Sedimentation in a Stratified Ambient

by

François Alain Blanchette

B.S., Université de Montréal, 1999

Submitted to the Department of Mathematics
in partial fulfillment of the requirements for the degree of

DOCTOR OF PHILOSOPHY

at the

MASSACHUSETTS INSTITUTE OF TECHNOLOGY

SEPTEMBER 2003

Author .....
Department of Mathematics
July 17th, 2003

Certified by .....
John W. M. Bush
Associate Professor of Applied Mathematics
Thesis Supervisor

Accepted by .....
Rodolfo R. Rosales
Chairman, Applied Mathematics Committee

Accepted by .....
Pavel I. Etingof
Chairman, Department Committee on Graduate Students

Sedimentation in a Stratified Ambient

by

François Alain Blanchette

Submitted to the Department of Mathematics
on July 17th, 2003, in partial fulfillment of the
requirements for the degree of
DOCTOR OF PHILOSOPHY

Abstract

We study the interaction between settling particles and a stratified ambient in a variety of contexts. We first study the generation of large scale fluid motions by the localised release of a finite mass of particles in the form of plumes or gravity currents. We present the results of a combined theoretical and experimental study describing the evolution of particle clouds formed by the release of heavy particles. In the early stages of motion, particle clouds behave as turbulent fluid thermals; however, their radial expansion eventually stops and particles settle from the base of the cloud at their individual settling speed. We focus on deducing a criterion for the various modes of particle deposition from particle clouds in a stratified ambient. We proceed to study the deposition patterns resulting from particle–laden gravity currents that spread horizontally when released in a particle–free ambient. Using a box–model, we focus on bidisperse gravity currents and examine the resulting particle distribution and maximal deposit length. We then turn to suspensions where particles are initially present throughout the fluid. The simultaneous presence of particles and of a stratified ambient may lead to behaviour analogous to double–diffusive systems, with particles playing the role of a diffusing component. We examine the linear stability of the settling of a particle concentration gradient in a stratified fluid. Numerical simulations allow us to determine the stability of the system for a broad range of particle settling speeds and diffusion coefficients. We then report on layering arising from sedimentation in a density stratified ambient beneath an inclined wall. From our experimental study, we describe the series of horizontal intrusions formed by particle-free fluid intruding at its level of neutral buoyancy. We present numerical models describing the time evolution of the concentration of particles and the layer formation. Finally, we present an experimental and theoretical study of the combined influence of hindered settling and settling speed variations due to an ambient stratification. We develop a criterion for the stability of a suspension settling in a stratified ambient and experimental observations allow us to qualify the main features of this instability.

Thesis Supervisor: John W. M. Bush
Title: Associate Professor of Applied Mathematics

Acknowledgments

By far, the most important person I need to thank is my advisor, John W. M. Bush. His enthusiasm, numerous research ideas and helpful comments on how to improve my writing shaped this thesis and my approach to fluid dynamics in general. Thanks John!

Special thanks should also go to my collaborators Bev Thurber and especially Tom Peacock, who shared their experimental expertise and observations and helped make my thesis much more complete. I also would like to thank my thesis committee, Peko Hosoi and Martin Bazant for their helpful suggestions. Throughout my graduate studies, I have also greatly benefited from the teachings of Michael Brenner and Ruben Rosales. My undergraduate advisors, Anne Bourlioux and Joshua Bengio also largely contributed to spark my interest for research. Finally, I would like to acknowledge the helpful discussions I have had with my fellow graduate students, Francis Poulin and Jaehyuk Choi. I am also grateful to NSERC and FCAR for their financial support, as well as for the partial support of the Schlumberger foundation and NSF.

On a personal level, I would probably have been very miserable if it weren't for my roommates. I thank Alex for his willingness to help regardless of the situation, Peter for being ever resourceful and Alberto for his sense of humour and discussions. My life would also have been very boring if it weren't for the friends I made at MIT: Radoč, Peter C., Étienne, Nora, Jing, Boris, Aleksey and Jim. But the most important person I met at MIT is obviously Lei Yue, whose support was invaluable to me.

Pour finir, je veux remercier tous ceux qui, même de loin, m'ont aidé à persévérer dans mes études. D'abord ma grand-mère, pour avoir toujours été un modèle que j'ai cherché à imiter. Nancy, pour m'avoir fait comprendre que je pouvais me permettre d'être plus ambitieux que je ne l'étais avant de la rencontrer. Mais surtout, je remercie mes parents, Andrée et Roger, pour leur amour, leur support et pour le mode de vie qu'ils ont su me transmettre. Enfin, je veux remercier mon frère Mathieu, qui fut sans contredit ma plus grande source de stimulation intellectuelle et qui a toujours été mon meilleur compagnon. Merci!

Contents

List of Figures

List of Tables

Chapter 1

Introduction

Sedimentation in stratified fluids is a problem of primary environmental importance. The interaction of particulate matter and density gradients arises in a number of geophysical contexts. In the oceans, the settling of particles is important in the dynamics of coastal currents (Drake 1971), fluvial plumes in estuaries (Wright 1977) and turbidites (Parker *et al.* 1987). Large numbers of microorganisms in the oceans may also be described as suspensions (Pedley & Kessler 1992). Examples of sedimentation in the atmosphere include flows forced by volcanic ejecta (Sparks, Carey & Sigurdsson 1991, Woods, Holasek & Self 1995), dust storms (Simpson 1987) and urban pollution (Fernando *et al* 2001). Solid Earth also provides examples of sedimentation: the interaction of settling particles with stratified fluids has been considered in the chemical differentiation of the early Earth (Solomatov, Olsen & Stevenson 1993) and in the context of magma chambers where crystals and bubbles of low viscosity fluids are present (Huppert & Sparks 1984, Greenough, Lee & Fryer 1999). Particle–laden flows also arise in industry, for example in a variety of centrifugation processes (Ungarish 1993) and in the disposal of waste in the oceans and atmosphere (Fischer 1971).

Suspended particles may behave in two qualitatively different ways. If particles do not generate fluid motions on a scale much larger than that of an individual particle, they are said to be dynamically passive. The transition between dynamically active and passive suspended particles typically occurs when the velocity of the fluid motions due to the presence of particles exceeds the individual particle settling speed (Ungarish 1993). When particles are dynamically passive, the motion of the fluid is dictated by factors independent of the presence of particles (density differences, boundary conditions etc) and the particles are transported by the fluid and settle under the action of gravity (Ungarish 1993). Examples where particles are dynamically passive include particle–laden gravity currents driven by large temperature or compositional differences (Simpson 1987) and crystals in suspension in magma undergoing thermal convection (Martin & Nokes 1988). If however the particle concentration is sufficiently non–uniform, particles may be dynamically active and drive large scale fluid motion. For example, particle–laden fluid may drive turbidites (Parker *et al.* 1987), volcanic ash can generate large atmospheric flows (Sparks, Carey & Sigurdsson 1991) and a localised release of particles may generate particle clouds moving much faster than individual particles (Slack 1963). Random particle concentration fluctuations may

also occur in a suspension, leading to convective motions on the scale of the container (Hinch 1977).

The initial distribution of particles may also be divided into two categories. If particles are everywhere present in the fluid, the suspension is treated as a single fluid of varying particle concentration and whose properties (density, viscosity) are determined by both the fluid and solid phases. Such a description of the fluid is appropriate for a variety of industrial separation processes (Kinosita 1949), crystals settling in magma chambers (Sparks *et al.* 1993) and microorganisms in the oceans (Pedley & Kessler 1992). However, if initially particles are only present in a confined area, the particle–laden fluid may behave as a second phase of fluid. Particle–laden and particle–free fluid then behave as two miscible fluids of different densities, with the additional feature that particles may settle out of suspension. The release of particles in a localised region arises in a number of geophysical and industrial settings; for example when fluvial plumes enter into the ocean (Wright 1977) and industrial waste is discharged into rivers and oceans (Bühler & Papantoniou 1999) or the atmosphere (Fischer 1971).

In many physical settings, the suspending fluid through which particles settle is not homogeneous. For example, stable stratifications are ubiquitous in lakes, which are often thermally stratified (Monismith 1985) and in the oceans, where both heat and salt variations typically contribute to density gradients (Schmitt 1994). Over scales relevant to the dynamics of volcanoes, the atmosphere is stably stratified due to pressure variations (Sparks *et al.* 1991). Magma chambers may also contain large density variations, due to gradients in temperature and chemical concentrations (Hodson 1998). These stratifying agents (temperature, salt, chemicals) are advected by the fluid and subject to diffusion owing to Brownian motion (Einstein 1956). An ambient density stratification may have a significant influence on the evolution of a suspension and elucidating this influence in a variety of physical settings will be the focus of this thesis. We will examine the influence of particles on a number of classical fluid dynamics problems: fluid thermals, gravity currents and boundary–driven flows. We also study the influence of an ambient stratification on classical suspension problems: the Boycott effect, settling of a particle concentration gradient and the effects of hindered settling.

We begin by studying the release of a finite mass of negatively buoyant fluid, a so–called fluid thermal (Scorer 1957), within a homogeneous or stably stratified environment. The dynamics of fluid thermals have been studied extensively (Woodward 1959, Turner 1973). If a sufficiently large mass of negatively buoyant fluid is released, that is if $Re = Ub/\nu > 1000$, with U, b and ν the velocity, radius and viscosity of the heavy fluid, then the fluid sinks as a turbulent thermal. A heavy thermal grows by turbulent entrainment of ambient fluid and its radius increases linearly with distance from the source. As a consequence of entrainment, the density difference between the thermal and the ambient decreases with distance from the source. If the thermal evolves in a stratified environment, the buoyancy of the thermal is continually reduced until the thermal attains a level of neutral buoyancy (Morton, Taylor & Turner 1956). At that point, the thermal briefly keeps sinking owing to its momentum, but its buoyancy becomes positive, forcing the thermal to rebound. Oscillations about the neutral

buoyancy height ensue until momentum is sufficiently dissipated. The thermal then spreads as a gravity current.

The presence of particles as a source of buoyancy complicates this physical picture. Clouds of particles may settle significantly faster than individual particles and their motion resembles that of fluid thermals, as was first pointed out by Slack (1963). Slack also noticed that at a certain distance from the source, called the fallout height, the radial expansion of the cloud stops. The particles then settle from the base of the thermal and form a bowl–shaped swarm that descends at the settling speed of individual particles. Particles thus initially behave as in dilution and contribute to the buoyancy of the thermal, before exiting the cloud when their individual settling speed becomes comparable to that of the cloud. We present in chapter 2 the results of a combined theoretical and experimental study aimed at elucidating the mixing processes accompanying the settling of particle clouds in homogeneous and stratified ambients. In §2.2, we present our theoretical model and numerical simulations of the progression of a particle cloud. Comparison with experiments described in §2.3 enables us to validate our model in the case of both homogeneous (§2.4) and stratified ambients (§2.5). The broader relevance and applications of this work are considered in §2.6. Particular attention is given to deducing criteria for the various modes of particle deposition from particle clouds in a stratified ambient. Our model allows us to determine whether a particle cloud will leave a localised deposit or alternatively reach the lower boundary while remaining particle–laden, thus giving rise to a particle–laden gravity current.

To fully describe the shape of deposits left by particle clouds, an accurate description of the deposits resulting from particle–laden gravity currents is required. Gravity currents occur throughout nature and commonly encountered examples include rivers flowing into the sea, lava flows and storms in the atmosphere (Simpson 1987). By definition, a gravity current occurs when relatively dense fluid is released and spreads beneath a lighter fluid. The gravitational force then acts to generate a horizontal pressure gradient that drives flow and thus decreases the potential energy of the system. The first type of gravity currents to be studied consisted of a constant volume of dense fluid spreading over a flat surface. This scenario was studied in the context of toxic gas release by Von Kármán (1940) who derived a condition on the velocity of the nose of the current. Benjamin (1972) later performed a more thorough analysis and corrected the derivation of Von Kármán, although his result was identical. A similarity solution valid for long times was derived by Hoult (1972) who was interested in the spreading of oil over water. A particularly helpful tool, the box–model, was introduced by Huppert & Simpson (1980); the assumption that the current is flat at all times allows great simplifications and closed form solutions in many instances, and predicts the main features of the flow to a remarkable accuracy.

Many gravity currents carry small particles in suspension. Rivers are usually sediment laden (Parker *et al.* 1987), powerful storms carry dust and water containing industrial waste is particle–laden (Simpson 1987). When the density difference between the current and the ambient is mostly due to compositional or temperature differences, as may be the case when fresh rivers enter the ocean, the particles are passive and are simply carried by the gravity current. However, other gravity currents are

driven by suspended material, i.e. the density difference between the current and the ambient is mostly due to the presence of particles in suspension. Examples of particle–driven gravity currents include flows generated by volcanic ashes (Sparks, Carey & Sigurdsson 1991) and underwater turbidites (Parker *et al.* 1987). Because the density difference between the current and the ambient is not constant, particle–laden gravity currents do not yield a similarity solution and one must resort to box–models or numerical simulations to elucidate their dynamics. Bonnecaze, Huppert & Lister (1993) performed a numerical study of the horizontal spreading of suddenly released particle–laden fluid using the shallow–water approximation. Moodie (2000) later suggested the use of a time–dependent settling speed in order to take into account the time–dependent level of turbulence in the system. More recently, three dimensional simulations of particle–laden gravity currents have allowed a more precise study of the shape of the nose and of lateral instabilities (Necker *et al.* 2002), but such simulations are still limited to relatively low Reynolds number currents ($Re \approx 2000$). The influence of the Earth's rotation on large scale particle–laden gravity currents was studied using the shallow–water approximations by Hogg, Ungarish & Huppert (2001).

Most of the earlier studies of particle–laden gravity currents have focused on monodisperse suspensions, where particles are all of the same size and density. While this is a natural first approximation, geological applications of gravity currents often require a more detailed description of the deposits resulting from polydisperse gravity currents (Kneller & Buckee 2000). In chapter 3, we focus on deposition patterns resulting from turbulent and laminar gravity currents containing bidisperse sediment, i.e. two different types of particles. In §3.1, we present new analytical results for the length of deposits resulting from particle–driven currents by considering a box–model. Numerical simulations of deposits left by bidisperse gravity currents are presented for turbulent (§3.2) and laminar flow (§3.3) and allow for a better understanding of the impact of polydispersity on the shape and particle distribution of deposits resulting from polydisperse gravity currents.

We then turn our attention to flows where particles are initially present throughout the fluid. We consider suspensions settling under the influence of gravity through an ambient density stratification associate with a gradient of a diffusing component such as a solute or heat. The simultaneous presence of settling particles and of a diffusing component may result in flows reminiscent of double–diffusive systems. Double–diffusive systems are marked by the presence of opposing gradients (or jumps) of two diffusing components, such as heat and salt (Turner 1985). Such systems are particularly relevant in oceanography, where both temperature and salinity gradients may be present (Schmitt 1994) and also arise in magma chambers where two or more solutes may be present (Spera 1986).

Instabilities relying on the difference in the diffusivity of the two components may be observed in double–diffusive systems. If hot and salty fluid overlies cold and fresh fluid, instabilities may develop even when the total density profile is stable (Stommel, Arons & Blanchard 1956). Because the diffusivity of heat, κ_T, is much larger than that of salt, κ_S, a sufficiently small fluid parcel displaced downward will quickly adjust its temperature to that of its surroundings while remaining saltier than neighbouring

fluid. The fluid parcel thus becomes heavier and its downward motion is amplified. Fluid parcels displaced upward similarly see their motion amplified and long, thin tubes of fluid alternately rise and sink (Veronis 1968). The so–called salt–fingers thus increase significantly the vertical transport of heat and salt (Schmitt 1979). The size of the fingers, δ, must be such that the typical advection time of a finger is larger than the typical diffusive time scale of heat $\delta^2/\kappa_T \ll W/\delta$, with W the vertical velocity of the salt–finger, but smaller than the typical diffusive time scale of salt $W/\delta \ll \delta^2/\kappa_S$. (Tritton 1988). The opposite scenario, where cold and fresh fluid overlies hot and salty fluid, may also be unstable. A fluid parcel displaced downward again adjusts its temperature faster than its salinity. Being fresher, it becomes lighter than its surroundings, rises and overshoots its initial height. The repetition of this process amplifies small disturbances and generates oscillations of growing amplitude (Baines & Gill 1969).

Particles settling in a density gradient may play the role of the slowly diffusing agent in a double–diffusive system. Particle–fingers, the analog of salt–fingers, have been observed experimentally when particles settle across a density interface in a quiescent fluid by Green (1987) and at the base of a spreading gravity current by Maxworthy (1999) and Parsons *et al.* (2001). Particles may also act to stabilise an unstable ambient stratification as they settle in a light fluid underlying a heavier fluid. Convective plumes then form above the suspension as particles settle and release light fluid (Huppert *et al.* 1991).

The diffusion coefficient of particles in suspension may be much larger than what would be expected from Brownian motion (Caflisch & Luke 1985). For very small particles, of the order of 10nm, Brownian motion is dominant and determines the magnitude of the effective diffusion coefficient. However, for larger particles, settling velocity fluctuations due to the presence of neighbouring particles, the so–called hydrodynamic dispersion effect, dominate Brownian motion (Ham & Homsy 1988). The magnitude of the diffusion coefficient therefore depends on the settling speed, particle radius and concentration (Mucha *et al.* 2003, Martin, Rakotomalala & Salin 1995). Moreover, particle diffusion is typically anisotropic, diffusion parallel to the settling direction being greater than that perpendicular (Nicolai *et al.* 1995).

In chapter 4, we examine the linear stability of the settling of a particle concentration gradient in a stratified fluid. In the limit of particle settling speed going to zero, the double–diffusive stability diagram is recovered (Baines & Gill 1969). The dependence of the stability of the system on the particle settling speed is studied numerically. We first review the main features of thermohaline instabilities in §4.2. Assuming a constant settling speed, we then perform a linear perturbation analysis of the system of equations considered by Baines & Gill (1969), with the addition of a particle concentration advection term. We present the governing equations and the method used to analyse their stability in §4.3. Numerical simulations allow us to determine the stability of the system for a broad range of particle settling speeds and diffusion coefficients and the results are presented in §4.4. We study the stability of a particle concentration gradient settling in a uniform ambient and in stable and unstable ambient stratifications. We also investigate the influence of the relative magnitude of the diffusivity of particle concentration and ambient density.

In double–diffusive systems, both salt–fingers and overstable oscillations eventually break down when the amplitude of the disturbances becomes too large. Horizontal layers, between which discrete changes in fluid properties arise, are then formed, (Turner 1985). Layers also form when a statically stable salinity gradient is heated from below, as reported by Turner (1968) and Huppert & Linden (1979). Initially, heated fluid rises to its level of neutral buoyancy, where the density difference due to temperature balances that due to compositional differences. As time progresses, a well–mixed layer forms in which the temperature and salinity become constant. This layer then transfers heat to the overlying fluid and subsequent layers develop in turn until the whole container is marked by layers. Heating a salinity gradient from the side also generates layering (Huppert & Turner 1978). When a density gradient is heated (or cooled) from the side, layers form simultaneously as fluid ascends along the wall and intrudes at its level of neutral buoyancy (Hart 1971). Theoretical investigations into the origins of layers arising from sidewall heating or cooling have shown that both shear instabilities and sideways diffusive instabilities may be present (Thorpe 1969, Kerr 1989). The latter results from the presence of opposing horizontal gradients of two components of different diffusivity and their mechanism is analogous to that of salt–fingers.

The presence of a sloping boundary provides another means of generating horizontal layers in a double–diffusive system. Sloping boundaries are generally present in magma chambers (Martin & Campbell 1988) and arise in the oceans in the form of inclined ice shelves. A stratified ambient beneath a sloping roof may also be found in Antarctica's lake Vostok, which lies beneath a few kilometers of ice (Wuest & Carmack 2000). In a fluid stably stratified by a single component, convection develops beneath an inclined wall. Because of the no–flux requirement at the boundary, contours of constant density (isopycnals) must meet the boundary at right angles. Beneath the inclined boundary, in a stably stratified environment, fluid is thus heavy relative to fluid in the bulk, causing it to sink along the inclined wall (Phillips 1970). If the system is stratified with two components of markedly different diffusivity, the convection that develops beneath the wall due to the faster diffusing component is opposed by the density stratification due to the slower diffusing component. Consequently, a series of intrusions proceed into the ambient from the sloping wall. This phenomena was investigated experimentally by Linden & Weber (1977) and Turner & Chen (1974), and theoretically by Chen (1971) and Paliwal & Chen (1977).

In chapter 5, we report layering that arises from sedimentation in a density stratified ambient beneath an inclined wall. The so–called Boycott effect (Boycott 1920) occurs when a suspension of relatively heavy particles underlies an inclined wall. Particles settle away from the wall, creating a layer of clear fluid that is buoyant relative to the bulk fluid and so ascends. As it does so, it entrains fluid from the bulk and drags particles upward until an equilibrium is achieved where the settling of particles is countered by the vertical motion of the fluid. The presence of a stable ambient stratification is expected to modify this physical picture. As fluid rises along the wall, the density difference between fluid within the Boycott layer and the ambient suspension will diminish. If fluid within the Boycott layer reaches its level of neutral buoyancy, it will stall and we thus expect horizontal intrusions to appear. To verify

this physical picture, we performed a series of experiments described in §5.3 in which particles settled in a salt stratified ambient. The observations and measurements made are discussed in §5.4 and a model describing the time evolution of the concentration of particles in the presence of steady layers is presented in §5.5. We also present numerical simulations capturing the formation of layers by the stratified Boycott effect in §5.6. The relevance of this mechanism to layering in magma chambers is considered in §5.7.

In many instances, compositional variations in the suspending fluid affect the settling speed of particles through their influence on fluid density and viscosity. When the particle density is close to that of the suspending fluid, variations in the ambient fluid density may significantly modify the particle settling speed. The dilution of undersea sewage clouds (Fischer 1971) and suspensions of microorganisms in the oceans (Pedley & Kessler 1992) are examples where the particle settling speed may vary significantly over the course of the settling process. Viscosity gradients may modify the particle settling speed of crystals sedimenting in magma chambers (McMillan, Long & Cross 1989). The particle size may also evolve as particles settle, if melting or crystallisation occurs; for example, significant particle size changes arise in the melting or formation of ice crystals in marine snow (MacIntyre, Alldredge & Gotschalk 1995) and during the sedimentation of crystals in magma (Cashman 1993). Bubbles may also increase in size as they rise in the presence of a pressure gradient (Delnoij *et al.* 1997). If particles settle due to centrifugation, the centrifugal force increases with distance from the axis of rotation, and consequently the velocity of the particles increases, as was studied by Essington, Mattingod & Ervin (1985) in the case of a single particle.

The presence of neighbouring particles also modifies the particle settling speed in a suspension. Hindered settling results from the fluid upflow generated in settling suspensions. As the particle concentration increases, the fluid reflux becomes larger, thus reducing the settling speed of particles in suspension (Richardson & Zaki 1954). Kynch (1952) examined the influence of hindered settling on the evolution of a dilute suspension of heavy particles settling in a uniform ambient and found a variety of non–trivial solutions. Starting from an initial particle concentration jump, one of two things may happen: if the particle concentration increases with height, an intermediate region forms, joining smoothly the two regions of different particle concentration. However, if the particle concentration decreases with height, the concentration jump remains sharp and propagates as a shock. Concentration jumps may also form from continuous initial particle distributions if the particle concentration decreases sufficiently rapidly with height.

The combined influence of hindered settling and settling speed variations has not been previously investigated. Chapter 6 is devoted to the theoretical and experimental investigations of hindered settling in a stably stratified ambient. In §6.2, we review the results of Kynch (1952) for suspensions in a homogeneous ambient before extending them to the case of a stably stratified ambient in §6.3. The stability of the resulting motion is discussed in §6.4 and §6.5 is concerned with the experimental verification of these results for a suspension of latex particles settling in a stable density gradient.

We proceed by introducing a few general concepts and notation which will be

used in later sections. We have tried to use the most commonly accepted notation, however in many cases there is no unanimous choice and we fix here the notation to be used in the remainder of the thesis.

1.1 General Considerations

Stable density stratifications are typically obtained through variations in the concentration of one or more solutes such as salt or sugar, or through temperature variations. The added density is assumed to be proportional to the concentration of the solute, S, and to the difference in temperature between the fluid and a reference state, $\Delta T = T - T_0$,

$$\rho_f = \rho_0(1 - \alpha\Delta T + \beta S) \tag{1.1}$$

where T_0, ρ_0 are the temperature and density of the fluid in the reference state and α and β are respectively the temperature and solute expansion coefficients. For small values of ΔT and S, α and β are constant to a good approximation (Handbook of Chemistry and Physics 1986).

Once dissolved, the solute molecules are transported by the fluid. Consider a container of height h in which solute is left to reach equilibrium under the combined influence of gravity and diffusion due to Brownian motion. If we assume no horizontal variations and a fluid at rest, the equation governing the concentration of solute is

$$\partial_t S - U_s \partial_z S = \kappa \partial_{zz} S, \tag{1.2}$$

where U_s is the settling speed of an individual solute molecule, κ the diffusion coefficient and z the height. The relevant boundary conditions are that of no solute flux at the base and top of the container, $-U_s S = \kappa \partial_z S$ at $z = 0, h$ and the steady state solution is

$$S(z) = Ae^{\frac{-U_s z}{\kappa}} \tag{1.3}$$

where A is a constant depending on the initial concentration. As a measure of the relative importance of settling and diffusion, we consider the ratio $S(h)/S(0) = e^{-Pe}$, where we defined the Péclet number as $Pe = U_s h/\kappa$. If settling is dominant, as is expected to be the case for large particles, $Pe \gg 1$ and $S(h)/S(0) \approx 0$. If on the other hand diffusion is dominant, $Pe \ll 1$ and $S(h)/S(0) \approx 1$.

To evaluate the relative importance of settling and diffusion in terms of more fundamental quantities, we use the Stokes–Einstein relation (McQuarrie 2000)

$$\kappa = B\frac{kT}{\nu a}, \tag{1.4}$$

where ν is the fluid viscosity, a the particle size, $k = 1.38 \times 10^{-23} JK^{-1}$ is Boltzmann's constant, T is the temperature expressed in Kelvin and B is a constant of order one whose value depends on the nature of the solute. If a single spherical particle is settling in a uniform fluid at low Reynolds number ($Re_p = U_s a/\nu \ll 1$), its settling speed may be found by neglecting the inertial response of the fluid and solving for the flow around

a translating sphere. The drag on the particle is then found to be $F_d = 6\pi\rho_f\nu a U_s$, where g is the gravitational acceleration and ρ_f the fluid density (Batchelor 1967). Coupling this drag with the buoyancy force on a particle $F_b = 4\pi a^3\Delta\rho g/3$, where $\Delta\rho = \rho_p - \rho_f$ and ρ_p is the particle density, yields the Stokes settling speed for a spherical particle

$$U_s = \frac{2\Delta\rho g a^2}{9\rho_f\nu} \tag{1.5}$$

Using equation (1.4) and (1.5), we then find

$$Pe \sim \frac{\Delta\rho a^3 g h \rho_p}{\rho_f k T}. \tag{1.6}$$

Estimating the temperature as 300K, the density of the fluid and particles to approximately 1000kg/m^3, $\Delta\rho/\rho_f$ to be of order one and the height of the container to 30cm as would be the case in a laboratory setting, we find that the Péclet number is of order one for a particle radius of the order of $a = 10$nm. In most of the cases discussed in this thesis, the radius of the sedimenting particles considered will be of the order of 1μm or greater and Brownian motion may therefore be neglected. Conversely, for simple solute molecules such as salt and sugar, the size of a molecule is typically about 1nm and the influence of gravity is negligible. The solute is therefore subject to diffusion and transported by the fluid, but does not settle. The equation governing the evolution of the solute concentration, and also the temperature distribution, in an incompressible fluid is thus the familiar advection–diffusion equation

$$\partial_t S + \vec{u}\cdot\nabla S = \kappa\nabla^2 S. \tag{1.7}$$

1.1.1 Suspensions

Suspensions consist of a large number of settling particles transported by an interstitial fluid. We denote by ϕ the particle volume fraction

$$\phi = \frac{\text{Volume of particles}}{\text{Volume of suspension}} \tag{1.8}$$

If we denote the density of the fluid and of the particles respectively as ρ_f and ρ_p, the density of the suspension is then

$$\rho = (1-\phi)\rho_f + \phi\rho_p. \tag{1.9}$$

Similarly, we define the volume–averaged velocity of the suspension as

$$\vec{u} = (1-\phi)\vec{u}_f + \phi\vec{u}_p \tag{1.10}$$

where $\vec{u}_f$ and $\vec{u}_p$ are respectively the fluid and particle velocity fields. The particles we consider here generally have a small Reynolds number (with the exception of some

experiments presented in chapter 2)

$$Re_p = \frac{(u_p - u_f)a}{\nu} \ll 1 \tag{1.11}$$

where u_p and u_f are the magnitudes of the corresponding vector fields. Inertia is thus negligible when describing the motion of the particles relative to the fluid. We therefore assume that the particles move with velocity

$$\vec{u}_p = \vec{u} - u_s\hat{k}, \tag{1.12}$$

where the z–axis is in the direction opposite to gravity, $g = -g\hat{k}$, (Ungarish 1993).

For example, if a suspension is left to settle in a fluid at rest, the average flow field vanishes, $\vec{u} = 0$, while the particles settle under the influence of gravity, $\vec{u}_p = -u_s\hat{k}$, and induce a fluid back flow, $\vec{u}_f = -\phi/(1-\phi)u_s\hat{k}$, known as reflux. Fluid reflux acts to reduce the settling speed of neighbouring particles and u_s therefore depends on ϕ. The particle settling speed is thus usually written as

$$u_s = f(\phi)U_s \tag{1.13}$$

where $f(\phi)$ captures the influence of surrounding particles and U_s is given by equation (1.5). The average settling speed is therefore reduced as the concentration increases, $f(\phi) \leq 1$ and $f'(\phi) < 0$ (Richardson & Zaki 1954).

The influence of particle concentration on the viscosity of a suspension, and indirectly on the settling speed, was examined by Einstein (1911) who estimated the size of molecules by measuring the influence of dilute solutes on viscosity. He found that for small ϕ, the effective viscosity of the suspension, ν, is related to that of the fluid phase, ν_0, through $\nu/\nu_0 = 1 + 2.5\phi + O(\phi^2)$. The direct summing of the contribution of neighbouring particles to the settling speed of an individual particle is divergent, but this problem was circumvented by Batchelor (1972) who used a renormalisation method to find that in the limit of small particle concentrations, $f(\phi) = 1 - 6.55\phi + O(\phi^2)$. A commonly accepted empirical formula valid for moderate values of ϕ ($0 < \phi < 15\%$) is that of Richardson & Zaki (1954):

$$f(\phi) = (1-\phi)^n \qquad n = 5.1 \pm 0.1 \tag{1.14}$$

To describe flows in which the fluid motion is not necessarily parallel to that of the particles, we use the Navier–Stokes equations, appropriate for fluids with a linear stress-strain relation (Newtonian fluids). We also make use of the Boussinesq approximation which states that density variations are only important through their effect on the force of gravity. The governing equations are thus those of mass and momentum conservation (Batchelor 1967)

$$\partial_t \rho + \nabla \cdot [(1-\phi)\rho_f \vec{u}_f + \phi\rho_p \vec{u}_p] = 0 \tag{1.15}$$

$$\partial_t \vec{u} + \vec{u} \cdot \nabla\vec{u} = -\nabla p + \frac{\rho}{\rho_0} g\hat{k} + \nu\nabla^2\vec{u} \tag{1.16}$$

where p is the average pressure and ρ_0 a constant reference density. In the case of small ϕ and if the suspending fluid is incompressible, we may approximate (1.15) by the solenoidal condition

$$\nabla \cdot \vec{u} = 0. \tag{1.17}$$

The particle concentration is being advected with velocity u_s and is also diffusing, with diffusion constant κ_ϕ. The settling speed in a suspension is defined as the average velocity of a large number of particles, but deviations from this mean value act to diffuse the particle concentration and are included in κ_ϕ (Caflisch & Luke 1985, Ham & Homsy 1988). For $a < 10$nm, Brownian motion determines κ_ϕ; however, for larger particles κ_ϕ is dominated by random settling speed fluctuations due to local variations in ϕ (Martin, Rakotomalala & Salin 1995). Consequently, particle diffusion is anisotropic, diffusion parallel to the settling direction being typically greater than that perpendicular $\kappa_{hor} = \Phi\kappa_{ver}$, $\Phi < 1$ (Nicolai *et al.* 1995). The equation describing the evolution of ϕ is thus

$$\partial_t\phi + \nabla \cdot [(\vec{u} - u_s\hat{k})\phi] = \kappa_\phi(\phi_{zz} + \Phi\phi_{xx}) \tag{1.18}$$

Random particle concentration fluctuations in suspensions may cause density variations which in turn generate large scale fluid motions (Hinch 1977). Such variations occur on the scale of the container size, h, and scale as $\Delta\phi_{flu} \sim \phi^{1/2}a^{3/2}h^{-3/2}$, thus giving rise to convective motions of typical velocity $U_{flu} \sim g'\phi^{1/2}a^{3/2}h^{1/2}\nu^{-1}$, where g' is the reduced density of particles, $g' = g(\rho_p - \rho_f)/\rho_f$ (Brenner 1999). We restrict our study to systems where the particle size ($\sim 10^{-5}$m) and container size ($\sim 10^{-1}$m) are such that $\Delta\phi_{flu} \sim 10^{-7}$ is small relative to $\phi \sim 10^{-2}$ and we thus neglect the effect of random fluctuations. We also note that the presence of a large concentration of particles, $\phi > 15\%$, in a Newtonian fluid may qualitatively alter the properties of the fluid (specifically render it non-Newtonian), for example by giving rise to a finite yield stress (Sigworth 1996). Throughout this thesis, we shall restrict our attention to systems with small particle concentrations so that the resulting suspension behaves as a Newtonian fluid.

Having established the governing equations of motion and the principal notations used, we may now proceed with our study of sedimentation in a stratified ambient.

Chapter 2

Particle clouds

2.1 Introduction

The sudden release of a large number of particles arises in a number of geophysical and industrial settings, the most important example being the discharge of industrial waste into rivers and oceans (Bühler & Papantoniou 1999). In the case of contaminated waste, the deposition pattern of the particles, as well as the fate of the fluid with which they were in contact, are important considerations.

If the motion of an isolated mass of heavy fluid is sufficiently vigorous, the fluid sinks as a turbulent thermal. The single governing parameter of the evolution of a thermal in a homogeneous environment is the total buoyancy $Q = g'V_0$, where $g' = g(\rho - \rho_f)/\rho_f$ is the reduced gravity, ρ the density of the thermal and V_0 the initial volume of the thermal, and ρ_f the density of the ambient fluid. In a homogeneous ambient, even though the density difference between the thermal and the ambient is reduced owing to the entrainment of ambient fluid, the buoyancy, Q, remains constant. In terms of the distance from the source, z, and assuming a negligible initial radius, we find by dimensional analysis that the radius, b, velocity, U, and reduced gravity, g', of the cloud are given by

$$b = \alpha z, \qquad U \sim \frac{Q^{1/2}}{z}, \qquad g' \sim \frac{Q}{z^3} \tag{2.1}$$

where α is a constant. As a function of time after release, we have

$$b \sim Q^{1/4}t^{1/2}, \qquad U \sim Q^{1/4}t^{1/2}, \qquad g' \sim Q^{1/4}t^{-3/2}. \tag{2.2}$$

The numerical value of the entrainment coefficient, α, has been measured by different authors (Scorer 1957, Woodward 1959), with values ranging from 0.13 to 0.53 and an average value close to $\alpha = 0.25$.

In a homogeneous environment, thermals thus grow indefinitely in size and theoretically reach infinite depth (although viscous forces come into play at long times). However, if a sinking thermal evolves in a stratified environment, its buoyancy is reduced by the entrainment of light ambient fluid. The thermal eventually reaches

a level of neutral buoyancy, Z_N where its density matches that of the ambient. Considering a uniform stratification, such that the Brunt–Väisälä frequency, $N = (g/\rho_0)^{1/2}(d\rho_f/dz)^{1/2}$ is constant, dimensional analysis indicates that

$$Z_N = C_1 \frac{Q_0^{1/4}}{N^{1/2}} \tag{2.3}$$

where Q_0 is now the initial buoyancy of the thermal. Experimental measurements of C_1 (Morton *et al.* 1956) yield a coefficient of $C_1 = 2.6 \pm 0.4$ for the mean neutral buoyancy height.

This physical picture is appropriate to thermals with a relatively small density difference to the environment and with little or no initial momentum. However, the dynamics of momentum puffs, where the initial momentum is non-negligible are slightly different. It was demonstrated experimentally (Papantoniou, Bühler & Dracos 1990) that the entrainment coefficient is reduced with increasing initial momentum. Maxworthy (1974) studied vortex rings, the limit of no initial buoyancy, and Escudier & Maxworthy (1973) investigated the influence of added mass, the mass of fluid displaced by the cloud, on the dynamics of thermals. They also demonstrated that the rate of growth of the thermal depends on the density difference between the thermal and the ambient. However, their results indicate that after a distance of no more than 10 initial thermal radius, linear growth of the thermal radius holds to a good approximation.

If particles act as the source of buoyancy, the resulting particle cloud initially behave as a fluid thermal. However, after sinking to a given depth called the fallout height, Z_f, the particles fall out from the bottom of the thermal and the radius of the cloud remains constant thereafter. Particle clouds in a homogeneous ambient were studied over a limited range (from 1 to 10) of particle Reynolds number by Rahimipour & Wilkinson (1992). These authors studied the dynamics of a cloud with initial radius b_0 and made of N_p particles of volume V_p and with individual settling speed U_s. The buoyancy of the cloud is then $Q = (\rho_p - \rho_f)N_pV_p/\rho_f$ and the dynamics of motion were described in terms of a cloud number $N_c = U_s b_0 Q^{-1/2}$, which may be seen as the ratio of the individual settling speed to the descent speed of the cloud when seen as a thermal. For $N_c > 1$, the particles were observed to fallout from the cloud at their individual settling speed. For $N_c < 1$, the dynamics of the cloud were well described by that of an equivalent fluid thermal. Particle clouds were thus seen to go through three different phases. First the ballistic phase, where the cloud accelerates and entrains relatively little ambient fluid since the motion is not yet turbulent. This phase is typically short and the cloud progresses only a few cloud radius while in the ballistic phase. Once turbulence is well established, the clouds enter a self–similar phase where the motion closely resembles that of a fluid thermal. Finally, in the dispersive phase, the particles become separated from the entrained fluid and settle with speed U_s. Experiments were performed in the case of two-dimensional particle thermals (Nakatsuji, Tamai & Murota 1990). The resulting deposits were seen to depend critically on the ratio of the fallout height to the height of the container, Z_f/h. If $Z_f < h$, the deposit is localised, while if $Z_f > h$, the cloud

spreads upon reaching the bottom of the container, giving rise to a doubly–peaked deposit.

The recent study of Ruggaber (2000) shows that the assumption of linear entrainment may fail if the velocity of the cloud drops below a critical value. The entrainment coefficient is then seen to drop from $\alpha = 0.25$ by roughly 30% to values consistent with studies of vortex rings. The diminution of the entrainment coefficient was also observed and quantified as a function of the cloud number by Rahimipour & Wilkinson, (1992). Similarly, in the case of two dimensional clouds, Noh & Fernando (1993) concluded that the entrainment coefficient depended on the particle Reynolds number.

The case of a stratified ambient has received relatively little attention, despite obvious applications in the oceans and atmosphere. Luketina & Wilkinson (1994) considered a sediment cloud settling in a stratified ambient. They observed that the cloud progresses downward until reaching the fallout height, at which point the particles exit the cloud. The fluid remaining in the cloud then rises and oscillates about its rebound height, Z_R, at which point is spreads as a gravity current. The frequency of oscillation is near the Brunt-Väisälä frequency, N. The authors suggested the importance of a stratified cloud number, $N_s = U_s Q_0^{-1/4} N^{-1/2}$, noting that the fallout height appeared to decrease with N_s.

In this chapter, we examine the settling of a large number of heavy particles locally released in a homogeneous or stratified ambient. We consider cases where the motion is initially sufficiently vigourous that the particle cloud assumes the form of a turbulent thermal. An experimental study, complemented by numerical simulations, allow us to obtain an accurate picture of the resulting flow and deposition pattern. Most of the results presented in this chapter may be found in a paper by Bush, Thurber & Blanchette (2003). Our theoretical model and numerical simulations are described in §2.2. The experimental techniques employed in our study are detailed in §2.3. Our study of particle clouds settling in a homogeneous fluid is described in §2.4, while stratified environments are discussed in §2.5. The broader relevance and applications of this work are considered in §2.6.

2.2 Theoretical model

We consider the release of N_p heavy particles into an ambient fluid of density ρ_f. The particles have radius a and density ρ_p. The ambient fluid may either be homogeneous, in which case $\rho_f = \rho_0$, of stratified, in which case $\rho_f = \rho_0(1 + N^2 z)$, where z increases with depth from the point of release, $z = 0$. The result is a particle cloud of initial buoyancy $Q_0 = g' N_p \rho_p 4\pi a^3/(3\rho_0) = g' V_0$, where $g' = g(\rho_p - \rho_0)/\rho_0$ and V_0 is the initial volume of the particles. The Reynolds number of the cloud, $Re = Ub/\nu$, where b is the half width of the cloud, is assumed to be large, so that the cloud initially evolves as a turbulent thermal. The cloud thus entrains fluid as it descends and its radius grows linearly with distance from the source, $b = \alpha z$.

The cloud is initially assumed to be in a self–similar phase; consequently, the horizontal entrainment velocity is linearly related to the vertical velocity of the cloud

through $u = \alpha w$ (Morton 1956). The mass flux into the cloud yields (the cloud mass being $M = \rho V$)

$$d_t M = d_t(\rho V) = \eta\ 4\pi\alpha\rho_f r^2|\alpha w| \tag{2.4}$$

where ρ is the mean density of the cloud and η is a shape factor such that the volume of the cloud is given by $V = \eta\frac{4\pi}{3}r^3$. The cloud is thus treated as an oblate ellipsoid with horizontal radius r and height ηr. Scorer (1957) and subsequent studies on thermals indicate that $V = 3r^3$ and we hence take $\eta = 9/(4\pi)$ in what follows. The mean cloud density is defined as

$$\rho = \rho_p\phi + \rho_c(1-\phi) \tag{2.5}$$

where ϕ is the particle fraction in the cloud and ρ_c is the average density of the fluid present in the cloud. In a homogeneous ambient, fluid within the cloud has the same density as the ambient, $\rho_c = \rho_f$, and the buoyancy is thus independent of z.

In a stratified ambient, the z-dependent buoyancy is given by

$$Q = \frac{(\rho - \rho_f)Vg}{\rho_f(0)} \tag{2.6}$$

Combining $\frac{d\rho_f}{dt} = \rho_f(0)\frac{N^2}{g}w$, with equation (2.6), yields that the rate of change of the buoyancy is

$$d_t Q = -VwN^2. \tag{2.7}$$

Also, using Newton's second law, we relate the cloud's acceleration to the sum of the buoyancy and hydrodynamic forces

$$d_t(wV(\rho + k\rho_f)) = \rho_f(0)Q - C_d\rho_f\pi r^2 w^2\frac{w}{|w|} \tag{2.8}$$

where k represents the added mass of the cloud and C_d is a drag coefficient. While Luketina & Wilkinson (1994) set $C_d = 1/2$ and $k = 1/2$, values appropriate for a rigid sphere at high Reynolds number, experimental studies in the context of vortex rings suggest significantly smaller values. The results of Maxworthy (1974) derived by assuming $k = 0$, suggest $C_d = 0.02$ while those of Ruggaber (2000) obtained with particle clouds, actually yield negative values for both C_d and k, from which the author concludes that the correct values must be negligibly small. Comparison with our own experiments in §2.3 lead us to infer values consistent with the latter two authors and we thus set $k = 0$ and $C_d = 0.02$.

Equations (2.4-2.8) are non–dimensionalised using $l_n = Q_0^{1/4}N^{-1/2}$ as a typical length–scale, N^{-1} as a time–scale, and $\rho_f(0)$ as a characteristic density. We define a non–dimensional number $\beta = g^{-1}Q_0^{1/4}N^{3/2}$ which represents the fraction by which the ambient density changes between the level $z = 0$ and a typical neutral buoyancy height. In non–dimensional form the governing equations are

$$d_t V = \eta\ 4\pi\alpha r^2|w| \qquad d_t Q = -Vw \qquad d_t z = w \tag{2.9}$$

$$V\left(\rho_f(1+k) + \tfrac{\beta Q}{V}\right)d_t w = Q - C_d\rho_f\pi r^2 w^2\tfrac{w}{|w|} - \beta k w^2 V - \rho_f(1+k)w d_t V \tag{2.10}$$

where $\rho_f = 1 + \beta z$ and $\rho = \rho_f + \beta Q/V$ denote the densities of the ambient and cloud respectively and V, Q, w and z are dimensionless. The particle fraction in the cloud is given by

$$\phi = \frac{\rho - \rho_f}{\rho_p - \rho_f} \tag{2.11}$$

from which we may compute the density of the interstitial fluid in the cloud

$$\rho_c = \frac{\rho - \rho_p \phi}{1 - \phi}. \tag{2.12}$$

When the vertical velocity of the cloud is exceeded by the settling speed of the particles, the particles fallout and no longer contribute to the buoyancy of the cloud. After fallout, we then redefine Q to be

$$Q = \frac{(\rho_c - \rho_f)(V - \phi_0 V_0)g}{\rho_f(0)}. \tag{2.13}$$

This reduction of Q causes the cloud to rebound to its level of neutral buoyancy. We considered the final height of the cloud to be the rebound height. In order to compare with experimental results, we define the fallout height as the position of the center of mass of the cloud plus ηr at fallout. This corresponds to the leading edge of an axisymmetric cloud of horizontal radius r.

Numerical simulations of the full system of equations (2.10) were performed using a fourth order Runge–Kutta integrator. The cloud was started from rest ($w = 0$ and $z = 0$) and due to our non-dimensionalisation, $Q(0) = 1$. The non–dimensional initial volume of the cloud is given by $V(0) = V_0' Q_0^{-3/4} N^{3/2}$, where V_0' is the dimensional volume. The non-dimensional settling speed corresponds to the cloud number $N_s = U_s' Q_0^{-1/4} N^{-1/2}$ where U_s' is the dimensional settling speed. The values of β, $V(0)$ and N_s were varied over a range encompassing that used in our experiments.

In order to assess the reliability of our simulations, we first explored the small β, small V_0 limit, corresponding to a uniform ambient. The similarity solution described by equation (2.2) was well recovered in the limit of a small initial volume. We then proceeded to investigate the behaviour of a buoyant thermal in a stratified ambient, in the absence of particles. The cloud was seen to reach and overshoot its level of neutral buoyancy Z_N and thereafter to oscillate about Z_N. The period of oscillation was slightly more than $2\pi N^{-1}$ as was the case in the simulations of Luketina & Wilkinson (1994). The height of the intrusion depended largely on the entrainment coefficient α. In particular, it was seen to be 4.04 $Q_0^{1/4} N^{-1/2}$ for $\alpha = 0.15$ and 1.79 $Q_0^{1/4} N^{-1/2}$ for $\alpha = 0.35$. However, using the average value measured in our experiments, namely $\alpha = 0.25$, the intrusion height was 2.79 $Q_0^{1/4} N^{-1/2}$ which is seen to agree well with experimentally measured values of Z_N (Morton 1956). The intrusion height was also seen to be rather insensitive to changes in k and C_d, as we expect since these parameters influence the velocity of the cloud but not its composition.

a (cm)	U_s (cm/s)	ρ_p (g/cm^3)	Re_p
0.1095 ± 0.01	27.4 ± 1.4	2.5	300 ± 40
0.077 ± 0.008	22.0 ± 1.4	2.5	170 ± 25
0.065 ± 0.005	18.2 ± 0.8	2.5	118 ± 12
0.055 ± 0.005	16.4 ± 0.8	2.5	90 ± 12
0.039 ± 0.004	11.3 ± 0.5	2.5	44 ± 6
0.023 ± 0.002	6.6 ± 0.25	2.5	15 ± 2
0.016 ± 0.001	7.7 ± 0.25	4.2	12.3 ± 1.2
0.010 ± 0.001	4.4 ± 0.10	4.2	4.4 ± 0.7
0.005 ± 0.001	1.89 ± 0.05	4.2	0.94 ± 0.2
0.003 ± 0.0005	1.62 ± 0.05	4.2	0.48 ± 0.1
0.002 ± 0.0004	0.78 ± 0.05	4.2	0.15 ± 0.03

Table 2.1: Properties of the glass spheres used in the experiments: radius a, density ρ_p, measured settling speeds in water U_s and particle Reynolds number $Re_p = U_s a/\nu$.

2.3 Experimental method

We here briefly describe our experimental methodology. A cylindrical tank of diameter 45 cm and depth $h = 90$ cm was filled with water, or with a linearly stratified saltwater solution obtained using the Oster double–bucket system (Oster 1965). The cylindrical tank was housed in a rectangular casing filled with water in order to eliminate parallax effects. The payload was released by withdrawing a plunger from a funnel in the center of the tank. The release was made precisely at the surface of the water in order to minimise the initial momentum of the cloud. The resulting flow was illuminated from the side by a light sheet, and recorded with a video camera at sufficient distance (3-4 m) to eliminate errors associated with perspective. A grid was placed on the front face of the tank which, together with a time code generator on the video signal, enabled the computation of cloud speeds. Reviewing the video frames also enabled us to identify the fallout and rebound heights.

The properties of the eleven types of particles used (obtained from MO-SCI Corporation) are detailed in Table 1. The settling speeds, U_s, of the individual particles were measured in water. The particle Reynolds numbers, $Re = U_s a/\nu$, based on the individual particle settling speeds U_s ranged from 0.15 to 300. Payload masses varied from 0.2g to 50g. The payload also contained a small volume (typically 5-10 ml) of water which served to completely wet the particles, and so avoid the delayed onset of turbulence which typically accompanies dry particle releases (Ruggaber 2000). A few drops of dye were added to the payload in order to facilitate flow visualisation, in particular allowing us to keep track of the fluid entrained into the particle cloud.

The virtual origin is defined as the position of the thermal source inferred by extrapolating from its far-field form and assuming that the thermal motion is everywhere self-similar. Deviations of the thermal evolution from a self–similar structure (characterised by nonlinear dependence of cloud width on distance from the source)

in the vicinity of the origin typically lead to an offset between the real and virtual origins. For example, the delayed onset of turbulence for the case of large payloads of high density particles typically results in the virtual origin being displaced forward relative to the real origin (and so to a positive virtual origin). In our experiments, a rough estimate of the virtual origin could be obtained by tracing the far-field evolution of the cloud, deducing a mean entrainment coefficient for the cloud in its self–similar thermal phase, and extrapolating backward. As is typically the case in experimental investigations of turbulent thermals, indeterminacy in the virtual origin and variations in the entrainment coefficient are at once unavoidable and difficult to distinguish, and are the dominant source of scatter in the data.

We assume in the present study that throughout the thermal phase, the particles remain uniformly distributed throughout the cloud. A more detailed consideration of the interaction between the fluid and particle dynamics within the cloud was performed by Ruggaber (2000). Finally, the influence of the domain boundaries was investigated. The entrainment into the plume was significantly reduced when the plume width became comparable to half the tank width. This constraint limited the parameter regime explored in our study.

2.4 Homogeneous ambient

In all experiments, the cloud Reynolds number was sufficiently large than the cloud motion was turbulent. In agreement with the observations of Rahimipour & Wilkinson (1994), the cloud was seen to evolve through three successive phases. In the early stages of motion, the ballistic phase, the cloud accelerates and entrainment of ambient fluid is small. The motion quickly becomes self–similar and the particle cloud then behaves as a fluid thermal. Eventually, the cloud reaches the dispersive phase where particles fallout from the bottom of the cloud. The latter two phases are easily distinguished while the transition from the ballistic to the self–similar phase is more diffuse. Following fallout, particles settle in a bowl–shaped swarm within which there is little relative motion between particles. Particles first fallout from the center of the cloud, where the motion of the vortex motion is downward. Along the rim of the cloud, the vortex motion is upward, delaying fallout and thus causing the typical bowl shape. After fallout, fluid in the cloud progresses as a neutrally buoyant vortex ring (Maxworthy 1974).

2.4.1 Cloud width

We consider the maximal horizontal extent of the cloud to be the cloud width. The evolution of the cloud width was investigated through video recordings. We notice that although the cloud radius eventually increases linearly, the early ballistic phase exhibits a slower increase. The distance required to reach the self–similar phase was seen to depend on the initial payload size. In particular, for an initial mass of particles of 20g, the virtual origin was seen to be 10cm above the real origin. We therefore restricted our experiments to payloads of masses between 1 and 10g.

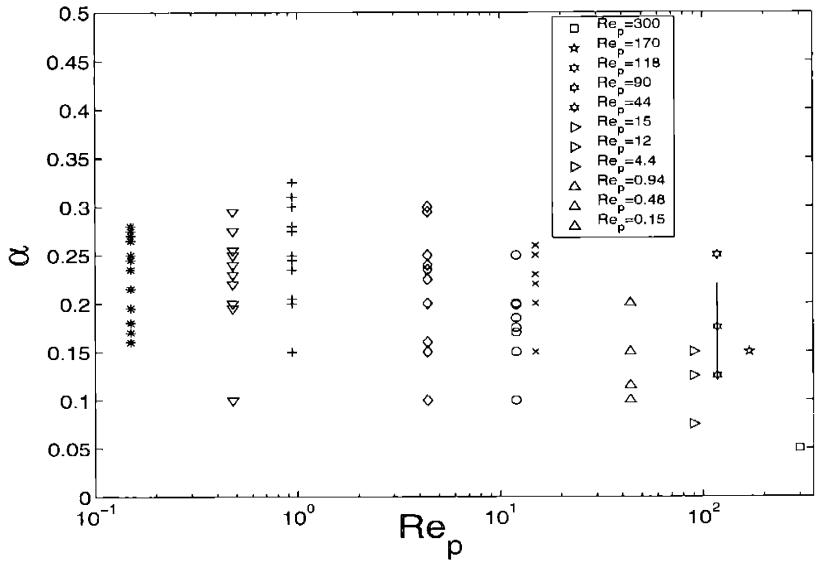

Figure 2-1: Dependence of the entrainment coefficient α on the particles Reynolds number, Re_p. A characteristic error bar is shown.

In the self–similar regime, the cloud width grows linearly with distance from the source. We measured an average entrainment coefficient $\alpha = 0.25$, with values ranging from 0.12 to 0.32, as shown in figure 2-1. When measured at a given height in the tank, the cloud width is expected to be independent of the initial buoyancy, provided the cloud is still in the self–similar phase. This is evident from figure 2-2 where the cloud width at respectively 30 and 50cm is plotted against cloud buoyancy. The scatter of the data is associated with the scatter in the entrainment coefficient. The data on the right of the dashed line is associated with clouds already in the dispersive phase and whose width consequently depend on the initial buoyancy. Note that more clouds are in the dispersive phase at $z = 50$cm.

2.4.2 Frontal position and cloud speed

Figure 2-3 illustrates the progression of the frontal position of the cloud, Z_M as a function of time for three particle clouds with $Re_p = 0.94$. The transition from the self–similar phase, where $Z_M \sim t^{1/2}$, to the dispersive phase, where $Z_M \sim t$, is evident. We note also that the ballistic phase is relatively short, and is shorter for smaller payloads. Comparing the evolution of Z_M with our numerical simulations allowed us to infer the added mass and hydrodynamic drag coefficients, k and C_d respectively. Figure 2-4 illustrates the descent rate of the 7g particle cloud (corresponding to the top curve in figure 2-3) plotted with the results of our numerical simulations. The dashed line represents the numerical results deduced using the hard sphere results ($C_d = k = 0.5$) proposed by Luketina & Wilkinson (1994). These results are clearly unsatisfactory: the cloud sinks too slowly, and the fallout height is thus underestimated. The solid line represents the numerical results obtained us-

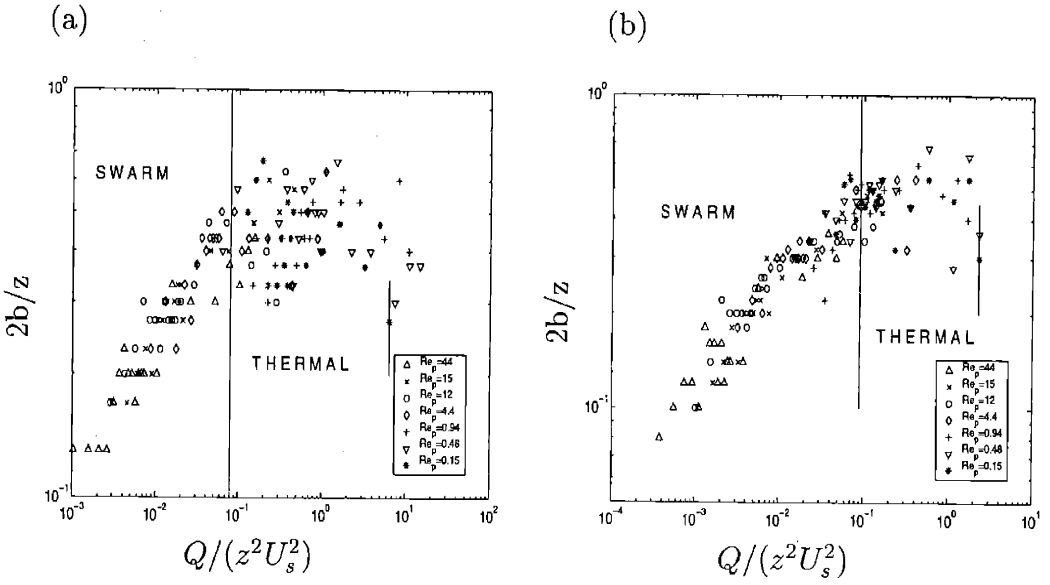

Figure 2-2: Dependence of the normalised cloud width $2b/z$ on the normalised cloud buoyancy $Q/(z^2U_s^2)$ at distance $z = 30$cm (a) and $z = 50$cm (b). The normalised width grows linearly in the thermal regime, $b \sim 0.25z$, (right of the dashed line) and remains constant in the swarm regime (left of the dashed line).

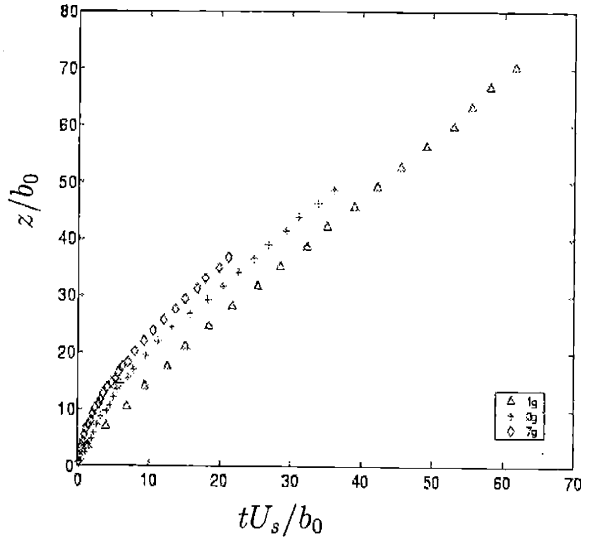

Figure 2-3: Time evolution of cloud front position Z_M/b_0 for three payload sizes: $\triangle$ 1g, $\circ$ 5g and $\diamond$ 7g. In each case $Re_p = 0.94$. Time is non–dimensionalised by the b_0/U_s. Particles settle at their individual settling speed after an initial thermal phase where the velocity of the cloud scales as $t^{-1/2}$.

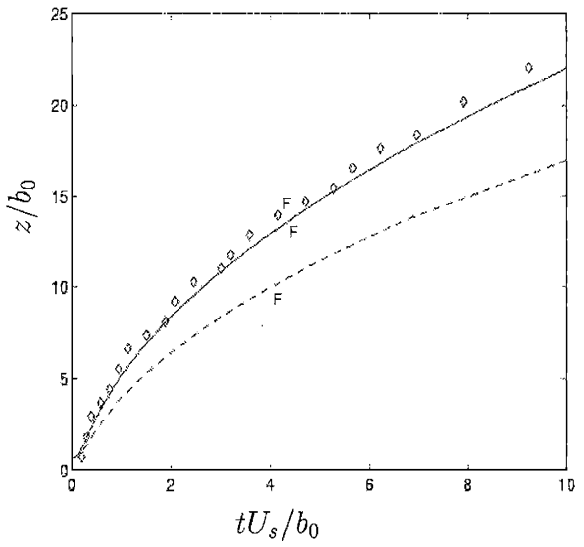

Figure 2-4: The numerical simulation of the 7g payload (top curve in the previous figure). The dashed line was computed with $C_d = k = 0.5$, the solid line was computed with $C_d = 0.02$, $k = 0$. F indicates the fallout point.

ing the values proposed by Maxworthy (1974) and Ruggaber (2000): $C_d = 0.02$ and $k = 0$. The numerics satisfactorily match the experimental data: the predicted and observed cloud speeds are consistent through both the cloud and swarm phases, and the fallout height is well reproduced. We proceed by adopting the results suggested by Maxworthy (1974) and Ruggaber (2000) $C_d = 0.02$ and $k = 0$, in all of our numerical simulations of particle clouds.

The observed cloud speed U measured at two depths, $z = 30$cm and $z = 50$cm, is plotted as a function of the cloud buoyancy in figure 2-5. The cloud speed is normalised by the particle settling speed U_s. In the self–similar regime, we expect a dependence consistent with equation (2.1) and thus of the form

$$\frac{U}{U_s} = C_2 \frac{Q^{1/2}}{zU_s}. \tag{2.14}$$

The data presented in figure 2-5 confirms this relation for cloud in the self–similar regime, and indicates that the coefficient $C_2 = (3.0 \pm .4)$. In the dispersive regime, the speed is independent of cloud buoyancy, and is comparable to the settling speed of the individual particles, U_s. The solid lines correspond to the results of the our numerical simulations, and indicate the dependence of the cloud speeds on height and initial cloud buoyancy. Note that the speed is recorded sufficiently far from the source that it is independent of the cloud's initial volume; consequently, the numerical lines are independent of particle Reynolds numbers.

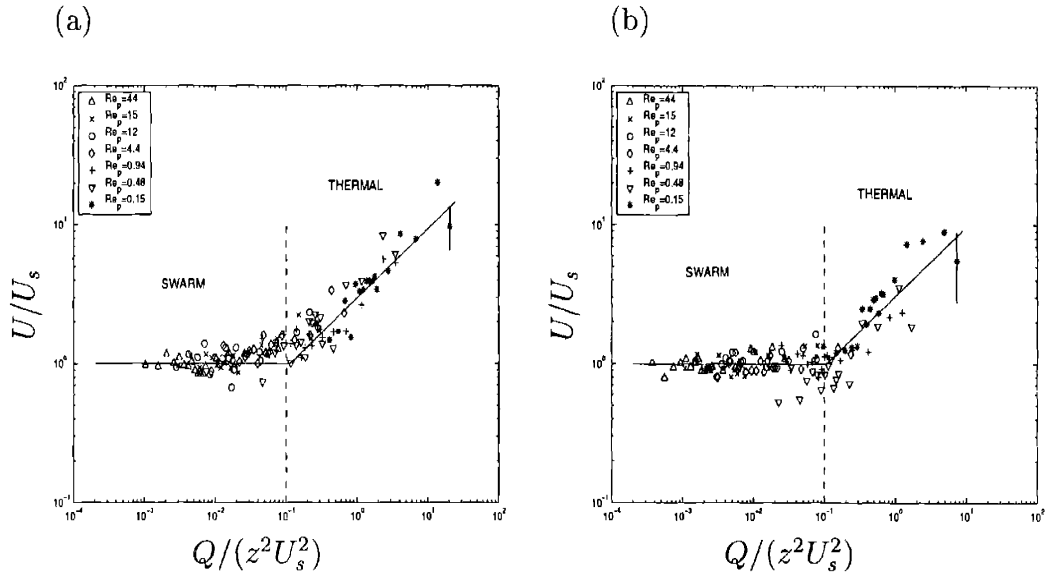

Figure 2-5: Dependence of the normalised cloud speed U/U_s on normalised buoyancy $Q/z^2U_s^2$ at $z = 30$cm (a) and $z = 50$cm (b). Left of the dashed line, the clouds are in their swarm phase, right they are in their thermal phase. The solid line are the corresponding numerical simulations.

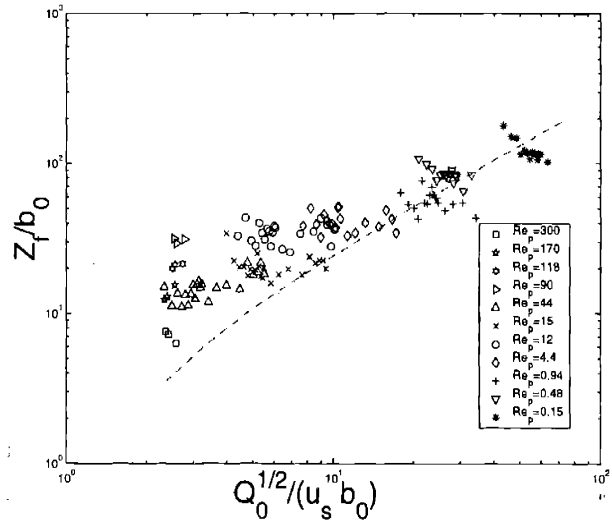

Figure 2-6: Observed dependence of normalised fallout height Z_f/b_0 on $Q^{1/2}/U_s b_0$ for all Re_p considered. The dashed line is the corresponding numerical simulation and has slope one for large Z_f.

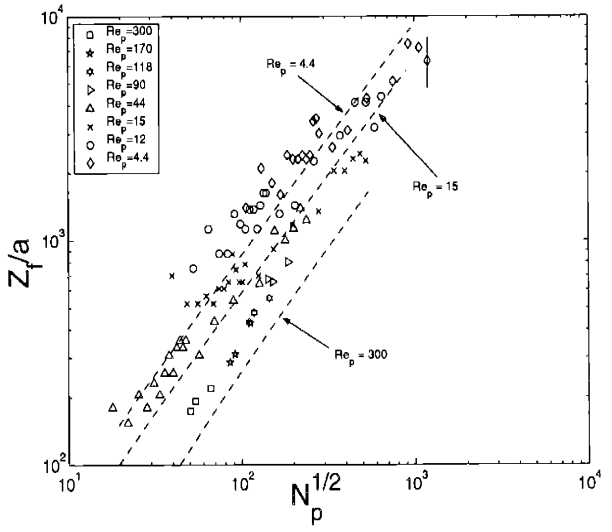

Figure 2-7: Dependence of the fallout height on the number of particles released, for large particle Reynolds. The dashed lines indicate the results of our numerical simulations for three values of Re_p. The offset of the numerical lines reflects the effect of the finite initial volume of the cloud.

2.4.3 Fallout height

Previous studies of particle clouds indicate that particles fallout when the cloud velocity matches the individual settling speed of particles (Bühler & Papantoniou 1999). This suggests, from equations (2.1)

$$Z_f = C_3 \frac{Q^{1/2}}{U_s}. \tag{2.15}$$

In our experiments, Z_f was taken to be the height at which particles first separated from the (dyed) cloud fluid. Figure 2-6 illustrates the dependence of Z_f/b_0 on $Q^{1/2}/(U_s b_0)$, where we used the initial radius of the cloud, b_0, to non–dimensionalise the results. A best fit line indicates a slope of 0.68. It may be seen that for low Re_p, the fallout height increases more slowly than predicted by equation (2.15). this behavior was also observed by Noh & Fernando (1993) and was attributed to particle–particle interactions at low particle Reynolds number (Davis & Acrivos 1985). Numerical simulations in the homogeneous case were seen to agree very well with equation (2.15) and predict a coefficient $C_3 = 3.66$. These may be seen as the dashed line in figure 2-6.

At high Re_p, the settling speed $U_s \sim \sqrt{g'a}$. Substituting for U_s and $Q = g' N_p V_p$ equation (2.15) yields the strikingly simple result $Z_f \sim N_p^{1/2} a$. Therefore for large Re_p, the fallout height depends only on the number of particles released and on their radius, but not on their density (or on the density of the fluid). Figure 2-7 indicates the observed dependence of the fallout height on a and N_p for particle clouds with $4.4 \leq Re_p \leq 300$, along with the results of our supporting numerical simulations.

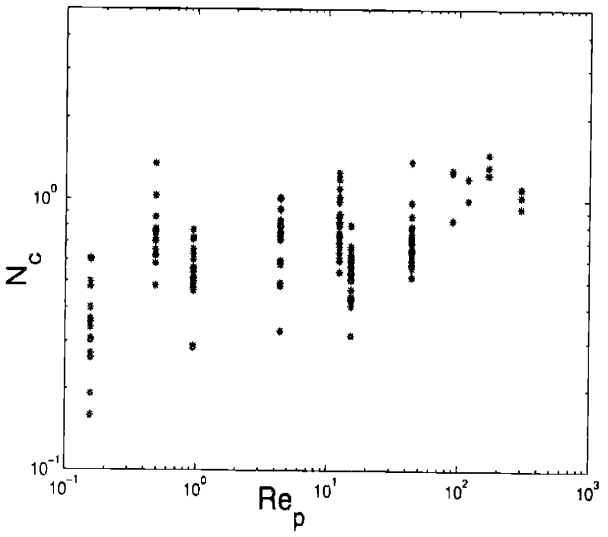

Figure 2-8: Dependence of the cloud number at fallout $N_c = U_s b Q^{-1/2}$ on the particle Reynolds number.

In both the experiments and numerics, the number of particles was calculated from the initial cloud buoyancy, particle size and density (table 2.3). In numerical simulations, the initial cloud buoyancy was varied over a range corresponding to those examined experimentally, and three particle sizes were chosen corresponding to particle Reynolds numbers $Re_p = 4.4$, 15 and 300. The slopes of the three resulting lines are seen to be equal to 1, in agreement with the predicted scaling. Our simulations indicate that the spread in the data results from the wide range of Re_p considered. For larger initial cloud volumes, used for particles with large Re_p, the virtual origin is located further above the position were particles were released and the fallout height is correspondingly reduced. Nevertheless, the numerics and experiments both serve to validate the proposed scaling, and indicate that the data may be described to leading order by

$$Z_f = (9 \pm 2)\ a N_p^{1/2} \quad . \tag{2.16}$$

In the parameter regime $1 < Re_p < 10$, Rahimipour & Wilkinson (1994), observed that the transition from the self-similar phase to the dispersive phase arises at a critical cloud number, $N_c = U_s b / Q^{1/2} = 1$. Figure 2-8 indicates the dependence of the critical cloud number on Re_p in our experimental study. Over a considerably wider parameter regime, $0.1 < Re_p < 300$, our observations emphasise the importance of a cloud number criterion for particle fallout, and indicate a mean critical cloud number of 0.8. This value is consistent with our inferred values of C_3 in (2.15) and the entrainment coefficient, $N_c \approx \alpha C_3$. Finally, we note that as Re_p increases, the critical cloud number increases and approaches one, which again suggests the importance of particle–particle interactions at low Re_p.

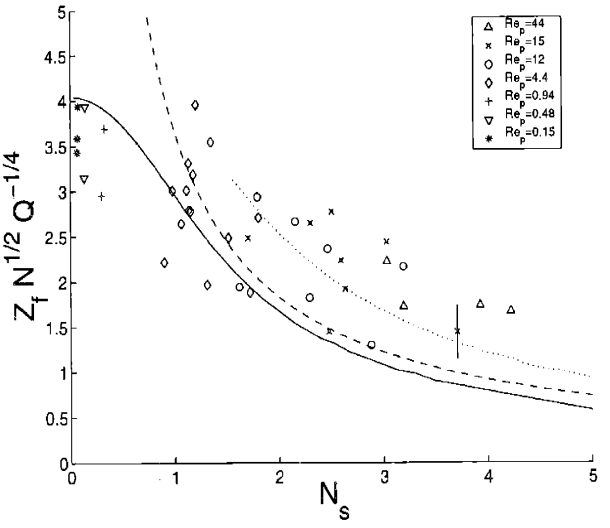

Figure 2-9: Dependence of the fallout height on the stratified cloud number $N_s = U_s Q^{-1/4} N^{-1/2}$ for particle clouds in a stratified ambient. The numerical results are denoted by a solid line. For large N_s, the influence of stratification is negligible and the fallout height is given by the homogeneous result (dashed line). The discrepancy between numerics and theory suggests reduced entrainment for large Re_p,; the dotted line indicates numerical simulations with $\alpha = 0.17$, the mean value appropriate for $12 < Re_p < 44$.

2.5 Stratified ambient

In the presence of a stratified ambient, the evolution of the particle cloud may be significantly different. We consider a linear ambient stratification so that $\rho_f(z) = \rho_0(1 + N^2/gz)$. We consider the settling speed U_s to be approximately constant throughout the settling process. This is justified by the fact that $(\rho_p - \rho_f)/\rho_f$ is only of the order of 5%. We therefore use the settling speed corresponding to the top of the container where $\rho_f = \rho_0$. A new lengthscale results from the presence of a stratification, $Q^{1/4}N^{-1/2}$, approximately corresponding to the level of neutral buoyancy of a fluid thermal, Z_N, see equation (2.3). The ratio of the Brunt-Väisälä period, $1/N$, to the time taken by individual particles to travel a distance Z_N, is the stratified cloud number $N_s = U_s Q^{-1/4} N^{-1/2}$, which determines the nature of the flow (Luketina & Wilkinson 1994).

In the case $N_s > 1$, the initial phase is similar to the motion of a particle cloud in a homogeneous ambient. The cloud progresses downward as a turbulent thermal until its velocity matches the settling speed of individual particles, at which point the particles fallout of the cloud. the particles again settle as a bowl–shaped swarm and give rise to a localised deposit. Following fallout, the fluid contained within the cloud descends a short distance owing to its inertia and then ascends and oscillates about it rebound height Z_R. The frequency of oscillation is close to N and as the oscillations are being damped, the cloud spreads as a gravity current. On the other hand, when

$N_s < 1$, the clouds reaches, and overshoots, its level of neutral buoyancy Z_N while retaining its particles. As the cloud spreads as a particle–laden gravity current, the particles rain–out thus giving rise to a much broader deposit. The fluid contained in the cloud once again finds itself buoyant and rises to its rebound height Z_R as in the case $N_s > 1$.

The fallout height depends crucially on the stratified cloud number. For small N_s, where particles settle relatively slowly, one expects the fallout height to corresponds to the intrusion height of a fluid thermal in a stratified ambient. Conversely, for large N_s, where the particles settle relatively fast, one expects the fallout height to be the same as it would be in a homogeneous ambient. Figure 2-9 illustrates the observed dependence of the fallout height on the stratified cloud number. For $N_s < 1$, the particles fall out over the range of depths between the maximum depth of penetration and the neutral height expected for an equivalent fluid thermal $Z_N = (2.6 \pm 0.4)Q^{1/4}N^{-1/2}$. In the small N, large N_s limit, one expects fallout to be uninfluenced by the ambient stratification and so to arise at a height appropriate for a homogeneous ambient. The dashed line in figure 2-9 corresponds to the homogeneous fallout height, equation (2.15), with a value of $C_3 = 3.77$ appropriate for particles with $Re_p > 12$.

The computed dependence of the fallout height on N_s appears in figure 2-9 as a solid curve. The numerical simulations indicate that the transition from the stratified to the homogeneous fallout height occurs at approximately $N_s = 2$. A plausible explanation for the discrepancy between the numerics and experiments evident in figure 2-9 is a weak dependence of the entrainment coefficient α on the particle size, as is evident from figure 2-9, where α is seen to decrease weakly with increasing Re_p. A smaller entrainment coefficient implies that the cloud buoyancy is reduced relatively slowly: the cloud thus travels faster, and the fallout height increases. This trend is evident in the homogeneous results of figure 2-6: smaller and larger particles have fallout heights that are systematically lower and higher, respectively, than would arise if the entrainment coefficient were independent of particle Reynolds number. A similar trend can be observed in the experiments of Noh & Fernando (1993). In figure 2-9, the numerical simulations, where $\alpha = 0.25$ was considered to be constant, thus systematically underpredict the fallout heights of the larger particles (larger N_s values). The dashed line in figure 2-9 indicates the fallout heights predicted numerically with an entrainment coefficient $\alpha = 0.17$, the mean value appropriate for $12 < Re_p < 44$. This discrepancy emphasises the need for further investigation of the factors influencing the magnitude of the entrainment into particle clouds. However, even with a constant value of $\alpha = 0.25$, our model yields general agreement with experimental data.

2.5.1 Rebound Height

The fate of the fluid that comes into contact with the particulate matter may have considerable environmental significance if the particulate matter is contaminated. When the particles fall out of the cloud in a stratified ambient, the fluid contained in the cloud is buoyant relative to the ambient, and so ascends to its rebound height

where it intrudes. We here present a simple calculation which yields a new relation between the rebound and fallout heights (Z_R and Z_f respectively).

The volume of the cloud, $V(z)$, in the thermal regime is given by

$$V(z) = C_4 \alpha^3 z^3 \ , \tag{2.17}$$

where C_4 is a constant shape factor, and we assume that the cloud is sufficiently far from the point of release that V_0 is negligible. In a linear stratification, $\rho_f = \rho_0(1 + N^2/gz)$, the rate of change of the total mass of the thermal, $M(z)$, with depth is given by

$$d_z M = \rho(z) d_z V = C_4 3 \alpha^3 z^2 \rho_0 (1 + N^2/gz) \ . \tag{2.18}$$

Integration yields the mass of the particle cloud in its thermal phase as a function of z:

$$M(z) = M_0 + C_4 3 \alpha^3 \rho_0 \left(\frac{z^3}{3} + \frac{N^2 z^4}{4g} \right) \ . \tag{2.19}$$

If we consider that the initial mass of the cloud was entirely due to particles, the density of fluid within the particle cloud at a height z is

$$\rho_c(z) = \frac{M(z) - M_0}{V(z)} = \frac{3 C_4 \alpha^3 \rho_0 (\frac{z^3}{3} + \frac{N^2 z^4}{4g})}{C_4 \alpha^3 z^3} \ . \tag{2.20}$$

The density of the fluid contained in the cloud thus increases with depth at a rate corresponding to 3/4 of that of the ambient:

$$\rho_c(z) = \rho_0 \left(1 + \frac{3N^2}{4g} z \right) \ . \tag{2.21}$$

This simple dependence allows us to relate the rebound height to the fallout height. For simplicity, we assume that the fluid that remains following fallout does not mix with the ambient during its ascent. It should then rebound to a height

$$Z_R = \frac{3}{4} Z_f \ . \tag{2.22}$$

While Luketina & Wilkinson (1994), did not present their data in such a way that one can infer the relative magnitudes of Z_R and Z_f in their experiments, it is noteworthy that the one experiment presented in their figure 2 is reasonably well described by relation (2.22).

In our experiments, Z_R was taken as the mean height of the neutral cloud resulting from the intrusion of the rebounded fluid, while the observed fallout height, $Z_f^o = (1 + \alpha\eta) Z_f$ was taken as the base of the cloud at fallout, where $\eta \alpha Z_f$ corresponds to the thickness of the cloud at its fallout height. Our leading order result (2.22) thus becomes, in terms of the observed fallout height

$$Z_R = \frac{3}{4} Z_f = \frac{3}{4} \frac{1}{1 + \alpha\eta} Z_f^o \ \approx \ 0.63 Z_f^0 \ . \tag{2.23}$$

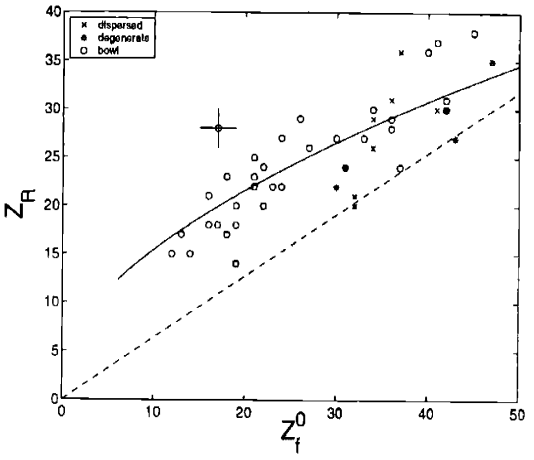

Figure 2-10: Dependence of the rebound height, Z_R on the observed fallout height, Z_f^0, for particle clouds in a stratified ambient. $\circ$ denotes a bowl fallout ($N_s > 1$); $\times$ denotes a dispersed fallout ($N_s < 1$); $\star$ denotes the intermediate cases. The dashed line is the theoretical prediction $Z_r = 3/4 Z_f \approx 0.63 Z_f^0$. The solid line indicates the results of the numerical simulations including entrainment after fallout.

This relation between the rebound and fallout height appears as the dashed line in figure 2-10 along with the the observed relation between the fallout and rebound heights for both bowl and dispersed fallouts. The fact that Z_R typically exceeds the predicted value of $\frac{3}{4} Z_f = 0.63 Z_f^o$ is consistent with the rebounding cloud entraining relatively dense fluid as it overshoots Z_f, and also as it ascends to its rebound height.

We used our numerical model to investigate the influence of entrainment following fallout. One expects that, as the cloud overshoots and rebounds, it will entrain surrounding fluid, but that owing to reduced cloud speeds, the entrainment coefficient α may be diminished. The case of no entrainment $\alpha = 0$ reproduces the theoretical prediction (2.23), and is represented by the dashed curve in figure 2-10. The case of $\alpha = 0.25$ is represented by the solid curve which agrees well with our data. Our results thus indicate that $\alpha = 0.25$ is a good estimate even as the cloud overshoots then ascends to its rebound height.

2.6 Discussion

In this chapter, we have described the evolution of heavy particle clouds in homogeneous and stratified fluids. In a homogeneous ambient, the particle cloud descends as a fluid thermal until reaching its fallout height, Z_f, where the particles settle out of the cloud in the form of a bowl-shaped swarm. After fallout, the entrained fluid continues its downward motion behind the particle swarm and evolves as a neutrally buoyant vortex ring. The deposit resulting from a discrete release of particles in a stratified fluid depends on the relative magnitudes of depth of the container h, the fallout height and the stratified cloud number $N_s = U_s Q_0^{-1/4} N^{-1/2}$. For $N_s > 1$,

		Localised deposit	Dispersed deposit	Ring deposit
Uniform environment	$Re_p > 0.15$	$Q < \frac{(U_s b_0)^2}{12}\left(\frac{h}{b_0}\right)^{-0.68}$	NA	$Q > \frac{(U_s b_0)^2}{12}\left(\frac{h}{b_0}\right)^{-0.68}$
	$Re_p > 4$	$N_p < \frac{1}{81}\left(\frac{h}{a}\right)^2$	NA	$N_p > \frac{1}{81}\left(\frac{h}{a}\right)^2$
Stratified environment	$N_s < 1$	NA	$Q < \frac{1}{6}\, h^4 N^2$	$Q > \frac{1}{6}\, h^4 N^2$
	$N_s > 2$	$h > 3.5\frac{Q^{1/4}}{N^{1/2}} - 0.5\frac{U_s}{N}$	NA	$h < 3.5\frac{Q^{1/4}}{N^{1/2}} - 0.5\frac{U_s}{N}$

Table 2.2: Criteria for the three modes of particle deposition: a localised deposit, a dispersed deposit, and a ring deposit arising from the cloud colliding with the bottom prior to fallout. Criteria are expressed in terms of the initial cloud buoyancy Q, particle radius a, initial cloud radius b_0, fluid viscosity ν, layer depth h, reduced gravity of the particles g' and Brunt Väisälä frequency N. For large N_s, the homogeneous criteria become relevant. NA denotes 'not applicable'.

particles fall out before the cloud reaches its neutral buoyancy height and descend as a swarm with little or no spread following fallout (Bühler & Papantoniou 1999). This gives rise to a localised deposit, provided fallout occurs before the cloud reaches the bottom of the container. After fallout, fluid entrained by the particle cloud ascends and intrudes at a rebound height, Z_R, somewhat less than $\frac{3}{4}Z_f$. For $N_s < 1$, the particles settle out in an irregular fashion at a depth between the intrusion height of an equivalent fluid thermal, Z_N, and the maximum penetration depth. This gives rise to a relatively broad deposit on the lower boundary. Again, entrained fluid ascends to, and intrudes at, a height slightly less than $\frac{3}{4}Z_N$. When particles fall out from the base of the spreading neutral cloud, they may not settle as individuals; rather, a convective instability initiated at the base of the cloud by the presence of a region of high particle concentration overlying a particle–free region may prompt the emergence of microscale particle–laden plumes. The dynamics of convective sedimentation from a gravity current (Maxworthy 1999), therefore play an important role in the resulting deposit and settling rate of the particles.

Finally, for both homogeneous and stratified ambients, if $h < Z_f$, the cloud maintains its thermal form throughout its descent. It consequently collides with the lower boundary as a turbulent vortex ring. The dynamics of motion are expected to be similar to those of atmospheric microbursts (Linden & Simpson 1985), where vortex

stretching in the expanding vortex ring may generate high flow speeds. In the context of barge dumping at sea, such vigorous motions may lead to scouring and resuspension of particulate material from the sea floor, and thus leave a ring-shaped deposit. This scenario has been observed in the two-dimensional study of Nakatsuji *et al.* (1990). In a stratified ambient, the height of ascent of the cloud fluid following particle settling will depend on the entrainment induced following contact with the bottom boundary. If this entrainment is small, the fluid will ascend to a depth slightly less than $\frac{3}{4}h$. The dependence of particle–laden gravity currents, as may emerge from the collision of the particle cloud with the lower boundary will be considered in chapter 3.

Our study thus distinguishes between three distinct modes of particle deposition, as summarised in table 2.2. Note that the dispersed deposits may only arise in a stratified environment. We note that other factors such as polydispersity, flocculation and reaction with the ambient may be important in the dumping of solid material. Moreover, while our experiments have yielded robust scalings describing the dynamics of particle clouds and their subsequent deposition patterns, they also underlined the indeterminacy in the numerical coefficients introduced by the influence of the ballistic phase and the variability of the entrainment coefficient. In suggesting a weak dependence of α on Re_p such as that evident in the study of Noh & Fernando (1993), our study motivates further experimental studies of the factors influencing entrainment into particle clouds. The source conditions, such as whether the particulate matter is wet or dry, may also influence the onset of self–similar cloud behaviour (Ruggaber 2000).

Finally, we have presented a system of ordinary differential equations describing particle cloud dynamics in homogeneous and stratified ambients that allow for efficient numerical simulation. The numerics has served to validate and determine the limitations of our leading order results deduced from simple theory and scaling arguments. The numerical model may be readily extended to describe more complex physical situations such as payloads composed of polydisperse particles and particles that react with the environment.

Chapter 3

Deposits resulting from particle–laden gravity currents

Particle–laden gravity currents arise in a wide variety of geophysical settings. For example the deposits left by turbidites have important geological implications and may be used to help locate oil and gas fields (Kneller 1995). The maximal distance traveled by masses of air laden with volcanic ash may be a great security concern (Sparks, Carey & Sigurdsson 1991). Mud flows (Simpson 1987) and crystal–laden flows in magma chambers (Irvine 1987) are examples of viscously dominated particle–laden gravity currents. Also, our study of particle clouds (chapter 2) has underlined the importance of particle–laden gravity currents in the context of the dumping of waste into rivers and oceans (Bühler & Papantoniou 1999). When a particle cloud reaches the bottom of the container while still in its thermal phase, its deposit is equivalent to that of a corresponding particle–laden gravity current. Being able to infer the properties of a current from its deposit, or conversely predict the deposit resulting from a gravity current with given properties is thus of primary importance.

Based on the classic works of Von Kármán (1940) and Benjamin (1972), particle–laden gravity currents have been studied numerically using the shallow–water equations (Bonnecaze, Huppert & Lister 1993). Using the similarity solution derived by Hoult (1972), Hogg, Ungarish & Huppert (2000) found solutions in the asymptotic limit of low particle concentration and justified the use of box–models by showing that they provide a valid leading order approximation of the flow properties and deposits of particle–laden gravity currents. These authors also derived an expression for the runout length, the maximal extent of the deposit, of turbulent particle–laden gravity currents. More recently, direct numerical simulations of two and three–dimensional particle–laden gravity currents have been performed (Hartel, Meiburg & Necker 2000), but are still limited to relatively low Reynolds numbers ($Re \leq 2000$).

Most natural and industrial particle–laden gravity currents involve polydisperse particles. The particle settling speed has a direct influence of the runout length of particle–laden gravity currents and the initial distributions of particle size and density are thus determinant in the evolution of the flow. As a first step towards understanding the influence of polydispersity, we focus in this chapter on the shape and particle distribution of deposits resulting from bidisperse particle–laden gravity

currents. Currents carrying more than one type of particles were studied numerically in some particular cases by Garcia (1994), and Bonnecaze, Huppert & Lister (1996) and the dependence of the volume fraction of different types of particles on distance from the source was examined. We extend these results to more general geometries (two–dimensional planar and three–dimensional axisymmetric) and initial conditions (fixed volume and constant volume flux).

We present here a computationally efficient model which allows for a qualitative description of deposits left by various types of gravity currents. We also derive new analytical results on the maximal length of deposits left by laminar gravity currents. We begin by describing the dynamics of gravity currents in §3.1. We discuss deposits left by turbulent and laminar gravity currents in §3.2 and §3.3 respectively. We present our conclusions in §3.4.

3.1 Dynamics of Gravity Currents

We begin by considering two-dimensional planar gravity currents of fixed volume spreading over a flat surface. The density difference between the current and the ambient fluid may be due to both compositional differences and the presence of particles. The dense fluid is initially confined by a lock and is released at time zero. The boundary condition at the top of the current is that no fluid may cross the interface

$$\frac{\partial h}{\partial t} = \vec{u} \cdot \vec{n} \approx -u(x, h(t), t)\frac{\partial h}{\partial x} + v(x, h(t), t) \tag{3.1}$$

where x is the horizontal coordinate, h the height of the gravity current, u the horizontal velocity field and v the vertical velocity field and we have assumed that the variations of $h(x,t)$ in the x direction are small compared to h. We consider fully turbulent flows, an assumption valid provided

$$Re = \frac{Uh}{\nu} > 1000 \tag{3.2}$$

where U and h are typical velocity and height scales and ν is the fluid viscosity (Simpson 1987). The horizontal velocity is then independent of height, as turbulence acts to eliminate any systematic variations with height. By considering an incompressible fluid, we may integrate the solenoidal condition $\nabla \cdot \vec{u} = 0$ with respect to y and find $v(x, h(t), t) = -h\frac{du}{dx}$, noting that u does not depend on y. The kinematic boundary condition may thus be expressed as

$$\frac{\partial h}{\partial t} + u(x,t)\frac{\partial h}{\partial x} + h\frac{\partial u}{\partial x} = 0 \tag{3.3}$$

We consider the pressure to be hydrostatic to first order (Simpson 1987), $P = g\Delta\rho z$, where $\Delta\rho$ stands for the difference between the density of the current, ρ_{gc} and the

ambient, ρ_f. Integrating the vertical Navier–Stokes momentum equation, yields

$$\frac{\partial(uh)}{\partial t} + \frac{\partial(u^2 h)}{\partial x} + \frac{1}{2}\frac{\partial(g\Delta\rho h^2)}{\partial x} = 0, \tag{3.4}$$

This equation is often referred to as the shallow–water equation (Kundu 1990). Note that the density difference between the ambient and the current, $\Delta\rho$, has contributions from the density differences between the ambient fluid and both the current fluid ρ_c and the particles ρ_p. If particles are present with particle fraction ϕ, we have

$$\Delta\rho = (\rho_c - \rho_f)(1-\phi) + \phi(\rho_p - \rho_f) \approx (\rho_c - \rho_f) + \phi(\rho_p - \rho_f) \tag{3.5}$$

We note that the first term of this difference is constant in time while the second term decays due to the sedimentation of particles, i.e. the secular decrease in ϕ. If $\rho_c - \rho_f \gg \phi(\rho_p - \rho_f)$, the presence of the particles is not dynamically significant; the particles are then passive tracers and are simply carried by the fluid. If conversely $\phi(\rho_p - \rho_f) \gg \rho_c - \rho_f$, particles drive the flow. These two limiting cases result in very different deposits.

Equations (3.3) and (3.4) are valid between $x = 0$ and $x = x_n$, the position of the nose of the current. The boundary condition at $x = 0$ is that the velocity is zero, due to the presence of a wall. We define the Froude number, Fr, such that the velocity at the front of the current u_n is given by

$$u_n = Fr\sqrt{g\Delta\rho h} \tag{3.6}$$

Von Kármán's analysis, based on an application of Bernouilli's equation for steady irrotational flows, showed that Fr remains constant. However, conservation of energy is not applicable here as was argued by Benjamin (1972), who went on to show that Von Kármán's results were nonetheless valid and found that $Fr = \sqrt{2}$ in the limit of a very deep ambient.

In the case of a constant $\Delta\rho$, a long term similarity solution was obtained by Hoult (1972):

$$x_n(t) = Kt^{2/3} \tag{3.7}$$

$$u(x,t) = \frac{2Ky}{3t^{1/3}} \tag{3.8}$$

$$h(x,t) = \frac{4K^2}{9t^{2/3}}\left(\frac{1}{Fr^2} - \frac{1}{4} + \frac{y^2}{4}\right) \tag{3.9}$$

$$K = \left(\frac{27Fr^2V}{12 - 2Fr^2}\right)^{1/3} \tag{3.10}$$

where V is the initial volume of the current. Notice that this solution assumes a constant volume, i.e. no entrainment. Experiments on a flat surface are seen to agree well with this solution for long times (Huppert & Simpson 1980). The so–called box–model is a helpful tool introduced to approximate flows which may not be described by this similarity solution, either because $\Delta\rho$ is time–dependent or because the initial

length of the current is comparable to its maximal extent. In box–models, the current height is assumed to be constant in space.

Huppert & Simpson (1980) used box–models to find expressions for $l(t)$, the length of the current, in different regimes. If we consider a two–dimensional gravity current dominated by inertia, we may obtain the time–dependence of the velocity from a simple scaling argument. Using our assumption that the gravity current is dominated by inertia, we have that $u^2 \sim g\Delta\rho h$. Combining this with the approximation $u \sim l/t$ and $V = lh$ for a planar two–dimensional current, we find that the velocity of the nose scales like $u_n(t) \sim (Vg\Delta\rho)^{1/3}t^{-1/3}$. The relevant coefficient is found by balancing the dynamic pressure at the nose with the difference of hydrostatic pressures far up and downstream and yields (Simpson 1987)

$$u_n(t) = \sqrt{2}(Vg\Delta\rho)^{1/3}t^{-1/3}. \tag{3.11}$$

Experimental results yield a smaller value of this constant, typically about 1.19 (Huppert & Simpson 1980).

Similarly, if the spread of the gravity current is radial, an expression for the velocity of the front may be found by dimensional analysis. The current volume is now given by $V \sim l^2h$, where l is the radius of the current. Approximating again $u \sim l/t$ and considering inertially dominated currents, $u^2 \sim g\Delta\rho h$, we find

$$u_n(t) = \sqrt{2}(g\Delta\rho V)^{1/4}t^{-1/2}. \tag{3.12}$$

Experimental results again lead to a smaller constant of about 1.3 (Huppert & Simpson 1980).

3.1.1 Sedimentation from a turbulent ambient

If the Reynolds number of the current is large, $Re = uh/\nu > 1000$, the flow is fully turbulent and particles are evenly distributed in the vertical direction. We consider small Reynolds number particles, $Re_p = U_s a/\nu \ll 1$, with a and U_s the particle radius and settling speed respectively, so that the vertical velocities generated by turbulence are much greater than the settling speed of the particles. In this case, following Bonnecaze *et al.* (1993), we may apply the results of Martin & Nokes (1988), who developed models describing particle settling through a turbulent fluid in a bound container.

The main assumption of Martin & Nokes (1988) is that fluid is well mixed everywhere, except in a thin boundary layer along the bottom of the container. Only in this layer may particles settle out of suspension because the turbulence is not sufficiently vigorous. The volume flux of particles out of the suspension is thus proportional to the area of the base, A, the particle settling speed, U_s, and particle volume fraction at the base $\phi(0)$. We consider that turbulent motions are sufficiently vigorous that the volume fraction is uniform in the vertical direction and thus $\phi(0) = \phi$ and find

$$v_p\frac{dN}{dt} = -AU_s\phi \tag{3.13}$$

where N is the volume of particles and v_p the volume of one particle. Using $\phi = v_p N/(Ah)$, with h the height of the fluid, we have:

$$\frac{d\phi}{dt} = -\frac{U_s \phi}{h} \tag{3.14}$$

The height of the deposit, H, is proportional to the number of particles having settled out of suspension $H = \gamma(N_0 - N)/A$, where the constant N_0 is the initial number of particles and γ depends only on the details of the packing. The growth rate of the deposit is thus

$$\frac{dH}{dt} = \gamma U_s \phi. \tag{3.15}$$

In the case of a spreading gravity current, the time derivative of equation (3.14) is replaced by a material derivative:

$$\frac{D\phi}{Dt} = \frac{d\phi}{dt} + u\frac{d\phi}{dx} = -\frac{U_s \phi}{h} \tag{3.16}$$

where u represents the horizontal velocity of the fluid. The expression for the height of the deposit remains the same as the deposit is not transported by the fluid.

Equations (3.13-3.16) highlight the dependence of the deposit height on the particle settling speed. In the presence of different kinds of particles, the deposition pattern will necessarily depend on their individual settling speeds. We consider low particle concentrations (i.e. $\phi \lessapprox 1\%$) so that the interaction between particles is negligible and we may deduce more compact analytical expressions. However, numerical simulations may readily be extended to consider the influence of hindered settling.

3.2 Deposition from a Turbulent Gravity Current

We consider in turn a number of special cases. In §3.2.1, we study the deposits left when a constant flux of particle–laden fluid leads to spreading in a rectangular geometry. This case corresponds to sediment–laden rivers, for which the flux varies slowly in time. In §3.2.2 we examine the sudden release of a finite volume of particle–laden fluid. This scenario provides a leading order description of the progression of turbidites and underwater landslides.

3.2.1 Constant Flux

We first consider a flow driven by a constant flux of particle–laden fluid, Q. We consider steady flows, i.e. time–independent, where the flux and height of the current are constant, as would be the case in particle–laden rivers. After a transient period of order h/U_s, the particle concentration remains steady and equation (3.16) becomes:

$$u\frac{d\phi}{dx} = -\frac{U_s \phi}{h} \tag{3.17}$$

The particle concentration thus decays with distance from the source as particles settle to the bottom. Because both the volume flux Q and current height u are constant, the velocity of the current $u = Q/h$ is also constant and the solution is readily found to be:

$$\phi(x) = \phi_0 e^{\frac{-U_s x}{Q}} \tag{3.18}$$

where ϕ_0 is the initial concentration of sediment.

To find the deposition pattern from a bidisperse gravity current, we consider each type separately to find that the concentration of particles of type I and II left in suspension at a distance x from the source is

$$\phi_I(x) = \phi_I^0 e^{\frac{-U_I x}{Q}} \tag{3.19}$$

$$\phi_{II}(x) = \phi_{II}^0 e^{\frac{-U_{II} x}{Q}} \tag{3.20}$$

where U_I and U_{II} are the settling speeds corresponding to particles of types I and II. In the deposit, at any given time the contributions to the height of accumulated sediment are respectively $U_I\phi_I$ and $U_{II}\phi_{II}$. Since the flow is steady, the height has the particularly simple form

$$H(x,t) = (U_I\phi_I(x) + U_{II}\phi_{II}(x))\gamma t. \tag{3.21}$$

The fraction of particles I in the deposit at any given point, x, is:

$$X_I(x) = \frac{U_I\phi_I^0 e^{\frac{-U_I x}{Q}}}{U_I\phi_I^0 e^{\frac{-U_I x}{Q}} + U_{II}\phi_{II}^0 e^{\frac{-U_{II} x}{Q}}}. \tag{3.22}$$

We thus see that the only parameters influencing the form of the deposit are U_I, U_{II}, ϕ_I^0, ϕ_{II}^0 and the volume flux Q. It is straightforward to extend this to n different types of particles

$$X_k(x) = \frac{U_k\phi_k^0 e^{\frac{-U_k x}{Q}}}{\sum_{i=1}^{n} U_i\phi_i^0 e^{\frac{-U_i x}{Q}}}. \tag{3.23}$$

A continuous distribution of particles may be studied by considering the limit of a large n. The denominator then becomes an integral which needs to be evaluated numerically for most distributions of particles. As it appears that there is little understanding to be gained from doing so, we confine ourselves to the bidisperse limit.

Theoretically, the deposit has infinite length, although effectively particles are absent after a typical length scale given by the volume flux divided by the settling speed $l_\infty \approx Q/U_s$. The form of the deposit left by a gravity current generated by a constant source flux and carrying two different types of particles is shown in figure 3-1. In this simulation, $\phi_I^0 = \phi_{II}^0 = 0.5\%$, $\rho_p/2 = \rho_c = \rho_f = 1\text{g/cc}$ and the particle radii, a, satisfies $a_I = 2a_{II} = 20\mu\text{m}$. Each point of the deposit was plotted as a circle or a dot with a probability corresponding to the local particle fraction of particles

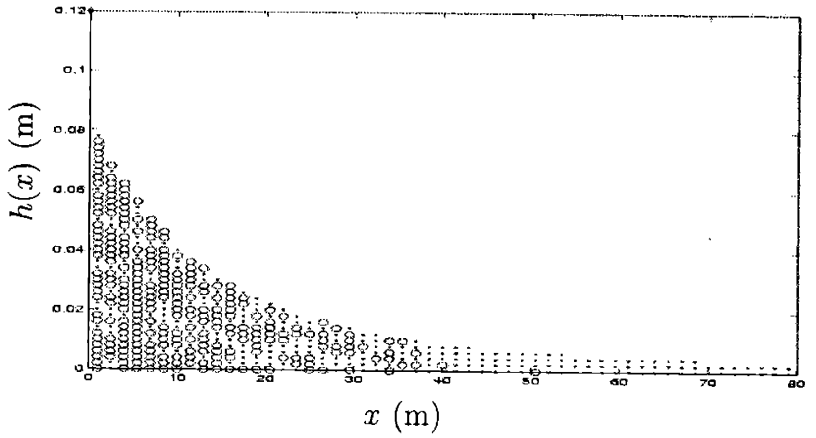

Figure 3-1: The dependence of deposit height, $h(x)$, on distance, x, from the point of release of a bidisperse turbulent planar gravity current generated by a constant flux $Q = 1\text{m}^2/\text{s}$. Initial conditions are: $\phi_I^0 = \phi_{II}^0 = 0.5\%$, $\rho_p/2 = \rho_c = \rho_f = 1\text{g/cc}$ and $a_I = 2a_{II} = 20\mu\text{m}$. Circles correspond to high particle fractions of large particles (I) and points to high particle fraction of small particles (II). The height of the deposit increases uniformly in time.

of type I and II respectively. The concentration of each particle is seen to decay exponentially with distance from the source, with that of smaller particles decaying more slowly, as expected from equations (3.19) and (3.20).

3.2.2 Constant Volume

We now consider the release of a constant volume of particle–laden fluid where the interstitial fluid is the same as that in the ambient, $\rho_c = \rho_f$. The density difference then depends only on the particle concentration: $\Delta\rho = \phi(\rho_p - \rho)$. To simplify notation, we define g' as $g' = g(\rho_p - \rho_f)/\rho_f$ and $g'\phi$ is now the driving force of the flow. The three equations describing the flow, (3.16), (3.3) and (3.4) have to be solved numerically in order to find a complete solution (Bonnecaze *et al.* 1993). In the limit of deep surroundings, the shape of the deposit depends only weakly on the density of the interstitial fluid in the gravity current, ρ_c. However, the velocity of the gravity current is qualitatively different for cases of $\rho_c > \rho_f$ and $\rho_c = \rho_f$. In the latter case, the driving force is only due to the presence of particles and decreases with time. The current then only has a finite length, at which point all the particles have been deposited. The runout length may be expressed analytically using a box–model (Hogg, Ungarish & Huppert 2000)

$$V = hl \tag{3.24}$$

$$\frac{d\phi}{dt} = \frac{-U_s\phi}{h} = \frac{-U_s\phi l}{V} \tag{3.25}$$

$$\frac{dl}{dt} = Fr\sqrt{g'\phi h} = Fr\sqrt{\frac{g'\phi V}{l}}. \tag{3.26}$$

where the Froude number, Fr is again assumed to be a constant. Dividing equation (3.25) by equation (3.26) yields

$$\frac{d\phi}{dl} = \frac{-U_s\sqrt{\phi l^3}\rho}{Fr\sqrt{g'V^3}} = -\lambda\sqrt{\phi l^3} \tag{3.27}$$

where $\lambda = \frac{U_s}{Fr(g'V^3)^{1/2}}$. Equation (3.27) may be solved using the condition that $\phi = \phi_0$ at $l = 0$, and yields

$$\phi^{1/2} = \phi_0^{1/2} - \frac{\lambda l^{5/2}}{5} \tag{3.28}$$

The maximal extent of the current is found by setting $\phi = 0$ and yields $l_\infty = (5\phi_0^{1/2}/\lambda)^{2/5}$. An expression for the height of the deposit, H, as a function of position may also be found analytically. The flux of particles out of the suspension is $U_s\phi$ and so

$$\frac{dH}{dl} = \frac{dH}{dt}\frac{dt}{dl} = \gamma\lambda V(\phi l)^{1/2} \tag{3.29}$$

$$H(l) = \int_l^{l_\infty} V\gamma\lambda(\frac{\lambda}{5}l'^3 - \sqrt{\phi_0 l'})dl'. \tag{3.30}$$

If we introduce $\xi = l/l_\infty$, the height of the deposit is then (Hogg, Ungarish & Huppert 2000)

$$H(\xi) = \frac{25\phi_0 V\gamma}{12 l_\infty}\left(1 - \frac{8}{5}\xi^{3/2} + \frac{3}{5}\xi^4\right). \tag{3.31}$$

Notice that equations (3.24-3.26) have a singularity as $t \to 0$. Comparing this theory with experiments is thus only possible at long times, when the flow has relaxed from its initial conditions to its assumed self–similar form.

It is worth mentioning that, despite the fact that no similarity solution exists for the full problem of the particle driven flow, asymptotic solutions have been found by Hogg, Ungarish & Huppert (2000). The similarity solution of Hoult (1972) and a constant volume fraction of particles are used as a background state. One then proceeds to expand (3.24-3.26) in terms of the small parameter $\tau = K^{-2}t^{5/3}U_s/(Vg'^2)^{1/4}$, where the term $(Vg'^2)^{1/4}$ is a reference velocity. This asymptotic expansion yields the conclusion that the box–model actually has a much larger range of validity than might be first expected, therefore justifying its use in many applications.

The cases of bidisperse currents, or of $\rho_c \neq \rho_f$ may not be solved in closed form, and we perform simple numerical integrations instead. We first express the concentration, ϕ, in terms of the height of the gravity current. Using the box–model, we have $u(x,t) = xu_n(t)/l(t)$ so that (3.16) becomes

$$\frac{d\phi}{dt} + \frac{xu_n(t)}{l(t)}\frac{d\phi}{dx} = -\frac{\phi U_s}{h(t)} \tag{3.32}$$

Equivalently, we may solve the system of equations

$$\frac{dt}{1} = \frac{l(t)dx}{xu_n(t)} = -\frac{h(t)d\phi}{\phi U_s} \tag{3.33}$$

We note that $l'(t) = u_n(t)$; therefore, solving the first equality yields:

$$\log x = \log l(t) + \log(K_1) \tag{3.34}$$

$$\frac{x}{l(t)} = K_1 \tag{3.35}$$

It is also straightforward to solve for the first and third terms of (3.33) to find

$$\phi e^{U_s \int_0^t 1/h(s)ds} = K_2 \tag{3.36}$$

so that the general solution is

$$\phi(x,t) = e^{-U_s \int_0^t 1/h(s)ds} F(x/l(t)) \tag{3.37}$$

where $F(x/l(t))$ is determined by the initial conditions. Assuming that the initial concentration of sediment is uniform yields $\phi(x,t) = \phi_0 e^{-U_s \int_0^t 1/h(s)ds}$. The deposit still obeys (3.15):

$$H(x,t) = \int_0^t \gamma U_s \phi_0 e^{-U_s \int_0^t 1/h(s)ds} dt. \tag{3.38}$$

This equation may be solved numerically, along with equation (3.26), and the results are shown in figure 3-2. Here we show the deposit resulting from a current containing two types of particles with $\phi_I^0 = \phi_{II}^0 = 0.5\%$, $\rho_p/2 = \rho_c = \rho_f = 1\text{g/cc}$ and $a_I = 2a_{II} = 20\mu\text{m}$. The final deposit once again has a finite length. The particles show a more uniform distribution than in the case of a constant volume flux. For a fixed volume, the height of the deposit initially decays relatively slowly, leading to a convex deposit. Experiments have been done in this setting by Gladstone, Phillips & Sparks (1998) and their results exhibit a maximum deposition located between 1/4 and 1/3 of the runout length of the current. This discrepancy between experiments and simulations is thought to be due to the vigourous stirring used to maintain particles in suspension before the opening of the gate (Moodie 2000). Box–model simulations of monodisperse gravity currents have been compared with experiment by Hallworth, Hogg & Huppert (1998) which also exhibit a local maximum and good agreement was found away from the point of release. Similar results were found by Garcia (1994) when the current initially propagated down a slope of small angle before coming to rest over a horizontal bed. The comparison between the experiments of Gladstone, Phillips & Sparks (1988) and our simulations is thus made more difficult, but good qualitative agreement in the shape of the deposit past the point of maximal deposit is found.

It should be noted that all the previous experiments describe the total height and particle fraction as a function of distance from the source, but not the dependence of

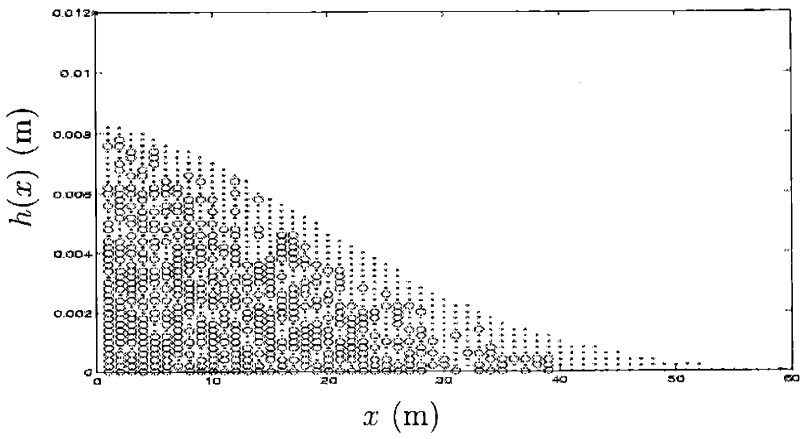

Figure 3-2: The dependence of the deposit height, $h(x)$, on distance, x, from the release point for a turbulent fixed volume bidisperse gravity current. Initial conditions are: $\phi_I^0 = \phi_{II}^0 = 0.5\%$, $\rho_p/2 = \rho_c = \rho_f = 1\text{g/cc}$ and $a_I = 2a_{II} = 20\mu\text{m}$ and the initial volume is 10m^2. Circles correspond to high particle fractions of large particles (I) and points to high particle fraction of small particles (II), the latter propagating further as they remain in suspension longer.

the distribution of particles on the height within the deposit. An empirical relation describing the total height of the deposit was suggested by Bonnecaze *et al.* (1996); based on the numerical prediction for one type of particles, they predicted the sum of the different contributions. No information about the structure of the deposit was provided. In contrast, our simulations clearly show not only the particle fraction of each type of particle but also their distribution with height.

Our model also allows us to simulate currents where the ambient fluid is lighter than fluid within the current. Figure 3-3 shows the deposit resulting from a gravity current where the density of the fluid in the current $\rho_c = 1.1\text{g/cc}$ is greater than of the ambient $\rho_f = 1\text{g/cc}$. The particles are not dynamically significant here, accounting only for 1% of the initial density difference between the current and ambient. In this configuration, the deposit theoretically has an infinite length, and the concentration decays exponentially with distance from the source. The particles travel further downstream than in previous examples, because the driving force does not decay as significantly. The maximum height of the deposit is also reduced, since the particles are distributed over a greater distance. Note that here the initial number of particles has been reduced by a factor of ten compared to previous simulations in order to ensure that they are not dynamically significant, thus leading to a smaller total deposit. From our model, it is straightforward to consider intermediate cases where a prescribed fraction of the density difference is due to particles.

A similar analysis may be done in the case where viscous forces dominate inertial forces in resisting the spreading of the current. The transition from inertially to viscously dominated gravity currents occurs when viscous and inertial forces are of the same order, that is, when the terms U^2/l and $\nu U/h^2$ have the same magnitude. For two-dimensional gravity currents, we find using (3.11) that the transition time

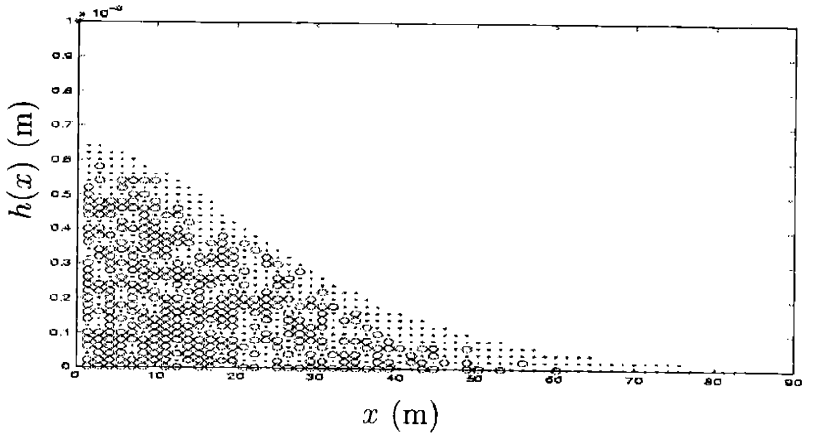

Figure 3-3: Dependence of the deposit height, $h(x)$, on distance, x, from the point of release of a fixed volume, bidisperse turbulent particle–laden gravity current where the density of the fluid in the current is greater than of the ambient, $\rho_c = 1.1\rho_f$. Here the initial volume is 10m^2 and $\phi_I^0 = \phi_{II}^0 = 0.05\%$ so that particles are not dynamically significant. Circles correspond to high particle fractions of large particles (I) and points to high particle fraction of small particles (II).

is of the order of $t_{cr} \sim (V^4/\nu^3 g^2)^{1/7}$. We now proceed to study the deposits left by laminar gravity currents, a limit expected to be relevant for $t > t_{cr}$.

3.3 Deposits from a laminar flow

3.3.1 Constant Flux

The case of a laminar flow is very different from the turbulent one. We consider that the velocity of the particles is $u_p = \vec{u} - U_s\hat{k}$. If both the flux Q and the height of the current h are constant, there is no vertical velocity component so that the height of the suspension following the flow is $h_s = h - U_s t$. Assuming steady flow, the time component may be replaced by the distance from the source divided by the velocity of the current $t \to x/u$. This gives rise to a deposit with a profile considerably different from turbulent currents, as shown in figure 3-4. In this simulation, $Q = 10\text{m}^2/\text{s}$ and $\phi_I^0 = \phi_{II}^0 = 0.5\%$ with $a_I = 2a_{II} = 20\mu\text{m}$ and $\rho_p/2 = \rho_c = \rho_f = 1\text{g/cc}$. Here the particles are simply deposited at a distance that depends linearly on the height at which they started. If we assume the initial particle distribution to be uniform, the resulting deposit is also uniform and of finite length. Each type of particles is thus evenly distributed over a region of length Q/U_s.

3.3.2 Constant Volume

To consider the case of a constant volume release, we again make use of a box-model. The height of the current denoted previously by h no longer corresponds

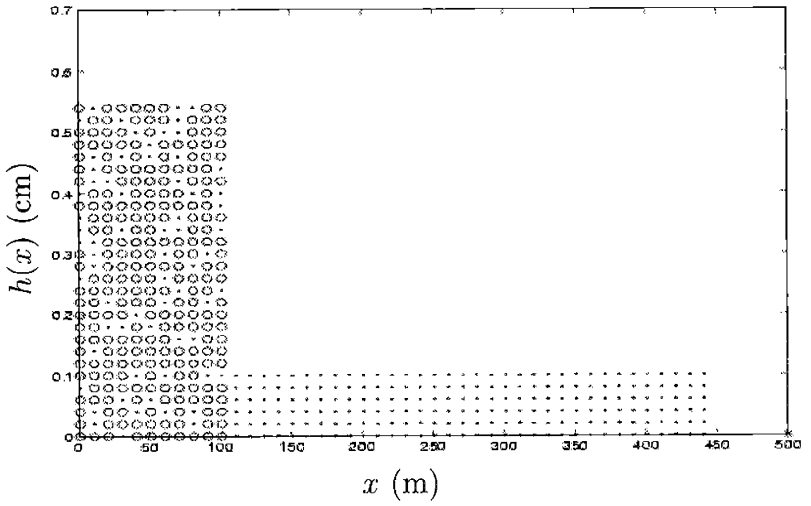

Figure 3-4: The dependence of the height of the deposit, $h(x)$, on distance from the source, x, of a laminar, constant volume flux ($Q = 10\text{m}^2/\text{s}$) bidisperse particle–laden gravity current. Particles are initially present in equal concentration, $\phi_I^0 = \phi_{II}^0 = 0.5\%$ with $a_I = 2a_{II} = 20\mu\text{m}$ and $\rho_p/2 = \rho_c = \rho_f = 1\text{g/cc}$. Circles correspond to high particle fractions of large particles (I) and points to high particle fraction of small particles (II). The height of the deposit increases uniformly in time.

to the height of the suspension, h_s, as particles now settle relative to fluid in the current. The height appearing in equation (3.26) and driving the flow is now that of the suspension. Assuming the flow is laminar and using a box–model, we deduce the horizontal, u, and vertical, v velocity components of the flow:

$$u = \frac{u_n(t)x}{l(t)} \tag{3.39}$$

$$v = -\frac{u_n(t)y}{l(t)} \tag{3.40}$$

Using the flow field given by (3.39-3.40) yields an expression for $h_s(t)$

$$\frac{dh_s}{dt} = v(h_s) - U_s = -\frac{u_n(t)h_s(t)}{l(t)} - U_s. \tag{3.41}$$

and solving for h_s yields

$$h_s = h - U_s\frac{\int_0^t l(t')dt'}{l(t)}. \tag{3.42}$$

Unlike the turbulent case, the concentration of particles will remain constant within the suspension.

To deduce the evolution of the deposit height, we need to know the flux of particles out of the suspension. Considering the whole current, we get an equation for the total

number of particles in suspension:

$$\frac{d(\phi l h_s)}{dt} = -\frac{d(\phi_0 l(h - U_s \frac{\int_0^t l(t')dt'}{l(t)}))}{dt} \tag{3.43}$$

$$= -\phi_0 \frac{d(V - U_s \int_0^t l(t')dt')}{dt} = -\phi_0 U_s l. \tag{3.44}$$

Equation (3.44) may be made into a local statement by noting that it represents the integral of particles locally leaving the suspension between 0 and l. Since the particle concentration remains uniform, we find that the height of the deposit satisfies

$$\frac{dH}{dt} = \gamma \phi_0 U_s. \tag{3.45}$$

We thus have the same governing equation for the height of the deposit as in the case of a turbulent ambient, but the concentration now remains constant until a critical time t^* such that $h_s(t^*) = 0$, at which point all the particles have settled out of suspension.

We derive an expression for the total length of the current using equation (3.26) with h_s now replacing h, and with a constant particle concentration $\phi = \phi_0$,

$$\frac{dl}{dt} = Fr\sqrt{g'\phi_0 \left(h - U_s \frac{\int l dt}{l}\right)} \tag{3.46}$$

$$= Fr\sqrt{g'\phi_0 \left(\frac{V - U_s \int l dt}{l}\right)} \tag{3.47}$$

We define $m(t) = \int_0^t l(t)dt$ and $\Phi = Frg'^{1/2}\phi_0^{1/2}V^{1/4}U_s^{-1}$, and non-dimensionalize length by $V^{1/2}$ and time by $V^{1/2}/U_s$ in order to obtain

$$\sqrt{m'}m'' = \Phi\sqrt{1-m} \tag{3.48}$$

The initial conditions are $m(0) = 0$, $m'(0) = 0$. We deduce the runout length by computing the value of $m'(\bar{x})$ for which the current stops, i.e where $m''(\bar{x}) = 0$. Multiplying equation (3.48) by m' and integrating yields

$$\frac{2}{5}m'^{5/2} = \frac{2}{3}\Phi(1 - (1-m)^{3/2}) \tag{3.49}$$

$$m' = \left(\frac{5}{3}\Phi(1 - (1-m)^{3/2}\right)^{2/5} \tag{3.50}$$

When the currents stops, $m = 1$ (because $m'' = 0$) and we find $m'(\bar{x}) = (5/3)^{2/5}\Phi^{2/5}$ which in dimensional form translates to

$$l_\infty = (5/3)^{2/5}\frac{\phi_0^{1/5}V^{3/5}g'^{1/5}Fr^{2/5}}{U_s^{2/5}} \tag{3.51}$$

		Const. Volume, V	Const. Flux, Q	Reference
Laminar	2–D	$1.23\left(\frac{\phi_0 V^3 g' Fr^2}{U_s^2}\right)^{1/5}$	$\frac{Q}{U_s}$	Present study
	3–D	$1.19\left(\frac{\phi_0 V^3 g' Fr^2}{U_s^2 \pi^3}\right)^{1/8}$	$\left(\frac{Q}{\pi U_s}\right)^{1/2}$	
Turbulent	2–D	$1.90\left(\frac{\phi_0 V^3 g' Fr^2}{U_s^2}\right)^{1/5}$	$O(Q/U_s)$	Hogg *et al.* (2000)
	3–D	$1.28\left(\frac{\phi_0 V^3 g' Fr^2}{U_s^2 \pi^3}\right)^{1/8}$	$O(Q/(\pi U_s))^{1/2}$	

Table 3.1: Runout length of monodisperse particle–driven gravity currents as estimated with a box–model. Here ϕ_0 is the initial particle concentration, $g' = (\rho_p - \rho_f)/\rho_f$ is the reduced gravity, Fr is the Froude number taken to be constant and U_s is the particle settling speed.

The runout lengths of deposits resulting from turbulent and laminar gravity currents are summarized in table 3.1. Similar computations have been performed for axisymmetric currents; the results are included in table 3.1.

The results of a numerical simulation of a laminar, fixed volume bidisperse gravity current are presented in figure 3-5. Here the initial particle concentrations are equal, $\phi_I^0 = \phi_{II}^0$, $\rho_p/2 = \rho_c = \rho_f$ and $a_I = 2a_{II}$. The shape is now more rounded and the separation between the two types of particles more clearly marked than for turbulent gravity currents.

By combining the turbulent and laminar cases, it is possible to deduce a complete description of the deposition pattern from the gravity current. Estimating the Reynolds number of the current allows one to determine whether the flow is predominantly turbulent or laminar. The transition between those two is expected to occurs when the Reynolds number of the flow $Re = uh/\nu$ falls below a critical value, typically of the order of 1000. We consider a simplified model where the flow is turbulent if $Re > 1000$ and laminar otherwise. Because the velocity of the current is zero at the vertical wall, the Reynolds number increases away from the source. There will therefore always be a region near the vertical wall where the velocity of the current is sufficiently small that the current is laminar. This region grows and eventually covers the whole current. For the sake of simplicity, we assume that the transition between turbulent and laminar flow occurs at a critical Reynolds number, Re_c, from which we find that the transition point is

$$\frac{x_{cr}}{l(t)} = \frac{Re_c \nu}{h(t) u_n(t)} \tag{3.52}$$

Using the laminar model for $x < x_{cr}$, and the turbulent model for $x > x_{cr}$, we are now able to obtain a description of the whole current. A simulation showing a gravity current where the front is turbulent while the region near the vertical wall is laminar is shown in figure 3-6. In this case, $\phi_I^0 = \phi_{II}^0 = 0.5\%$, $\rho_p/2 = \rho_c = \rho_f = 1\text{g/cc}$ and

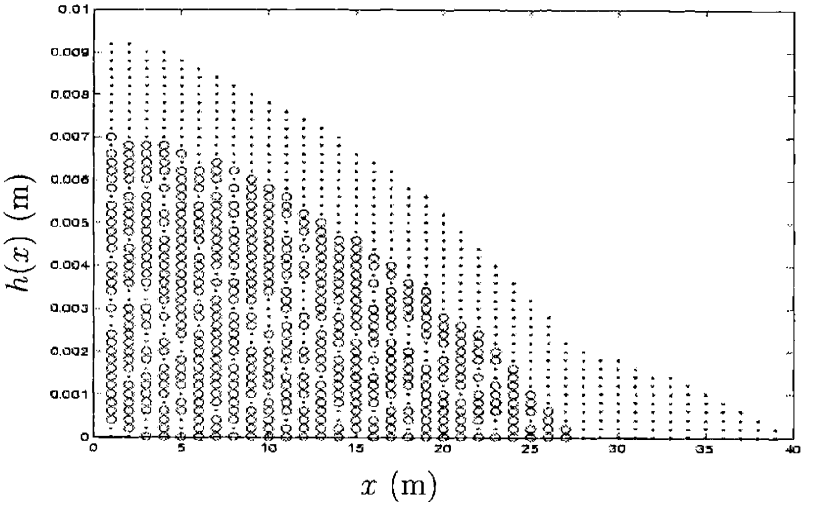

Figure 3-5: Dependence of the deposit height, $h(x)$, on distance from the source, x, of a bidisperse laminar fixed volume (V =10m^2) particle–laden gravity current. Initial conditions are: $\phi_I^0 = \phi_{II}^0 = 0.5\%$, $\rho_p/2 = \rho_c = \rho_f = 1$g/cc and $a_I = 2a_{II} = 20\mu$m. Circles correspond to high particle fractions of large particles (I) and points to high particle fraction of small particles (II).

$a_I = 2a_{II} = 20\mu$m. The region where the flow is laminar grows in time and exhibits a more pronounced particle separation than in simulations where the flow was assumed to be everywhere turbulent.

3.4 Conclusion

We have developed a theoretical model to describe the dynamics of particle–laden gravity currents and particular attention was given to the deposits left by such currents. We have extended the results of Hogg, Ungarish & Huppert (2000), describing the runout length of turbulent currents, to laminar particle–laden gravity currents, which were seen to be considerably shorter than turbulent ones. The box–model we used in our simulations allows for rapid computation of the shape of deposits as well as the distribution of particles within them. Our model may also readily be extended to incorporate the effects of more than two types of particles and thus provide a computationally efficient way to estimate deposits resulting from polydisperse particle–laden gravity currents.

Our model may thus be used to predict the shape of deposits resulting from particle clouds that reach the bottom of the container while still in their self–similar phase. The initial radius of the current is given by the lateral extent of the cloud, while the initial density of the fluid and concentration of particles may be obtained by the model presented in chapter 2. We thus have means to compute the complete time evolution of particle clouds, including the dynamics of the gravity currents they generate.

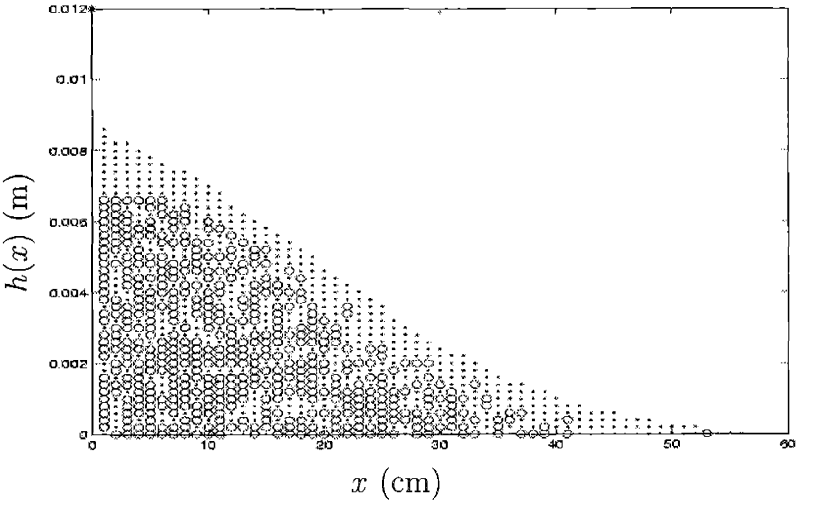

Figure 3-6: The dependence of the deposit height, $h(x)$, on the distance, x, from the point of release of a fixed volume (10m^2) bidisperse particle–laden gravity current. Here the region near the source is laminar while the head is turbulent. The transition from turbulent to laminar is assumed to occur when the Reynolds number exceeds a critical value $Re = uh/\nu > Re_c = 1000$. Circles correspond to high particle fractions of large particles (I) and points to high particle fraction of small particles (II). The region near the wall shows a more pronounced particle separation than in the case of a fully turbulent gravity current.

Modifications could be made to our model to allow for details of the flow which were neglected here. We have assumed that the flow is either turbulent or laminar, but in reality the level of turbulence varies smoothly. Moodie (2000) argued that the turbulent mixing imposed before the release of the current decays exponentially in time and therefore suggested to use a particle settling speed of the form $U_s = U_s(1 - e^{t\nu/\delta^2})$, where δ is a typical turbulent eddy size. This modification could readily be incorporated into our model. However, turbulence is also generated at the head of the current and it appears that a more precise model of the level of turbulence is needed in order to adequately describe the transition from turbulent to laminar flow, and this shall be the subject of future consideration.

Another potentially important phenomenon which has not been taken into account here is the possibility of reentrainment of particles, that is the entrainment in suspension of sediments deposited on the bottom. We have considered weakly turbulent gravity currents, where reentrainment is negligible. However, the early stages of turbidites are often sufficiently turbulent that reentraiment plays an important role (Parker *et al.* 1987). Different models have been suggested to describe reentrainment and a review may be found in Garcia & Parker (1991). However, a complete understanding of reentrainment has not been achieved yet and one must rely on empirical results to incorporate its effect on gravity currents. We thus do not pursue the influence of reentrainment in particle–laden gravity currents here, but this shall also be the subject of future investigation.

The bottom friction was also neglected in our simulations. This is usually modeled by introducing a friction term in the momentum equation (Garcia 1994) of the form $C_D u^2$, where C_D is a constant determined experimentally. Garcia (1994) suggested a value of C_D between 0.002 and 0.05, following the experimental measurements of Parker *et al.* (1987). Adding a bottom friction term gives a more realistic picture of the evolution of a gravity current, but provides little insight as to how to quantify this energy loss. Garcia (1994) and Moodie (2000) also allowed for the fact that the distribution of particles is not vertically homogeneous. Using experimental observations, Garcia (1994) determined that the bottom concentration $\phi(y = 0)$ may be written as a fraction of the vertically averaged concentration ϕ_{ave}. In his model, $\xi = \phi(y = 0)/\phi_{ave}$ take values between 1 and 3 and depends only on particle size. However, it is likely that ξ also depends on the level of turbulence within the current. Owing to the irregular nature of the turbulence within the gravity currents, it has proven difficult to estimate the value of ξ from first principles. Empirical corrections accounting for the reentrainment of particles from the bed, bottom friction and vertical non-uniformities in ϕ may readily be included in our model. However, none of them is expected to alter qualitatively the shape and particle distribution of the deposits observed.

Chapter 4

Particle–driven double–diffusive instabilities

4.1 Introduction

One of the most common instabilities generated by density variations in fluids is the Rayleigh–Bénard instability. When a planar fluid layer is heated from below, overturning may occur, the system thus reducing its potential energy (Bénard 1901). Instability occurs when the Rayleigh number, Ra, exceeds a critical value

$$Ra = \frac{g\Delta\rho h^3}{\kappa_T \nu} > Ra_c \tag{4.1}$$

where g is the gravitational acceleration, $\Delta\rho$ the density difference between the bottom and top of the container, h the height of the container, ν the kinematic viscosity and κ_T the density's diffusivity (Rayleigh 1916). The critical Rayleigh number, Ra_c, depends on boundary conditions (657 for stress–free, constant density boundaries, 1708 for no–slip, constant density boundaries, 868 for stress–free, constant density flux boundaries, 2272 for no–slip, constant density flux boundary (Chandrasekar 1963)). However, the order of magnitude of the critical Rayleigh number is always approximately 1000.

If two diffusing components affecting the density are present in a fluid, different types of instabilities may be observed. In contrast with the Rayleigh-Bénard instability, convective motions may be generated even though the total density gradient is stable, $d\rho/dz < 0$, with z the vertical coordinate. For example, if hot and salty fluid overlies cold and fresh fluid, salt–fingers may form. In the opposite scenario, where cold and fresh fluid overlies hot and salty fluid, overstable oscillations may develop, as described in chapter 1. The equations governing the motion of a fluid with two stratifying agents of different diffusivities have been analysed extensively. Veronis (1965, 1968) investigated the linear stability of combined thermal and salinity gradients, as well as the growth of finite amplitude instabilities. A detailed linear stability analysis was presented soon after by Baines & Gill (1969), where the nature of the instabilities and resulting flow structure was investigated. The complication of sloping boundaries

was considered later by Linden & Weber (1977), and studied numerically by Paliwal & Chen (1979). Applications to oceanography are extensively documented and were reviewed by Schmitt (1994).

Sedimenting particles may also play the role of a destabilising agent. A region of high particle concentration overlying a particle–depleted region may result in the formation of particle plumes (Drake 1971, Chen 1997). Details of the instability of a region of high sand concentration settling above a clear fluid region in a Hele-Shaw cell were recently investigated by Völtz, Pesch & Rehberg (2001), and many similarities with Rayleigh-Taylor instabilities (where a layer of heavy fluid overlies lighter fluid) were observed. A similar instability may result from particles settling through a density jump; as particles settle across a density interface, they form a region of high concentration overlying a particle–depleted region, which then becomes unstable (Hoyal *et al.* 1999). Particles settling in a density gradient may also play the role of the slowly diffusing agent in a double–diffusive system (Houk & Green 1973). Particle–fingers, the analog of salt–fingers, have been observed experimentally when particles settle across a density interface in a quiescent fluid (Green 1987) and at the base of a spreading gravity current by Maxworthy (1999) and Parsons, Bush & Syvitski (2001). A stability analysis of the progression of a horizontal layer of particle–laden fluid overlying particle–free fluid was presented by Mason (1988), in the limit of non-diffusing particles.

A linear stability analysis of a particle concentration gradient of particles settling in an ambient density gradient has yet to be undertaken. It is of particular interest to determine when particles may effectively be treated as a solute and when their non–zero settling speed must be taken into account. In this chapter, we focus on particle–driven double–diffusive instabilities. We consider a monodisperse suspension and assume a constant settling speed, U_s. We restrict our attention to small Reynolds number particles, $Re_p = U_s a/\nu < 1$, so that inertial effect may be neglected when describing the evolution of the particle concentration. We perform a linear perturbation analysis of the system of equations considered by Baines & Gill (1969) for the analogous thermohaline system, with the addition of a particle concentration advection term. The non–zero settling speed of particles may be treated through the introduction of a particle Péclet number, Pe, which represents the ratio of a particle advection time scale to an ambient density diffusive time scale $Pe = (U_s/h)/(h^2/\kappa_T) = U_s h/\kappa_T$. In geophysical contexts, Pe may range from 0 for very small particles and macromolecules, to $O(1000)$ for particles of approximate size 1mm settling in a salinity gradient.

Other important non–dimensional quantities in our system are the Prandtl number, $\sigma = \nu/\kappa_T$, whose values typically range from $O(1)$ to $O(1000)$ depending on the stratifying agent, and the diffusivity ratio, $\tau = \kappa_\phi/\kappa_T$ with κ_ϕ the particle diffusivity. For very small particles, of the order of 10nm, Brownian motion determines the magnitude of the particle diffusion coefficient. However for larger particles, settling speed fluctuations due to the presence of neighbouring particles, the so–called hydrodynamic dispersion effects, dominate the effects of Brownian motion (Caflisch & Luke 1985, Ham & Homsy 1988). The magnitude of κ_ϕ therefore depends on the particle settling speed, radius and concentration (Mucha *et al.* 2003, Martin, Rakotomalala

& Salin 1995). Moreover, particle diffusion is typically anisotropic, diffusion parallel to the settling direction being typically greater than that perpendicular to the settling direction, $\kappa_{hor} = \Phi\kappa_{ver}$, $\Phi < 1$. While numerical simulations show a relatively large anisotropy, ranging from $\Phi = O(1/50)$ (Koch 1994) to $\Phi = O(1/10)$ (Mucha *et al.* 2003, Kuusela & Ala-Nissila 2001), the experimental results of Nicolai *et al.* (1995) suggest that $\Phi \sim 1/5$. Numerical studies also exhibit a dependence of κ_ϕ on the container size, but experimental measurements have not confirmed such a dependence. Dimensional analysis suggests that the vertical diffusion constant of particles larger than 10nm be expressed as $\kappa_\phi = naU_s$, where n is a coefficient whose numerical value was measured to be between 4 and 20, (Martin *et al.* 1994, 1995, and Davis & Hassen 1988). The particle concentration affects the value of n, but variations are typically smooth and sufficiently weak that, for our purposes, we may consider n to be constant. Note that the diffusion constant of particles may be relatively large: experimental measurements of κ_ϕ range from $\kappa_\phi \sim 10^{-6}\mathrm{m}^2/\mathrm{s}$ (Ham & Homsy 1988) to $\kappa_\phi \sim 10^{-9}\mathrm{m}^2/\mathrm{s}$ (Martin *et al.* 1995). Depending on the ambient stratifying agent and on particle the particle size, the diffusivity ratio may thus takes values ranging from $\tau = 10^{-3}$ for small particles settling in a temperature gradient, to $\tau = 10^3$ for large particles settling in a salinity gradient.

We study numerically the stability of double–diffusive systems where one of the stratifying component settles with velocity U_s. We first review thermohaline double–diffusive instabilities in §4.2. We then present the governing equations including the effect of particle settling and discuss the method used to analyse their stability in §4.3. Numerical simulations allow us to determine the stability of various configurations. We present in §4.4 results describing the stability of an unstable particle concentration gradient settling in a fluid of uniform density and also that of equal and opposite ambient density and particle concentration gradients. We discuss the implications of our numerical results in §4.5.

4.2 Thermohaline double–diffusion

We begin by reviewing results obtained when two diffusing components affecting density are present in a fluid. We consider a system where the density depends on a relatively rapidly diffusing component (T), such as heat, and a slowly diffusing component (S), such as salt. In a two-dimensional system, x in the horizontal and z in the vertical, the governing equations are (Baines & Gill 1969)

$$\rho_0(u_t + uu_x + wu_z) = -p_x + \rho_0\nu(u_{xx} + u_{zz}) \tag{4.2}$$

$$\rho_0(w_t + uw_x + ww_z) = -p_z + \rho_0\nu(w_{xx} + w_{zz}) - \rho_0 g\alpha T + \rho_0 g\beta S \tag{4.3}$$

$$T_t + uT_x + wT_z = \kappa_T(T_{xx} + T_{zz}) \tag{4.4}$$

$$S_t + uS_x + wS_z = \kappa_S\,(S_{xx} + S_{zz}) \tag{4.5}$$

where u, w, ρ_0 and p stand for the horizontal velocity, vertical velocity, typical density and hydrodynamic pressure of the fluid respectively, and where we made use of the Boussinesq approximation.

Four non–dimensional parameters are required to fully describe the stability of a given initial configuration. A Rayleigh number is needed for each component

$$R_T = \frac{g\alpha\Delta T h^3}{\kappa_T \nu}, \qquad R_S = \frac{g\beta\Delta S h^3}{\kappa_T \nu}, \tag{4.6}$$

where h is a typical height, α and β are the expansion coefficients associated with heat and salt, and ΔT, ΔS are the temperature and salinity difference from bottom to top

$$\Delta T = T_{bottom} - T_{top}, \qquad \Delta S = S_{bottom} - S_{top}. \tag{4.7}$$

A positive value of R_T thus corresponds to a destabilising temperature gradient, while a positive value of R_S corresponds to a stabilising salinity gradient. Note that for simplicity of notation, R_S contains κ_T rather than κ_S. The Prandtl number $\sigma = \nu/\kappa_T$ and, more importantly, the ratio of the diffusivity coefficients $\tau = \kappa_S/\kappa_T$ are also determinant in the stability of the system. Baines & Gill (1969), considered infinitesimal perturbations of amplitude e^{pt} and showed that a linear stability analysis of equations (4.2-4.5) yields a criterion for salt fingering:

$$\frac{R_S}{\tau} < \left(R_T - \frac{27\pi^4}{4}\right) \tag{4.8}$$

where the real part of p is positive and the imaginary part is 0 so that the mode of instability is direct. Because S was chosen to be the slowly diffusing component, $\tau < 1$ and instability may occur even though the total density profile is uniform (corresponding to $R_T = R_S$). Overstable oscillations may occur if the real part of p is positive and its imaginary part is non–zero, as is the case if

$$R_T > \left(\frac{\sigma+\tau}{\sigma+1}\right) R_S + (1+\tau)\left(1+\frac{\tau}{\sigma}\right)\frac{27\pi^4}{4}. \tag{4.9}$$

Note that here again, instability may occur if the total density is uniform.

4.3 Settling particles as a stratifying agent

We perform the analogous linear stability analysis fro a system in which one of the stratifying agents is settling particles (ϕ) and the other is a purely diffusing component (T) such as heat or a solute. We consider a layer of depth h, and initially linear ambient density and particle concentration gradients. The boundaries consist of two infinite horizontal solid plates where we apply a no–slip boundary condition and assume the ambient density and particle concentration to be maintained constant, corresponding to a steady supply of particles at the top boundary. The density of the fluid is given by

$$\rho^* = \rho_0(1 - \alpha T^* + \frac{\rho_p - \rho_0}{\rho_0}\phi^*) \tag{4.10}$$

where α is the expansion coefficient associated with T^*, ρ_p and ρ_0 are the particle density and reference density of the fluid in the absence of particles and at $T^* = 0$, respectively, and all $*$ quantities are dimensional. We consider a two–dimensional system, x in the horizontal and z in the vertical, with $z = 0$ at the bottom and $z = h$ at the top of the container. Taking into account the non-zero settling speed of particles, U_s, the governing equations of motion are

$$\rho_0(u_t^* + u^* u_x^* + w^* u_z^*) = -p_x^* + \rho_0 \nu^* (u_{xx}^* + u_{zz}^*) \tag{4.11}$$

$$\rho_0(w_t^* + u^* w_x^* + w^* w_z^*) = -p_z^* + \rho_0 \nu (w_{xx}^* + w_{zz}^*) - \rho_0 g \alpha T^* + g(\rho_p - \rho_0)\phi^* \tag{4.12}$$

$$T_t^* + u^* T_x^* + w^* T_z^* = \kappa_T \, (T_{xx}^* + T_{zz}^*) \tag{4.13}$$

$$\phi_t^* + u^* \phi_x^* + w^* \phi_z^* - U_s \phi_z^* = \kappa_\phi \, (\Phi \phi_{xx}^* + \phi_{zz}^*). \tag{4.14}$$

where u^*, w^* and p^* stand for the horizontal velocity, vertical velocity and hydrodynamic pressure of the suspension respectively. Following the experimental measurements of Nicolai *et al.* (1995), we set $\Phi = 1/5$ in our simulations. However, we note that the anisotropy constant was seen to have little influence on the stability diagrams discussed here for physically reasonable values of Φ ranging from 1 to 1/50.

We non-dimensionalize equations (4.11-4.14) using h^2/κ_T as a typical timescale, h as a lengthscale, ρ_0 as a density, $\Delta\phi$ for particle concentration variations and ΔT as a typical ambient density variation. We eliminate the pressure term by taking ∂_x(4.12) - ∂_z(4.11) and introduce a streamfunction ψ^* such that the horizontal and vertical velocities are given by $(u^*, v^*) = (-\psi_z^*, \psi_x^*)$. We consider perturbations from a quiescent background in which the ambient density profile is linear and the particle concentration profile is a linear gradient propagating downward with speed U_s (Pe in non–dimensional form)

$$\psi' = 0 + \psi \qquad T' = -z + T \qquad \phi' = -z - tPe + \phi, \tag{4.15}$$

where the primed quantities are non–dimensional and the unprimed quantities are the non–dimensional perturbations. This allows us to neglect non–linear terms and we are left with

$$\frac{1}{\sigma}(\partial_t - \nabla^2)\nabla^2 \psi = -R_T T_x + R_S \phi_x \tag{4.16}$$

$$(\partial_t - \nabla^2) T = \psi_x \tag{4.17}$$

$$(\partial_t - \tau(\Phi \partial_{xx} + \partial_{zz})\phi = \psi_x + Pe\phi_z. \tag{4.18}$$

with boundary conditions

$$\psi = \psi_z = T = \phi = 0 \qquad \text{at } z = \pm 1/2. \tag{4.19}$$

where $\Delta\phi(\rho_p - \rho_0)$ and κ_ϕ replace $\beta\Delta S$ and κ_S respectively in the definition of R_S.

To investigate the stability of this system of equation, we use the method of normal modes and assume perturbations of the form

$$\psi = \psi^o(z) e^{pt+ikx}, \quad T = T^o(z) e^{pt+ikx}, \quad \phi = \phi^o(z) e^{pt+ikx}. \tag{4.20}$$

The system of equation (4.16)-(4.18) then reduces to a system of ordinary differential equation in z,

$$\frac{p}{\sigma}(\psi^o_{zz} - k^2\psi^o) - (\psi^o_{zzzz} - 2k^2\psi^o_{zz} + k^4\psi^o) + R_T ikT^o - R_S ik\phi^o = 0 \quad (4.21)$$

$$pT^o + k^2T^o - T^o_{zz} - ik\psi^o = 0 \quad (4.22)$$

$$p\phi^o + \tau\Phi k^2\phi^o - \tau\phi^o_{zz} - Pe\phi^o_z - ik\psi^o = 0 \quad (4.23)$$

and the boundary conditions (4.19) are now applied to functions indexed with an o. This system of equation does not have a simple and elegant solution as does the purely double–diffusive case. We thus resort to numerical methods to investigate its stability.

Using the methods described by Finlayson (1972), and following Paliwal & Chen (1979), we expand the perturbations in a series of functions of a known form

$$\psi^o(z) = \sum_{n=1}^{\infty} a_n\psi^n(z), \quad \phi^o(z) = \sum_{n=1}^{\infty} b_n\phi^n(z), \quad T^o(z) = \sum_{n=1}^{\infty} c_nT^n(z) \quad (4.24)$$

where the functions $\psi^n(z)$, $\phi^n(z)$ and $T^n(z)$ are chosen to satisfy the homogeneous boundary conditions (4.19), to obey $\partial_{zzzz}\psi = \lambda\psi$ and to form a complete orthogonal set

$$\psi^n = \begin{cases} \frac{\cosh(\rho_n z)}{\cosh(\frac{1}{2}\rho_n)} - \frac{\cos(\rho_n z)}{\cos(\frac{1}{2}\rho_n)} & \text{if } n \text{ is odd,} \\ \frac{\sinh(\mu_n z)}{\sin(\frac{1}{2}\mu_n)} - \frac{\sin(\mu_n z)}{\sin(\frac{1}{2}\mu_n)} & \text{if } n \text{ is even.} \end{cases} \quad (4.25)$$

$$T^n = \phi^n = \begin{cases} \sin((n+1)\pi z) & \text{if } n \text{ is odd,} \\ \cos((n-1)\pi z) & \text{if } n \text{ is even,} \end{cases} \quad (4.26)$$

where

$$\tanh(\rho_n/2) + \tan(\rho_n/2) = 0, \qquad \coth(\mu_n/2) - \cot(\mu_n/2) = 0. \quad (4.27)$$

We then proceed to use the Galerkin method by considering the projection of equations (4.21), (4.22) and (4.23) onto the basis functions ψ^n, T^n and ϕ^n respectively. Each equation is integrated over $-1/2 \leq z \leq 1/2$ to yield an algebraic system of equations in terms of the coefficients a_n, b_n and c_n. To solve for those coefficients, we truncate the infinite system, keeping only the first N terms. We thus obtain a system of equations of the form $(A - pB)\vec{x} = 0$, where $\vec{x}$ is a vector containing the coefficients a_n, b_n and c_n. To find a non–trivial solution, we look for eigenvalues of this system and the stability of the flow is determined by the real part of p.

4.4 Numerical results

We first validated our method by reproducing results for one component convection and double–diffusive instabilities. Due to imprecisions occurring when looking for

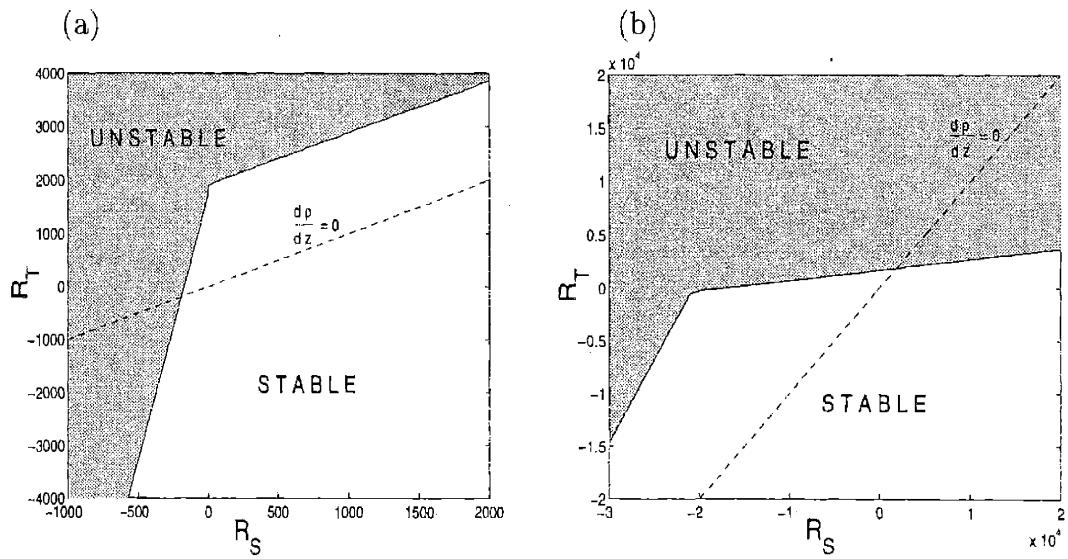

Figure 4-1: Critical temperature Rayleigh number R_T as a function of the particle Rayleigh number R_S for non–settling particles, $U_s = 0$. a) small diffusivity ratio $\tau = \kappa_\phi/\kappa_T = 0.1$ (b) large diffusivity ratio $\tau = 10$. The region above the solid line is linearly unstable, while the region below is stable. The dashed line corresponds to a uniform density $R_S = R_T$; the overlying region $R_T > R_S$ has a statically unstable density profile. In (a), the solid line crosses the dashed line at $R_S = R_T = 31550$ and -189 and in (b) at $R_S = R_T = 1850$ and -57000 showing that instabilities may occur even though the density gradient is statically stable. The value of the Prandtl number is kept constant at 7, a value appropriate for aqueous systems stratified through a temperature gradient.

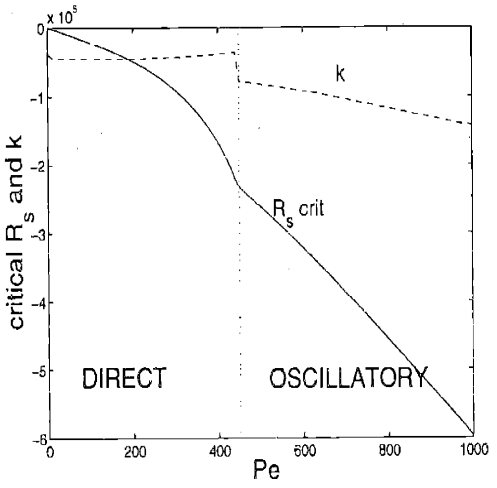

Figure 4-2: The dependence of critical particle Rayleigh number, R_S, and most unstable wavenumber, k, on the Péclet number, $Pe = U_s h/\kappa_\phi$, in the absence of an ambient density gradient, $R_T = 0$. The solid line indicates the critical value of R_S and the dashed line represents k (multiplied by -10^4 for scaling purposes). The dotted line separates regions of direct (left) and oscillatory (right) instabilities. The value of the Prandtl number is kept constant at 7, a value appropriate for 20μm glass particles settling in water.

eigenvalues of the system $(A - pB)x = 0$, a small error ($< 3\%$) on the critical values of the Rayleigh numbers is expected from computations on systems with known critical Rayleigh numbers. In the case $R_S = 0$, corresponding to Rayleigh-Bénard convection, we observe a critical Rayleigh number near $R_T = 1740$, and the most unstable wavenumber is $k = 3.12$, in good agreement with previous results (Chandrasekar 1961). In the case $Pe = 0$, corresponding to classic double–diffusive instabilities, a stability diagram is obtained by varying R_T and looking for the critical R_S, see figure 4-1. The agreement with the results of Baines & Gill (1969) is excellent. Note that the quantitative values are different due to the use of the no–slip condition in our simulations (compared to a stress–free condition in Baines & Gill (1969)). However, the slope of the critical Rayleigh number, dR_T/dR_S, in the fingering regime ($R_T < 0$), obeys approximately $1/\tau$ and is independent of σ, in agreement with the computations of Baines & Gill (1969). In the overstable regime ($R_T > 0$), dR_T/dR_S approaches 1 for large values of σ and depends only weakly on τ. We also verified that the results of our simulations were independent of N, as should be the case if N is sufficiently large. Comparing results obtained with $N = 48$ and $N = 50$ showed a difference of less than 0.3%; we therefore used $N = 48$ in the simulations discussed below. These results allow us to confidently explore cases where $Pe \neq 0$.

4.4.1 Particle settling in a uniform ambient

We first consider the case of a destabilising particle concentration gradient, $R_S < 0$, settling in a homogeneous ambient, $R_T = 0$, so that the initial density gradient is statically unstable $d\rho/dz > 0$. Physically, this corresponds to the settling in a homogeneous ambient of a suspension with particle concentration increasing with height. The non–zero settling speed of particles acts to stabilise the system and we expect the critical Rayleigh number to increase with Péclet number. The Rayleigh number may be viewed as the ratio of the falling time of a blob of particle–laden fluid of size h to the time required for the blob to lose its excess particles through diffusion:

$$\frac{-R_S}{\tau} = -\frac{(gh^2\frac{\rho_p-\rho_0}{\rho_0}\Delta\phi)/\nu}{\kappa_\phi/h}. \tag{4.28}$$

Note that here R_S/τ (and later Pe/τ) simply corresponds to the Rayleigh (and Péclet) number defined in terms of the diffusion constant of particles, κ_ϕ. If the absolute value of this ratio exceeds a critical value, convection ensues. To include the effects of particle settling, we instead consider the fall speed of a perturbation of size h relative to the settling particles

$$\frac{-(gh^2\frac{\rho_p-\rho_0}{\rho_0}\Delta\phi)/\nu - U_s}{\kappa_\phi/h} = \frac{-R_S - Pe}{\tau}. \tag{4.29}$$

We thus expect the critical Rayleigh number to grow linearly with increasing Péclet number.

Simulations performed with $R_T = 0$ and $\sigma = 7$ confirm this reasoning over the range $0 < Pe < 300$ and $450 < Pe < 1500$ (see figure 4-2). Here the solid line is the critical value of R_S and the dashed line indicates the most unstable wavenumber. The mode of instability is direct left of the dotted line and oscillatory right of the dotted line. The slope of the critical R_S as a function of Pe, dR_s/dPe, is seen to be approximately -220 for values of $Pe < 300$ and -690 for $Pe > 450$, with a smooth transition in the intermediate region.

A remarkable feature of figure 4-2 is that the imaginary part of the most unstable mode becomes non–zero for $Pe > 450$. The mode of instability of particles with sufficiently large Péclet numbers is thus oscillatory and the frequency of oscillations is of order $1000\kappa_T/h^2$ and increases with Pe. This contrasts with the Rayleigh–Bénard instability which remains direct even for large Rayleigh numbers. The mechanism of instability is thus modified by the non–zero settling speed of the particles. In our system, the most unstable wavenumber remains near 4 for small values of Pe, but jumps to 7.8 at $Pe = 450$ and thereafter increases with Péclet number, indicating that the non–zero settling speed of particles is determinant in the nature of the instability.

It should be mentioned that for small Pe, as in classic Rayleigh-Bénard convection, the Prandtl number, $\sigma = \nu/\kappa_T$, does not influence the stability of the system. From equation (4.21), we see that if the imaginary part of p is 0, the Prandtl number does not influence the value of the critical Rayleigh number (where the real part of

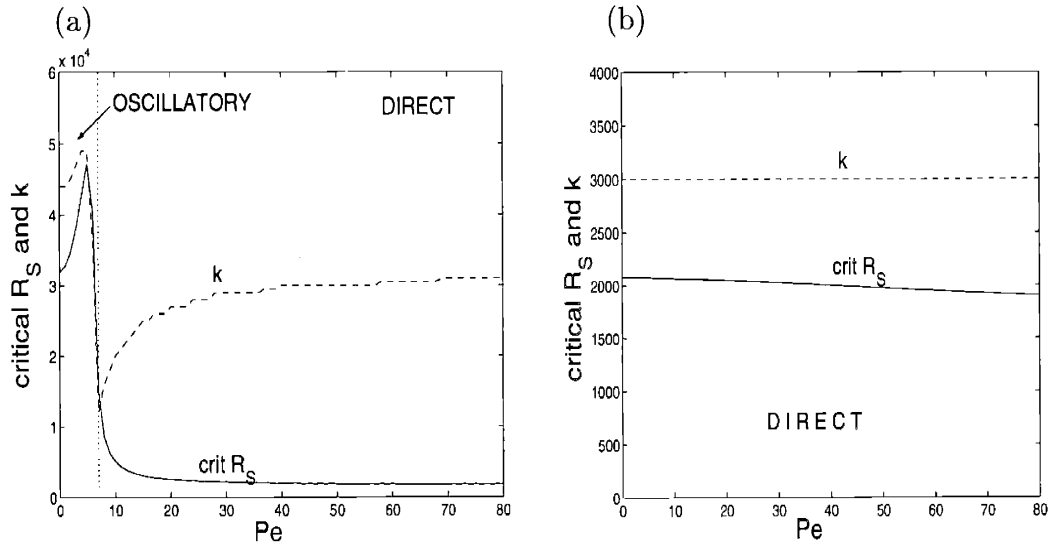

Figure 4-3: Dependence of the critical particle Rayleigh number, R_S, and most unstable wavenumber, k on the Péclet number, $Pe = U_s h/\kappa_T$. The initial density is uniform; an unstable ambient density gradient is opposed by a stable particle concentration gradient ($R_T = R_S > 0$). Figure (a) shows computations conducted with a small diffusivity ratio $\tau = \kappa_\phi/\kappa_T = 0.1$ and (b) with a large diffusivity ratio, $\tau = 10$. The solid lines ibndicate the critical value of $R_T = R_S$ and the dashed line the most unstable wavenumber k (multiplied by 10^4 in (a) and by 10^3 in (b)). The dotted line in (a) separates regions of oscillatory (left) and direct (right) instabilities. Instabilities for $\tau = 10$ (figure (b)) are always direct. The value of the Prandtl number is kept constant at 7, a value appropriate for water stratified through temperature variations.

p is also 0 and hence σ becomes irrelevant). Therefore, only oscillatory solutions are influenced by σ. The values discussed above were found for $\sigma = 7$, a value corresponding to 20μm glass particles settling in water (the particle diffusion constant is then $\kappa_\phi \approx 1.5 \times 10^{-7}\mathrm{m}^2/\mathrm{s}$). For higher values of σ, appropriate for smaller particles, the transition to the oscillatory mode of instability occurs at smaller Péclet number, $Pe = 310$ for $\sigma = 70$ and $Pe = 270$ for $\sigma = 700$. The slope of the critical Rayleigh number as a function of Pe is also reduced for larger values of σ, to -50 for $\sigma = 70$ and -5 for $\sigma = 700$. The critical Rayleigh number thus appears to increase linearly with the Reynolds number of the system, $Re = Pe/\sigma = U_s h/\nu$, with a proportionality constant of the order of 3500. For $Pe > 450$, instability therefore occurs if

$$\frac{R_S}{\tau} + 3500Re < -10^3. \tag{4.30}$$

4.4.2 Stabilising ϕ, destabilising T

We proceed by considering the case of an unstable ambient density gradient, $R_T > 0$, in the presence of a stable particle concentration gradient, $R_S > 0$. For example, this corresponds to a system where cold and clear fluid overlies hot and particle–laden fluid. A similar system, albeit with discontinuous particle concentration and ambient density, was studied experimentally by Huppert *et al.* (1991) and the layer of light fluid formed above the settling suspension was seen to be unstable. The finite settling speed of particles is expected to have a destabilising effect. In the limit of a large settling speed, the particle concentration gradient quickly moves downward and leaves behind an unstable density gradient. Instabilities are then analogous to the Rayleigh–Taylor instability with only one stratifying agent.

We investigate this scenario numerically by restricting ourselves to cases where the total density is initially uniform, $d\rho/dz = 0$, and we thus set $R_S = R_T$. To focus on the effects of particle settling, we fix $\sigma = 7$, a value appropriate for water with temperature acting as a stratifying agent. We consider first the case where particles diffuse slowly relative to the ambient density, $\tau = 0.1$. If $Pe = 0$, this corresponds to the overstable regime of the double–diffusive instability and we find a critical value of $R_S = 31900$ above which the system becomes unstable to oscillations of growing amplitude. In our simulations, the imaginary part of the most unstable mode is non–zero, indicating that the instability takes the form of oscillations of growing amplitude, in agreement with the results of Baines & Gill (1969).

Figure 4-3a illustrates the dependence of the critical Rayleigh numbers on the Péclet number when the particles act as the slowly diffusing agent ($\tau = 0.1$). The solid line represents the critical value of $R_T = R_S$ for a given Péclet number and the dashed line is the most unstable wavenumber (multiplied by 10^4 for scaling purposes). The dotted line again separates regions of oscillatory (left) and direct (right) instability. As the Péclet number increases, the critical Rayleigh number first increases until $Pe = 5$ (where $R_S = 47100$), then decreases until $Pe = 7$. The nature of the instability then changes abruptly. From an overstable mode, the instability becomes direct, the imaginary part of the most unstable mode becoming 0. The most unstable wavenumber, k, also drops discontinuously from 3.6 to 1.2. Most significantly, the critical Rayleigh number drops sharply by an order of magnitude from 40450 to 15100. As the Péclet number is increased further, the critical Rayleigh number decreases further until it stabilises to a value near 1800 for $Pe > 40$. This indicates that the presence of a stabilising particle concentration gradient has virtually no influence on the stability of an ambient density gradient if the Péclet number of the particles is larger than 40. The most unstable wavenumber and the imaginary part of the most unstable mode also remain constant, taking values of approximately 3.1 and 0 respectively, as would be the case in the absence of particles.

Figure 4-3b illustrates the dependence of the critical Rayleigh number (solid line) and most unstable wavenumber (dashed line), k, on the Péclet number when particles diffuse faster than the ambient density ($\tau = 10$). For small Péclet numbers, $Pe < 7$, this corresponds to the "salt–finger" regime, with particles now playing the role of heat. We again consider a uniform ambient density, $R_S = R_T > 0$. The observed

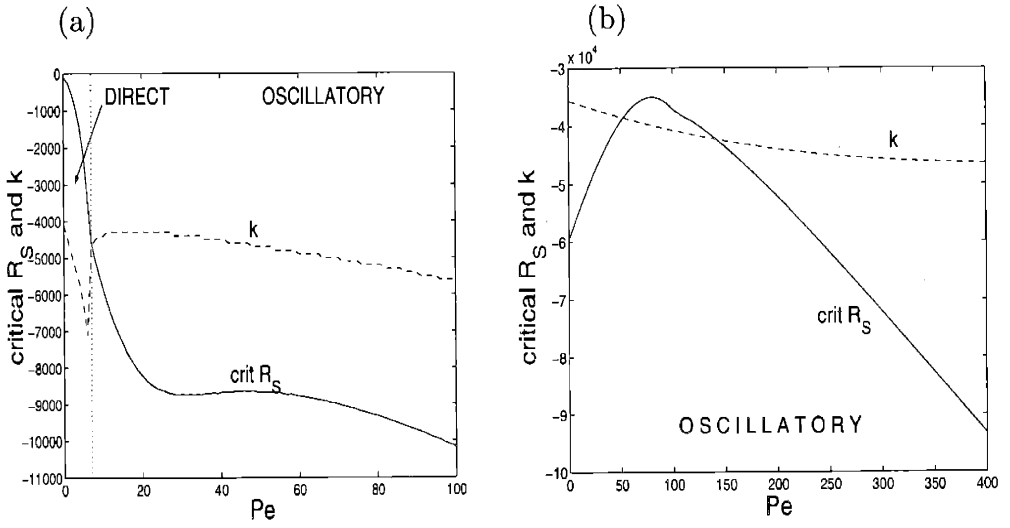

Figure 4-4: The dependence of the critical particle Rayleigh number, R_S, and most unstable wavenumber, k, on the Péclet number, $Pe = U_s h/\kappa_T$, in an ambient of uniform density, with a stabilising ambient density gradient and a destabilising particle concentration gradient ($R_T = R_S < 0$). Figure (a) shows computations done with a small diffusivity ratio $\tau = \kappa_\phi/\kappa_T = 0.1$ and figure (b) with a large diffusivity ratio, $\tau = 10$. The solid line is the critical value of $R_T = R_S$ and the dashed line indicates k (multiplied by -10^3 in (a) and -10^4 in (b)). The dotted line in (a) separates regions of direct (left) and oscillatory (right) instabilities. Instabilities in (b) are always oscillatory. The value of the Prandtl number is kept constant at 7, a value appropriate for water stratified through temperature variations.

qualitative dependence of R_S on Pe is similar to that observed for the case $\tau = 0.1$. The mode of instability is direct and the critical Rayleigh numbers are relatively low, $R_S = R_T = 2070$. As the Péclet number is increased, the critical Rayleigh number again decreases, albeit slowly, reaching $R_T = 1880$ for $Pe = 100$. The mode of instability is seen to remain direct for $0 < Pe < 100$, and the most unstable wavenumber is remarkably constant over this range, at $k = 3$. The stability of a system marked by a destabilising ambient density gradient opposed by a stabilising particle concentration gradient is thus seen to be determined almost exclusively by the ambient density gradient for $Pe > 40$.

4.4.3 Destabilising ϕ, stabilising T

We now turn to the opposite case, where the ambient fluid is stably stratified and the particle concentration is destabilising. Systems of fresh, particle–laden fluid overlying salty, particle–free fluid were investigated in the context of rivers intruding in the ocean (Houk & Green 1973, Green 1987, Hoyal *et al.* 1999, Parsons *et al.* 2001). However, all these authors considered discontinuous initial conditions, making the comparison with our simulations difficult. Particle–fingers have been observed

for particles of order 1μm (Green 1987) and instabilities caused by the formation of a three layered system were seen for larger particles (Hoyal *et al.* 1999). For infinitesimal perturbations to grow in time, particle–fingers should descend faster than individual particles. As was the case for particle concentration gradients settling in a homogeneous ambient, we expect large Péclet numbers to stabilise the system and impede the formation of particle–fingers. Here, we again set $R_T = R_S < 0$ so that the initial density is uniform and fix $\sigma = 7$. Figure 4-4a shows the dependence of the critical Rayleigh number (solid line) and most unstable wavenumber k (multiplied by -10^3, dashed line) for the case $\tau = 0.1$. The critical Rayleigh number decreases sharply with Péclet number for small Pe, from $R_S = -120$ down to approximately $R_S = -8500$ for $Pe = 25$. The instability mode becomes oscillatory for $Pe > 5$, implying that "fingers" will not form in this regime but that the instabilities instead take the form of waves of growing amplitudes. For values of Pe between approximately 20 and 60, the increase in critical Rayleigh number is very slow. However, the frequency of the most unstable mode increases linearly with Pe, showing that the time–scale of instability is set by the Péclet number. The most unstable wavenumber is also seen to increase, from about $k = 4$ for small Péclet numbers to $k = 5.5$ at $Pe = 100$. For $Pe > 60$, the instability remains oscillatory but R_S resumes its dependence on Pe, with $dR_S/dPe = -50$.

Figure 4-4b illustrates the influence of the Péclet number on the critical Rayleigh number when particles diffuse faster than the ambient density ($\tau = 10$), as would be the case for glass particles with radii larger than 10μm settling in a salinity gradient. The solid line indicates the critical Rayleigh number and the dashed line is the most unstable wavenumber (multiplied by -10^4 for scaling purposes). The mode of instability is oscillatory for $Pe = 0$, corresponding to the overstable regime of double–diffusive systems, with particles playing the role of heat. As the Péclet number is increased, the mode of instability is seen to remain oscillatory and the most unstable wavenumber to increase slowly from $k = 3.5$ at $Pe = 0$ to $k = 4.5$ at $Pe = 500$. The magnitude of the critical Rayleigh number initially decreases, showing that small values of Pe destabilise the system. For $Pe > 90$, increasing Pe stabilises the system and tends to impede the growth of the oscillatory instabilities as in the case $\tau < 1$. For larger Péclet numbers, the magnitude of the critical R_S increases linearly. The frequency of oscillation of the most unstable mode is also seen to increase almost linearly with Péclet number, indicating again that the time scale of the instability depends critically on the Péclet number and hence on the particle settling speed.

4.4.4 Influence of the diffusivity ratio, τ

The diffusivity ratio, τ is a determinant factor in the stability of the system. If $\tau > 1$, the particles diffuse faster than the ambient density, whereas if $\tau < 1$ particles act as the slowly diffusing component. We here focus on the influence of variations of τ by fixing $Pe = 100$ and $\sigma = 7$ and considering the critical Rayleigh number based on the ambient stratification, R_T, as a function of the particle Rayleigh number R_S.

Figure 4-5a illustrates the critical R_T as a function of R_S for different diffusivity ratios when $\tau > 1$. This corresponds physically to relatively large particles (a¿10μm)

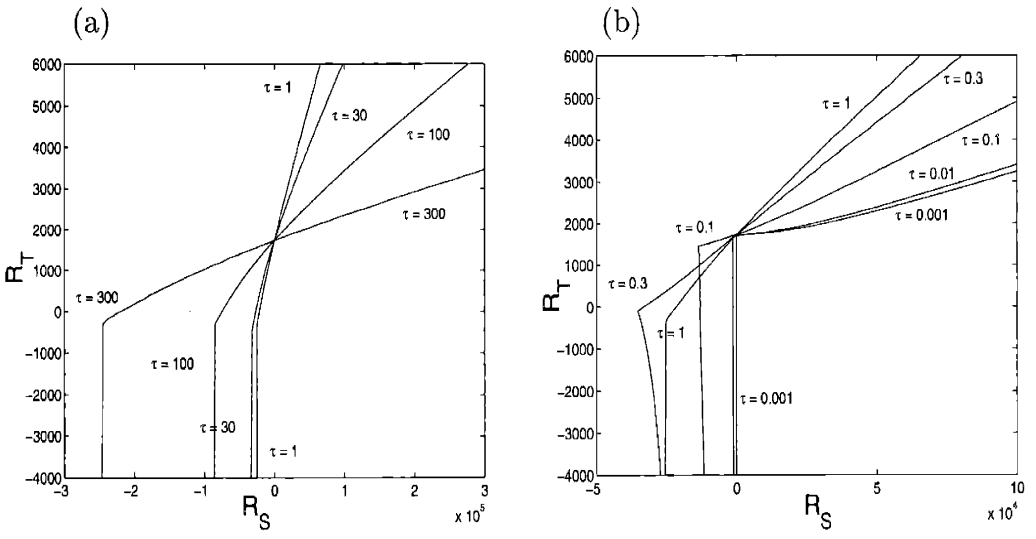

Figure 4-5: Dependence of the critical values of the ambient density Rayleigh number, R_T, on the particle Rayleigh number, R_S, for different values of the diffusivity ratio, $\tau = \kappa_\phi/\kappa_T$. The region above and to the left of a solid curve is linearly unstable and that below and to the right is stable. a) $\tau \geq 1$, particles diffuse faster than the ambient fluid's density; b), $\tau \leq 1$ particles act as the slowly diffusing component. The value of the Prandtl number is kept constant at 7, a value appropriate for water stratified through temperature variations.

settling in an ambient stratified through variations in a solute concentration such as salt. When a stable concentration gradient settles in an unstably stratified ambient (R_T, R_S¿0), a larger particle diffusion (increasing τ), and therefore a larger diffusivity difference between particles and ambient density, is destabilising. This indicates that the instability relies on the difference in diffusivities, as is the case for ordinary salt–fingers. The influence of the Péclet number is weak in this case and the dependence of the stability region on τ is similar to that of thermohaline systems. For negative R_S and R_T, corresponding to an unstable particle concentration gradient settling in a stably stratified ambient, larger particle diffusion is seen to be stabilising. The slope of R_T as a function of R_S is not readily affected by τ, but the region of instability is shifted to the left. The unstable oscillations are thus damped by the large particle diffusivity. However, even for large τ, the slope of the critical R_T as a function of R_S remains greater than one, indicating that, for sufficiently large Rayleigh numbers, instability may occur even when the total density gradient is statically stable.

The dependence of R_T on R_S for different values of $\tau < 1$ is shown in figure 4-5b. For $R_T, R_S > 0$, it may be seen that increasing particle diffusivity stabilises the system, indicating that the instability mechanism does not rely on the difference in diffusivities but rather on the release of the potential energy from ambient density field. The slope of the critical value of R_T as a function of R_S tends to a constant for very small values of τ, but decreases to 0 for increasing values of Pe, showing that the advection of particles is dominant in this regime. For negative R_S and R_T, a larger

	$\tau > 1$	$\tau < 1$
$R_S, R_T > 0$	Direct	Oscillatory $\rightarrow$ direct with $\nearrow Pe$
	Destabilised by $\nearrow Pe$	Destabilised by $\nearrow Pe$
	Destabilised by $\nearrow \tau$	Stabilised by $\nearrow \tau$
$R_S, R_T < 0$	Oscillatory	Direct $\rightarrow$ oscillatory with $\nearrow Pe$
	Destab. $\rightarrow$ stab. by $\nearrow Pe$	Stabilised by $\nearrow Pe$
	Stabilised by $\nearrow \tau$	Stabilised by $\nearrow \tau$

Table 4.1: Summary of the dependence of the qualitative mode of instability on the particle Péclet number, $Pe = U_s h/\kappa_T$, and diffusivity ratio $\tau = \kappa_\phi/\kappa_T$. The initial density profile considered is uniform in all cases.

particle diffusion is also stabilising. In this regime, a larger particle diffusion acts to dampen unstable oscillations, except for $\tau = 1$ which appears more unstable than $\tau = 0.3$. The qualitative dependence of the stability region on particle diffusivity is thus similar to that observed for $\tau > 1$.

4.5 Conclusion

We have characterised the linear stability of a particle concentration gradient settling in the presence of an ambient stratification. The non–zero particle settling speed enters through the Péclet number, $Pe = U_s h/\kappa_T$ and is seen to modify the stability of the corresponding double–diffusive system. We note that different boundary conditions (stress–free and zero particle and solute flux), as well as the exact value of the anisotropy factor Φ were also considered and were seen to have little influence on the stability diagrams presented.

In the absence of an ambient stratification, the critical particle Rayleigh number, R_S, was seen to increase approximately linearly with the Péclet number. The mode of instability remains direct for small values of Pe but becomes overstable (oscillatory) for larger Pe, indicating a qualitative difference with the well–known Rayleigh–Bénard instability. The Péclet number where the transition from direct to oscillatory instability occurs decreases slightly if the Prandtl number σ number is increased, from $Pe = 450$ at $\sigma = 7$ to $Pe = 270$ at $\sigma = 700$. If we consider for example glass particles of radius 10μm settling in water, their diffusion constant is approximately $\kappa_\phi \sim 10^{-8}\text{m}^2/\text{s}$, corresponding to $\sigma = 100$. For a 10cm high particle concentration gradient, corresponding to $Pe = 500$, the fastest growing instabilities are oscillatory and the critical Rayleigh number is of order 10^5 (compared to 10^3 for a solute or temperature gradient).

Table 4.5 summarises the main results of our numerical study of the stability of a double–diffusive system where settling particles play the role of a diffusing component and figure 4-6 shows the curves of critical ambient density Rayleigh number, R_T, as a function of particle Rayleigh number for different values of Pe for $\tau = 0.1$ (figure 4-6a) and $\tau = 10$ (figure 4-6b). A system where the total density is uniform but such

that hot, particle–laden fluid overlies cold, fresh fluid ($R_T, R_S < 0$), is stabilised by the non–zero settling speed of particles, as was the case in the absence of an ambient density gradient. When particles act as the quickly diffusing component ($\tau > 1$), the mode of instability remains oscillatory for all values of Pe and large Péclet numbers ($Pe > 90$) are stabilising, although the critical Rayleigh number does not change significantly. However, if particles diffuse slower than the ambient density, $\tau < 1$, particle–fingers are predicted to appear only for values of R_S orders of magnitude larger than in analogous double–diffusive systems. Moreover, for $Pe > 5$, the mode of instability changes from direct, corresponding to particle–fingers, to oscillatory. For particles settling in a heat water system, this corresponds to a critical radius of 1μm; smaller particles essentially behave as a solute while the preferred mode of instability for larger particles is oscillatory and instabilities occur only for $R_S \sim 10^4$.

In the opposite scenario, where the total density is uniform but where cold and clear fluid overlies hot and particle–laden fluid ($R_T, R_S > 0$), large Péclet numbers were seen to be destabilising. For $Pe > 7$ the fastest growing mode of instability is direct and the stability of the system is seen to depend almost exclusively on the ambient stratification. The particle concentration gradient then fails to stabilise the statically unstable ambient density gradient. If the ambient is stratified through an unstable heat gradient, a concentration gradient of particles larger than 1μm will be unable to impede the development of convective instabilities; the critical size drops to 0.1μm for systems destabilise by a salt gradient. When particles diffuse slower than the density of the ambient fluid ($\tau < 1$), the settling of particles thus changes the qualitative nature of the instability from oscillatory to direct. However, when $\tau > 1$ (as may be the case if the ambient stratification is due to large molecules such as sugar) larger particle diffusion is seen to be destabilising, demonstrating that the instability mechanism relies on the diffusivity contrast between ambient density and particle concentration, as would be the case in a double–diffusive system.

Experimental verification of the validity of the stability diagrams presented here should be the subject of future work. The system describe here may be studied experimentally by examining the stability of a suspension settling in a stratified ambient and where particles are supplied at the top. In particular, measurements of the critical Rayleigh number of a particle concentration gradient settling in a homogeneous ambient as a function of the particle settling speed would be very valuable to the description of certain industrial and environmental flows. In the presence of a stratified ambient, experiments would also be valuable to help distinguish between the linear instability discussed here and the instability resulting from the creation of a three layer system via the finite displacement of particles, as will be discussed in chapter 6.

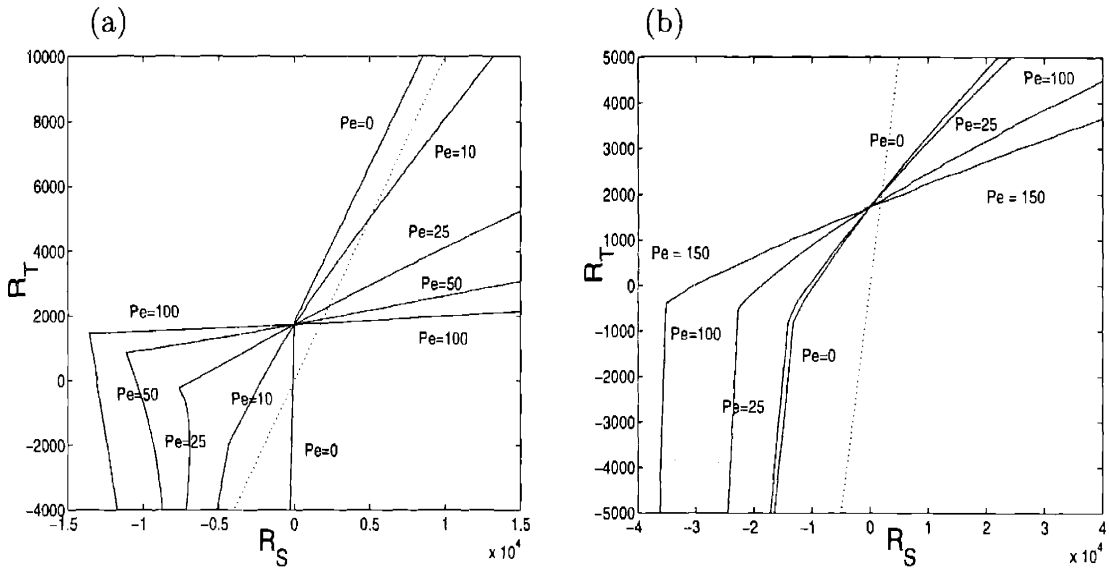

Figure 4-6: Dependence of the critical ambient density Rayleigh number, R_T, on the particle Rayleigh number R_S for different Péclet numbers for a) small diffusivity ratio $\tau = \kappa_\phi/\kappa_T = 0.1$ and b) large diffusivity ratio $\tau = 10$.. The region above and to the left of a solid curve is linearly unstable and that below and to the right is stable. The dotted line indicates the line of neutral buoyancy. The value of the Prandtl number is kept constant at 7, a value appropriate for water stratified through temperature variations.

Chapter 5

Boycott effect in a stratified ambient

5.1 Introduction

Boycott (1920) first reported that the settling rate of red blood cells could be enhanced by tilting the container in which the suspension was kept. He also noted that particle–free fluid left behind by the settling of particles beneath the inclined wall (the Boycott layer) flowed upward ówing to its positive buoyancy relative to the suspension. A heuristic model for the descent rate of suspensions settling beneath an inclined wall was put forward independently by Ponder (1925) and Nakamura & Kuroda (1937). Based on the requirement of volume conservation, the upflow of particle–free fluid is balanced by a corresponding downflow within the suspension, thus accelerating the descent of particles. A more complete theoretical description of the flow was later proposed by Hill, Rothfus & Li (1977) and Acrivos & Herbolzheimer (1979) and was verified experimentally by Leung & Probstein (1983).

The presence of a stratified ambient is expected to significantly alter the evolution of the Boycott effect. In a stable density gradient, fluid carried upward in the Boycott layer will see its density difference with the ambient diminish. If the density gradient is sufficiently strong, fluid in the Boycott layer may reach a height where the density difference due to the absence of particles is balanced by that due to salt. Horizontal intrusions are thus expected to penetrate from the inclined wall into the suspension. Horizontal layers are also known to form in doubled–diffusive systems. When a salinity gradient is heated from below (Turner 1985) or from the side (Huppert & Turner 1978), hot fluid rises to its level of neutral buoyancy and generate layers with typical height scaling as $\Delta\rho_T/(d\rho/dz)$, where $\Delta\rho_T$ is the density difference due to temperature and $d\rho/dz$ is the ambient density gradient. Sloping boundaries in double–diffusive systems may also generate layers as the convective motion generated by the faster diffusing component is opposed by the density stratification due to the slowly diffusing component (Linden & Weber 1977).

In this chapter, we present the results of a combined experimental, theoretical and numerical study of the Boycott effect in a stratified ambient and we compare layers

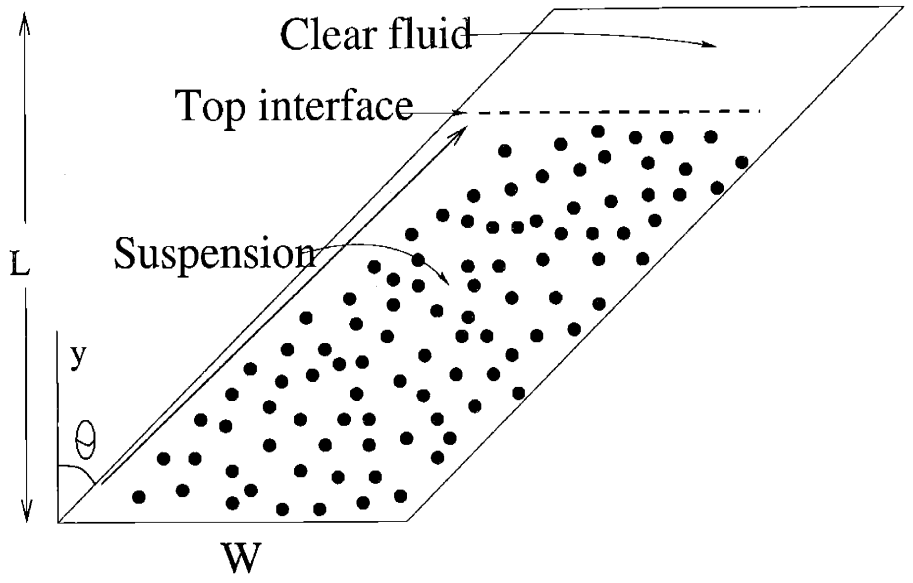

Figure 5-1: Schematic of the Boycott effect. Particles settling beneath a wall making an angle θ to the vertical leave behind a buoyant layer of clear fluid which rises along the wall.

resulting from intrusions of the Boycott layer in the bulk of the suspension with those observed in double–diffusive systems. We first describe the dynamics of the Boycott effect in homogeneous and stratified ambients in §5.2. We present our experimental study of the stratified Boycott effect in §5.3 and a discussion of our measurements and observations is given in §5.4. A numerical model of the evolution of the particle concentration in a suspension marked by convecting layers is introduced in §5.5 and we present numerical simulations of the formation of layers by the Boycott effect in the presence of an ambient stratification in §5.6. We conclude by investigating the applications of this layering mechanism to magma chambers in §5.7. Note that most of these results may be found in a paper by Peacock, Blanchette & Bush (2003).

5.2 Boycott effect

5.2.1 Homogeneous ambient

We begin by describing the Boycott effect as observed in a homogeneous ambient (Acrivos & Herbolzheimer 1979). When particles settle away an inclined wall, a layer of clear fluid is created, the so–called Boycott layer. The density of the suspension is greater than that of the clear fluid present in the Boycott layer. Fluid within the Boycott layer therefore ascends owing to its buoyancy, dragging particles upward as it does so. Eventually, an equilibrium is achieved where the settling of the particles is countered by the vertical motion of the fluid. In steady state, the velocity perpendicular to the wall, v, must balance the settling of particles, therefore scaling like the particle settling speed U_s. Using the length of the inclined wall L as a typical length

scale, continuity requires

$$\frac{u}{L} \sim \frac{v}{\delta} \sim \frac{U_s}{\delta}. \tag{5.1}$$

In many geophysical and laboratory settings, the Reynolds number of the flow is small and the buoyancy force in the Boycott layer is balanced by viscous forces

$$g\Delta\rho\ \phi \sim \frac{\rho\nu v}{\delta^2} \tag{5.2}$$

where $\Delta\rho$ is the density difference between particles and fluid, ϕ the particle concentration, ν the kinematic viscosity and ρ the density of the fluid. The velocity along the wall and the layer thickness thus scale as

$$v \sim U_s\Lambda^{1/3} \qquad\qquad \delta \sim L\Lambda^{-1/3}. \tag{5.3}$$

Where $\Lambda = (9/2)(L/a)^2\phi$, is the governing non-dimensional parameter, a being the particle size. In most practical settings, Λ is large with values greater than 10^6. The analysis of Hill, Rothfus & Li (1977) and later that of Acrivos & Herbolzheimer (1979) yield a more precise result in terms of the angle of inclination θ. In the initial stages of the motion, the thickness and fluid velocity in the Boycott layer are time dependent

$$\delta(x,t) = U_s \sin\theta\Lambda^{1/3}t \qquad v(x,y,t) = U_s\cos\theta\Lambda^{1/3}\left(1 - \frac{y}{2\delta(x,t)}\right)\frac{y}{\delta(x,t)} \tag{5.4}$$

where x is the distance along the wall and y is perpendicular to the wall. The Boycott layer grows until it reaches an equilibrium thickness at which point

$$\delta(x) = x^{1/3}(\tan\theta)^{1/3}L^{2/3}\Lambda^{-1/3} \qquad v(x,y) = U_s\Lambda^{1/3}\cos\theta\frac{x}{L}^{2/3}\left(2 - \frac{y}{\delta(x)}\right)\frac{y}{\delta(x)}. \tag{5.5}$$

From this it is seen that the flux along the wall is exactly the horizontal projection of the inclined wall multiplied by the settling speed

$$u\delta = LU_s\tan\theta. \tag{5.6}$$

Note that the same argument can be applied when fluid containing buoyant particles, such as bubbles overlies an inclined wall.

The rate of descent of the clear fluid interface at the top of the tank may be determined using the fact that there must be no mean vertical flux in the tank. There is thus a downflow in the bulk to counter the upflow of the Boycott effect. We here neglect the thickness of the Boycott layer and assume that the flow is uniform across the tank; these assumptions are well justified if $W \gg \delta$, W being the width of the container. Experiments show that the top interface remains nearly horizontal, which supports the assumption of particle concentration uniformity. Thus, for a tube

making angle θ with the vertical, as in figure 5-1, the interface velocity at height y is

$$u_i(y) = -U_s \left(\frac{y \tan\theta}{W} + 1 \right) \tag{5.7}$$

This result was derived independently by Ponder (1925) and Nakamura & Kuroda (1937) and is commonly referred to as the PNK equation.

5.2.2 Stratified Ambient

The presence of a stratified ambient is expected to significantly alter the evolution of the Boycott effect. If the ambient is stably stratified by a salinity gradient, fluid carried upwards in the Boycott layer will see its density difference with the ambient diminish. If the density gradient $d\rho/dy$ is sufficiently strong, fluid in the Boycott layer reaches a height h_n, at which the density difference due to the absence of particles is balanced by the density difference due to salt. This height satisfies

$$\int_0^{h_n} \frac{d\rho}{dy} dy = \Delta\rho \ \phi \tag{5.8}$$

where $\Delta\rho$ is the density difference between particles and the ambient fluid. For the case of a constant density gradient we thus have

$$h_n = \frac{\Delta\rho \ \phi}{d\rho/dz} \tag{5.9}$$

If h_n is greater than the height of the container, h, one expects that the flow is not significantly altered by the stratification. The Boycott effect then acts as a mixing mechanism in bringing fluid from the base to the top of the tank. The density gradient is thus eroded faster than it would be through the effect of diffusion alone. If $h_n < h$, fluid in the Boycott layer becomes neutrally buoyant and is expected to intrude into the bulk giving rise to a series of layers. To test this physical picture, we performed a series of experiments in which particles settled in a salt stratified ambient, which we describe in §5.3

5.3 Experimental investigation

5.3.1 Experimental method

We proceed to investigate experimentally the combined influences of the Boycott effect and ambient stratification. A schematic picture of the experimental apparatus is presented in figure 5-2. The container was a perspex tank 25cm high ($h = 25$cm), 40cm long and 2.5cm wide, with vertical sidewalls. The top was open and the sidewalls slotted to facilitate the introduction of a sloping wall, at an angle of 45° across the center of the tank. Holes were drilled in the base of the tank to allow it to be filled

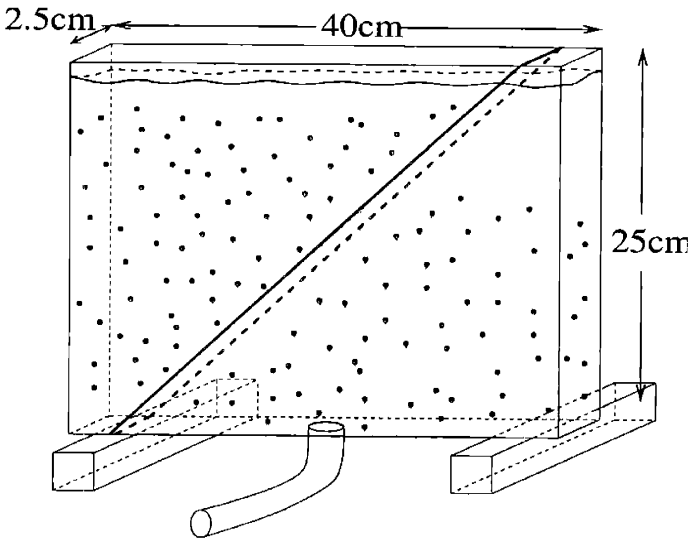

Figure 5-2: A schematic illustration of the apparatus used to study the Boycott effect in a stratified ambient. The inclined wall was inserted after filling the tank.

from below. Vibration control mounts were used to level the system and isolate the tank from exterior mechanical disturbances.

Two different configurations were used in the experiments. The first one involved silica particles of density 2.65kg/m^3 settling in stratified salt water. Using the Richardson–Zaki formula (Richardson & Zaki 1954), it was estimated that the particle radius was $4.1 \pm 0.8\mu$m. The corresponding Stokes settling speed of the particles was 65μm/s. The volume fraction of particles used was typically 0.3%. The second configuration involved glass spheres of radius $17.5 \pm 1.5\mu$m settling in a salt stratified solution comprising 63% glycerol and 37% water. In the absence of salt, the kinematic viscosity of the mixture was 12.1cS, which gave a settling speed of $88 \pm 15\mu$m/s. The presence of salt increased the viscosity of the solution significantly, giving a kinematic viscosity in excess of 21cS for salt–saturated solutions. To minimise the influence of viscosity variations, only weak salinity gradients were used in this configuration. The effects described in chapter 2 were thus neglected, as the settling speed of the particles varied by less than 50% in all experiments.

The tank was filled from below, and a linear salt stratification established using Oster's double bucket technique (Oster 1965). The volume fraction of particles in both buckets was identical, allowing us to establish an initial state characterised by a linear salinity gradient and a uniform particle distribution. The tank was filled in less than four minutes, insuring than particles did not settle more than 2cm as the tank was filled. A PME salinity probe measured the resulting density gradient, which was initially linear. Once the tank was filled, the sloping wall was introduced; this process took approximately four seconds and was sufficiently slow that disturbances to the ambient fluid were minimised, but fast compared to the time taken for the establishment of the Boycott layer (about 10 seconds). After the wall was introduced, a particle–free layer developed underneath the inclined wall in which fluid was seen

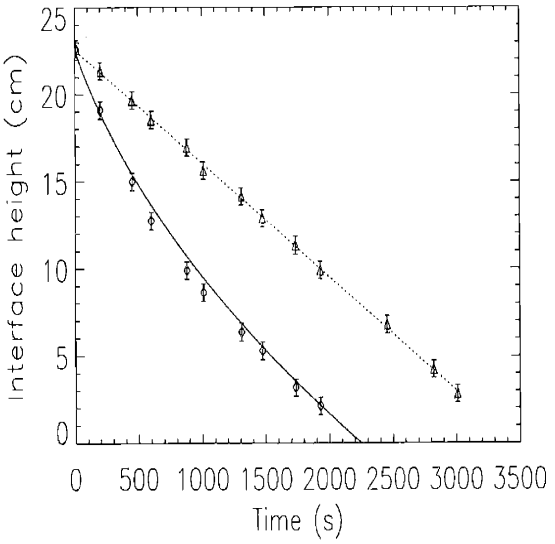

Figure 5-3: Progression of the top interface in a weak stratification. The dashed line represents the position of the top interface in the absence of an inclined wall and the solid line is equation (5.7). Experimental data confirms that the stratification does not affect significantly the progression of the top interface.

to rise. The evolution of the system was found to depend strongly on the ratio h/h_n, as is detailed in the next section.

5.3.2 Observations

We distinguish two qualitatively different regimes: that of a weak salinity gradient where $h_n > h$, and that of a strong salinity gradient where $h_n < h$. We begin by describing the case of a weak salinity gradient.

Weak salinity gradient

If the level of neutral buoyancy is higher than the top of the tank, we do not expect intrusions to form. In our experiments, a Boycott layer was seen to develop underneath the inclined wall, with a typical thickness of 2.5mm and moving with characteristic velocity 0.5mm/s, observations consistent with equation (5.3). The layer of clear fluid extended to the top of the suspension and a sharp interface descended from the top of the tank. The evolution of the height of the suspension was recorded for the glass particles settling in a glycerol–water solution, and the results are presented in figure 5.3.2. The solid line corresponds to the descent rate expected for particles of radius 16mm, the smallest size present in our sample, using equation (5.7). In our trapezoidal geometry, the interface height, $H(t)$, is governed by

$$\frac{dH}{dt}(X - H) = -U_s X \tag{5.10}$$

X being the length of the base of the tank. The dotted line indicates the descent rate of the interface expected for particles in the absence of the Boycott effect.

The clear fluid transported from the base of the tank by the Boycott layer mixed with that already present above the suspension. Introducing dye at the bottom of the container made clear that fluid fluid from the bottom of the container was carried all the way to the top of the suspension. The density of the clear fluid transported from the base of the tank decreases with time. One anticipates the development of a weak stratification in the clear upper layer, as fluid keeps rising along the wall all the way to the top of the container. The evolution of the clear fluid interface and the corresponding salinity profiles are presented in figure 5.3.2. Note that the time taken between obtaining a salinity gradient and the corresponding image was approximately one minute, the time required for immersion and withdrawal of the salinity probe. At time $t = 0$, the interface is at the top of the tank and the density profile is linear throughout; the apparent small scale deviations from linearity are due to the combination of high probe sensitivity, the weak salinity gradient and the motion of the probe through the ambient. After 5 minutes, the profile is linear within the suspension, and shifted downward from its original position. Above the clear fluid interface, the profile is irregular due to mixing. Such an intermediate stage is marked by clear salty fluid overlying a less saline suspension. After 40 minutes, particles have settled out completely and a stratification persists, although it is not as pronounced as it initially was.

Increased mixing in the upper clear fluid region is generated by the salinity jump at the interface between clear fluid and suspension. As particles settle near the interface, they leave behind buoyant fluid which rises in the form of millimetric plumes. the plumes are visible in parts due to the fact that they entrain particles from the suspension. A related scenario arising in a polydisperse suspension has been investigated by Kerr & Lister (1992), who deduced the influence of the associated plume–induced mixing on the descent rate of the suspension. In our system, such mixing is negligible, as evidenced by the good agreement between the descent rate of the suspension and that predicted for the Boycott effect in a homogeneous ambient, figure 5.3.2.

Strong salinity gradient

The experiments described in this section were performed using the smaller particles ($a = 4.1\mu$m) settling in salt water to avoid viscosity variations. The characteristic thickness of the Boycott layer and flow speed were, respectively, 1mm and 2mm/s, again values consistent with equation (5.3). For $h_n > h$, the upflow within the Boycott layer stalled, giving rise to intrusions into the stratified ambient. The lowermost intrusion, which we refer to as the primary intrusion, appeared first and was later followed by a series of overlying secondary intrusions that appeared simultaneously.

We first performed a series of experiments in order to ascertain the dependence of the primary intrusion height, h_p, on $d\rho/dz$. The density gradient was varied from 20 to $300 kg/m^4$ and the volume fraction of particles was kept constant at $\Delta\rho\phi = 5 \pm 0.2 kgm^{-3}$, which yields $1 < h/h_n < 15$. The results are presented in figure 5.3.2, where it is evident that the height of the primary intrusion decreases

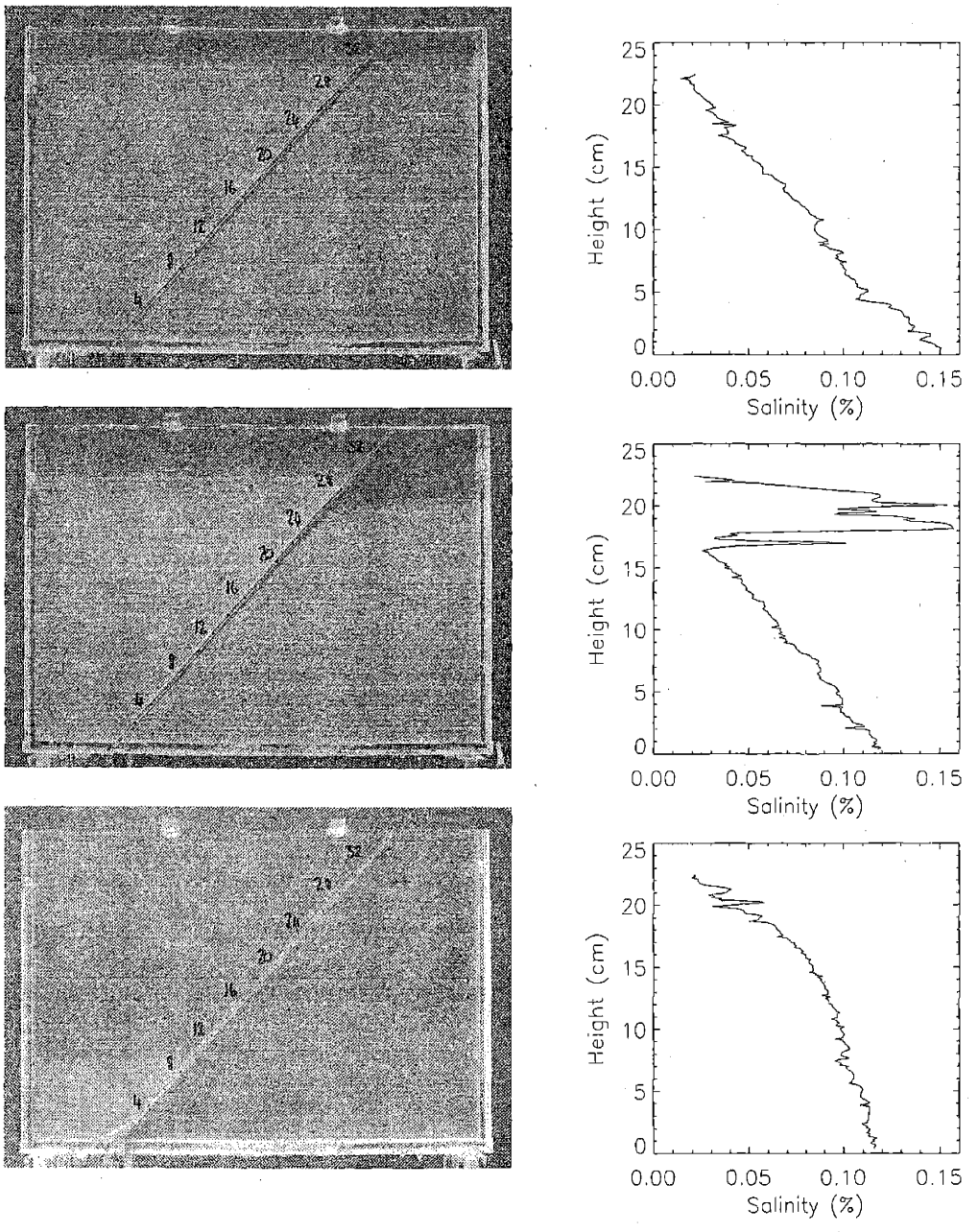

Figure 5-4: Pictures and salinity profiles of the evolution of a weak salinity gradient, $h/h_n = 0.5$ in the presence of the Boycott effect. Picture were taken at times 0min, 5 min and 40 min.

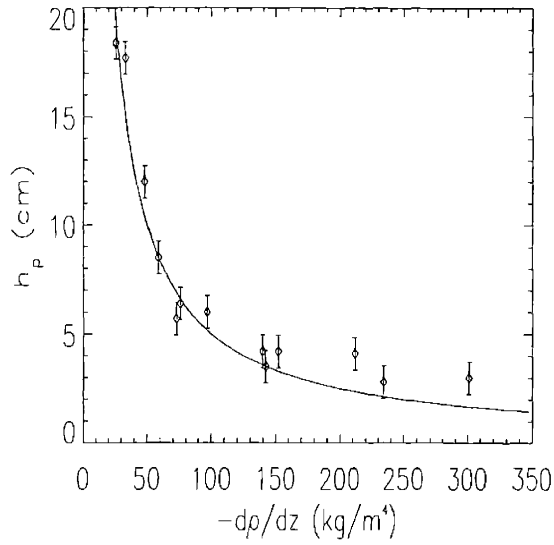

Figure 5-5: The dependence of the primary layer size on the ambient salinity gradient. The layer size is inversely proportional to $d\rho/dz$, in agreement with (5.9)

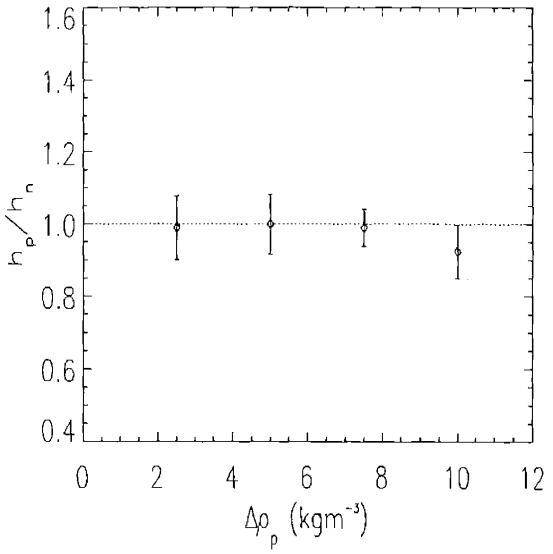

Figure 5-6: The dependence of the ratio of the primary layer size, h_P, to the neutral buoyancy height, h_n, on the initial particle concentration. The ratio h_P/h_n remains constant, showing that intrusions first occur as fluid reaches a height h_n.

monotonically with increasing density gradient. The solid line corresponds to the neutral buoyancy curve, (equation (5.9)). The dependence of h_p on the particle volume fraction was also investigated. Fixing the ambient stratification at $57 \pm 2kg/m^4$, the particle concentration was alternately set to $\phi\Delta\rho = 2.5$, 5.0, 7.5 and $10 \pm 0.1kg/m^3$. The anticipated dependence is again well supported by the data as is shown in figure 5.3.2.

As the system evolved, a layered structure developed throughout the fluid domain on a timescale of several minutes. Each layer was a convection cell characterised by an intrusion at the top and a return flow within the body of the layer. This fluid motion was made visible by the introduction of dye, as shown on figure 5-8. Figure 5-7 demonstrates that no fluid from the primary layer escapes to overlying layers. The Boycott layer thus completely detaches from the wall at the first intrusion. When dye was introduced at an intermediate height, it remained trapped within a single layer, indicating that no fluid was exchanged between layers. The convection within each layer is visualised in figure 5-8 through the transport of dye released from a vertical thread. Motion away from the wall at the top of each layer is countered at the bottom by inflow toward the wall. This convection served to mix the fluid within each layer, eroding the initial linear density gradient and generating step–like density profile, as shown in the salinity profiles in figure 5-7. The layering process was not entirely steady and layers did merge or split on occasions, in a manner reminiscent of layers forming in double–diffusive systems (Tanny & Tsinober 1988). The settling of particles prevented us from studying the long term behavior of the layers in the presence of particles and the ultimate steady state of the layers could not be examined. After all the particles had settled, the step–like density profile persisted until ultimately being eroded through diffusion.

The secondary intrusions were recognisable as disturbances emerging simultaneously from the Boycott layer soon after the development of the primary intrusion, as can be seen in figure 5-8. The size dependence of these intrusions on the density gradient was investigated as previously by varying $\partial_z\rho$ and keeping a constant particle fraction $\phi\Delta\rho = 5kg/m^3$. The observed dependence of mean secondary layer height on stratification is reported in figure 5-9. The secondary layer size, h_s, is smaller than their primary counterparts. Furthermore, the scale of the secondary layers is not inversely proportional to the density gradient of the ambient as one would anticipate from equation (5.9). Rather a best fit line to the results on a logarithmic plot yields the relation

$$h_s = 1.34 \left(\frac{\phi\Delta\rho}{d\rho/dz} \right)^{0.38} \tag{5.11}$$

Observations also indicated that the secondary layer size increased with increasing particle volume fraction. For example, for a density gradient of $\partial_z\rho = 150\text{kg/m}^4$, the layer size increased from approximately 2cm to 2.8cm as $\Delta\rho\phi$ increased from 5kg/m^3 to 16kg/m^3. A few experiments were attempted in the glycerol and water solution, although no useful data were obtained as too few layers were observed and no reliable average size could be discerned. The variable viscosity also invalidates qualitative measurements in this context. However, the secondary layers were clearly observed

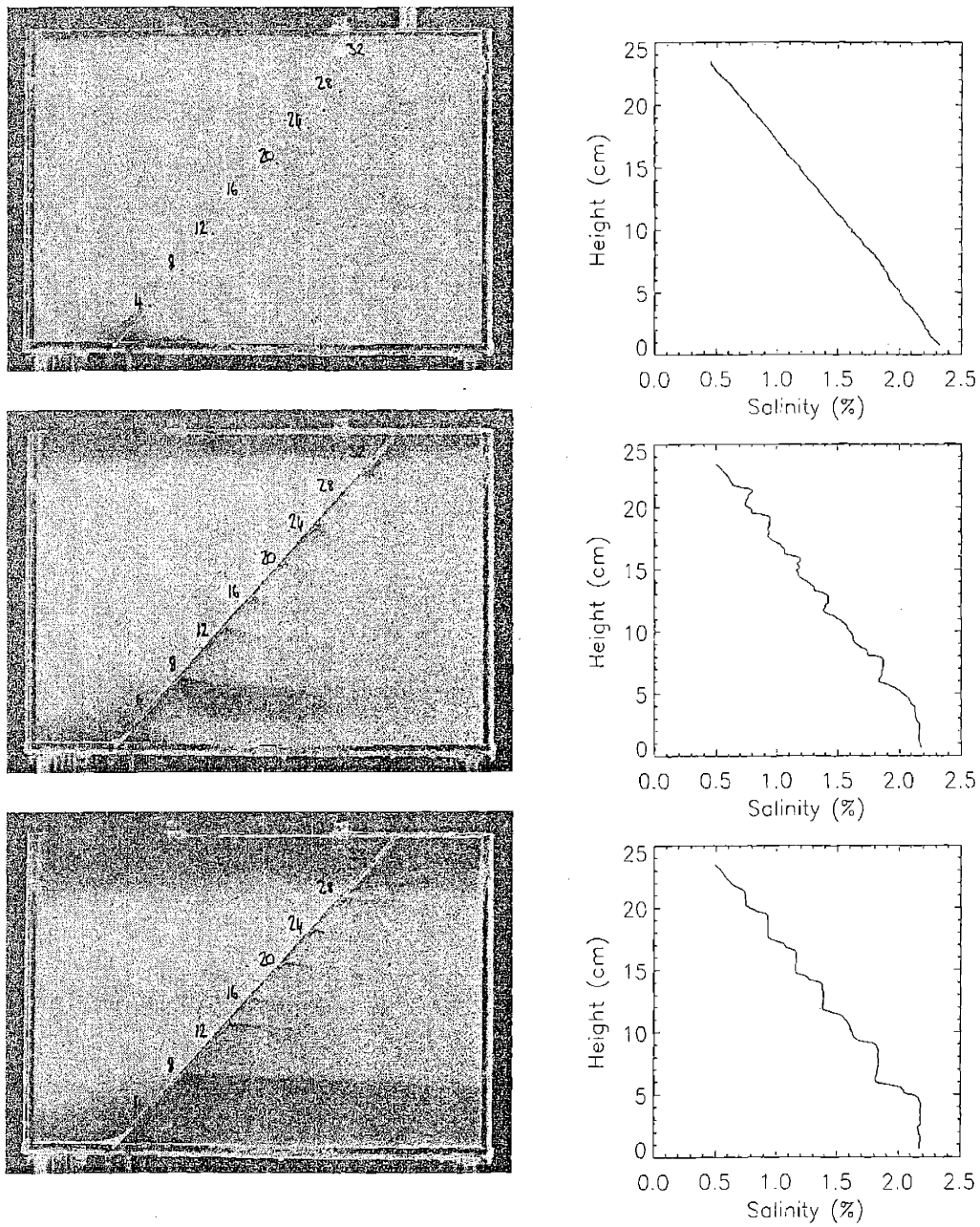

Figure 5-7: Pictures and salinity profiles of the evolution of a strong salinity gradient, $h/h_n = 3.85$ in the presence of the Boycott effect. Picture were taken at times 0min, 3 min and 10 min.

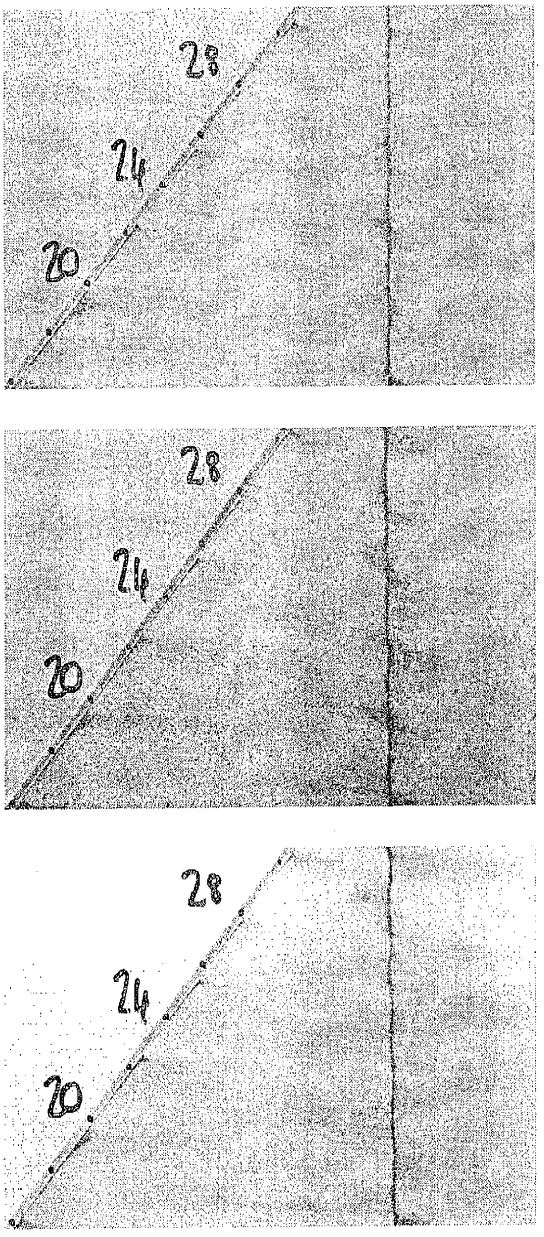

Figure 5-8: Evolution of a vertical streak of dye in a strong salinity gradient, $h/h_n = 7$. Each layer acts as a convection cells. Flow is away from the wall at the top, toward the wall at the bottom.

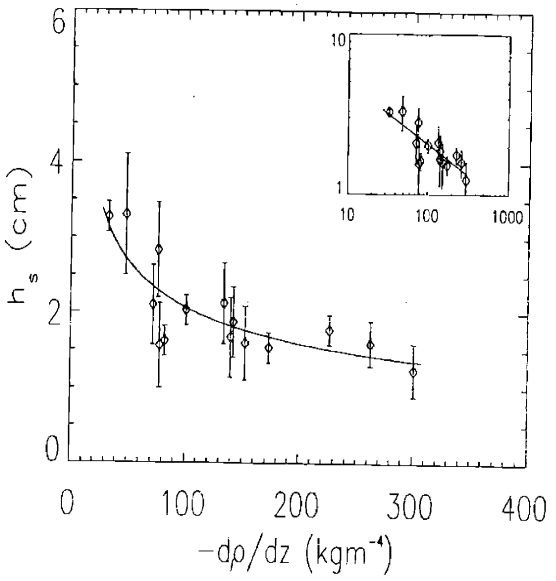

Figure 5-9: The dependence of secondary layer size, h_s, on the ambient density gradient $d\rho/dz$. The layers are smaller than the neutral buoyancy height. The solid line is a best fit showing a dependence of the form $h_s \propto (d\rho/dz)^{-0.38}$

to be larger than in the salt–water solution, by a factor of two or three.

The layers were initially tilted downward, as may be seen in figure 5-7. The salinity at the base of any given layer decreases with time, as progressively less saline fluid is drawn into the Boycott layer. The density of the particle–free fluid in the Boycott layer therefore also decreases with time, and the resulting intrusion height increases accordingly, resulting in an apparent tilt of the intrusion. However, after the layering has evolved for sufficient time, the density within the layer is uniform and the tilting is no longer apparent, figure 5-7. Note that this tilting mechanism is distinct from that observed in thermohaline systems (Huppert & Turner 1980).

The vertical transport of particles between layers was not accomplished through uniform settling. Rather, as a consequence of the density–jump between layers, particle–laden plumes developed and penetrated the clear fluid interfaces (figure 5-10). The generation of microplumes through sedimentation across a density interface has been considered by Hoyal *et al.* (1999) and Parsons *et al.* (2001) and is influenced by the increase of particle concentration required by conservation of particle flux across the interface. A quantitative measure of the overall settling time for the system was difficult to obtain as there was no easily discernible interface separating suspension from particle–free fluid. However, particle settling was clearly impeded by the presence of the layers; in the absence of layers particles settle completely within 40 minutes while they took more than an hour when layers were present.

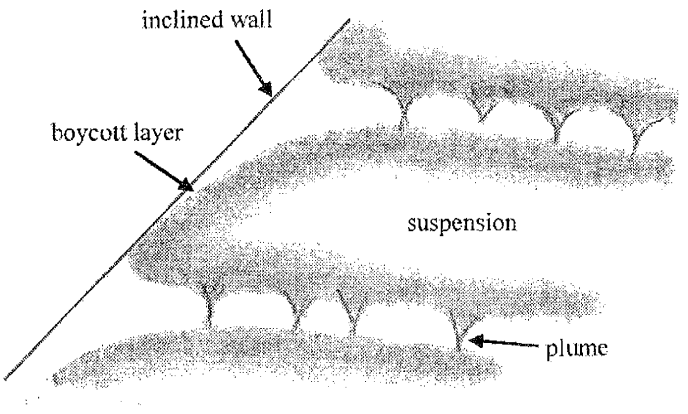

Figure 5-10: The transport of particles between layers formed by the stratified Boycott effect occurs mostly through plumes of particles.

5.4 Discussion

From our experimental investigation, we distinguish two distinct regimes, depending on the relative magnitude of h and h_n. For a weak salinity gradient, $h < h_n$, the Boycott layer transports dense fluid form the base of the tank to the top, where it mixes with clear fluid. This overturning process erodes the linear density gradient. Once all particles have settled, the density gradient is reduced throughout the system. Plumes of low salinity fluid are generated at the interface between the suspension and the overlying clear fluid; as particles settle, clear light fluid is released and may entrain suspended particles (Huppert *et al.* 1991). In our study, particle resuspension has little effect on the descent of the interface and the timescale of settling in the weak salinity limit is the same as that expected for the Boycott effect in a homogeneous ambient.

For a strong salinity gradient, $h > h_n$, the Boycott layer stalled, giving rise to a series of distinct layers. A primary layer first appears with the expected vertical height set by equation (5.9). The primary intrusion appears when clear fluid from the base of the tank reaches its height of neutral buoyancy. The size of the secondary layers, estimated by equation (5.11), is less well understood. A plausible explanation is that clear fluid within the Boycott layer entrains neighbouring sediment laden–fluid. The Boycott layer may then be viewed as a moving sidewall in a stratified ambient. The transfer of kinetic energy of the moving boundary to gravitational potential energy is expected to lead to layers of thickness

$$h_s \sim \frac{u}{N} \tag{5.12}$$

where u is the speed of the boycott layer and N the Brunt–Väisälä frequency $N = (g/\rho)^{1/2}(d\rho/dz)^{1/2}$. In terms of more fundamental quantities, this scaling is equivalent to

$$h_s = \frac{U_s L^{2/3} \phi^{1/3} \rho^{1/2}}{a^{2/3} g^{1/2} (d\rho/dz)^{1/2}} \tag{5.13}$$

which is roughly consistent with equation (5.11). The observed increase of layer size with volume fraction also supports this physical picture as the layer size increases with volume fraction. However, this simple model cannot account for observations made using 17.5μm glass spheres settling in glycerol–water solutions. In that case, U_s was unchanged but the particle size, a, was increased, which one expects to result in a smaller layer size. However, the secondary layer size in several test experiments was seen to be larger than for smaller particles settling in salt water by a factor of two or three.

A second possible explanation is that the Boycott layer itself becomes unstable through the combined effects of shear and density variations. Waves are sometimes seen to propagate along the Boycott layer interface, supporting this hypothesis. The instability would result from the growth of such waves, eventually resulting in intrusions into the ambient. One expects the wavelength of such an instability to scale as the thickness of the Boycott layer itself, δ. It appears that the primary intrusion is not affected by such an instability, presumably because the time scale of growth of the waves is slower than the time scale related to the establishment of the primary layer. The Boycott layer thickness is not constant in the bottom part of the tank, but its size is limited by the first intrusion. The thickness of the Boycott layer grows linearly in time (see equation (5.4)) until is reaches equilibrium (equation (5.5)). The primary intrusion occurs when fluid from the bottom of the container first reaches its level of neutral buoyancy, at which point the Boycott layer is only established in the bottom part of the tank. The thickness above that level is constant and equal to $\delta(h_n)$. The intrusion impedes further growth of the Boycott layer and the thickness in the top part of the container thus remains roughly constant until secondary intrusions appear. If secondary layers result from an instability of the Boycott layer, their size is then expected to scale as

$$h_s \sim \delta(h_n) \sim \frac{1}{\sin\theta} \left(\frac{\Delta\rho\phi}{\partial_z \rho} \right)^{1/3} \frac{a^{2/3}}{\phi^{1/3}}. \tag{5.14}$$

This hypothesis also agrees well with the results of equation (5.11) and with the increase in layer size observed for larger particles. However, the layer size predicted by this scaling is independent of particle fraction, which contradicts observations that the layer size increases slowly with particle fraction (from 2cm to 2.8cm for $\Delta\rho\phi$ changing from 5kg/m^3 to 16kg/m^3).

A discrepancy in the size of primary and secondary intrusions is also reported in thermohaline systems with heated sidewalls (Thorpe 1969, Chen 1971). In this system, heated fluid rises from the base to its neutral buoyancy height, where it intrudes into the ambient. The overlying fluid adjacent to the wall is everywhere neutrally buoyant, and temperature and salinity gradients exist perpendicular to the

wall. The sideways diffusive instability, which relies on the presence of horizontal gradients of both heat and salt, initially proposed by Thorpe (1969) and further studied by Hart (1971) is then responsible for generating the secondary intrusions. The lengthscale of secondary intrusions in the thermohaline problem was found to scale as $(\partial_z \rho)^{1/6}$ (Hart 1971), however the constant source of energy provided by sidewall heating gave rise to layer mergings so that the secondary layers eventually scaled as $(\partial_z \rho)^{-1}$. In the stratified Boycott effect, a similar situation arises; once the primary intrusion has developed, overlying clear fluid underneath the wall is everywhere neutrally buoyant. However, there is no clear analog of the sideways diffusive instability in our system. Given that we observed layer mergings, it is conceivable that in the presence of a constant source of energy, such as a steady supply of particles from above, the secondary layers would ultimately merge to give a layer size inversely proportional to the density gradient, as in the analogous thermohaline problem.

We have assumed here that the salinity in the Boycott layer remains constant as fluid is carried upward. This assumption is expected to hold if the time taken for fluid to rise in the Boycott layer across the container, t_s, is less than the diffusion time of salt across the Boycott layer, t_d.

$$t_s = \frac{L}{U_s \Lambda^{1/3}} \ll \frac{\delta^2}{\kappa} = t_d \tag{5.15}$$

where κ is the diffusion constant of salt in water. Assuming particles settle at low Reynolds number so that

$$U_s = \frac{2a^2 g \Delta\rho}{9\rho\nu} \tag{5.16}$$

and using equation (5.3) this assumption will hold true if

$$1 \ll \frac{t_d}{t_s} \sim \frac{a^{8/3} L^{1/3} g \Delta\rho}{\phi_0^{1/3} \kappa \nu \rho}. \tag{5.17}$$

This inequality holds in general for geophysical and laboratory settings; in the context our our experiments, $t_d/t_s \approx 50$ and geophysical applications are discussed in §5.7.

If the Boycott effect is present in a stratified ambient, the gravitational potential energy of the suspension serves to mix the stratified fluid. The efficiency with which the system converts the gravitational potential energy of the sediment to that of the fluid may be quantified in the following manner. The additional energy due to the presence of particles at the start of the experiment is

$$\Phi_p = \int_V \Delta\rho_p g z dV \tag{5.18}$$

where V is the total fluid volume. After mixing, the increase in gravitational energy of the fluid is

$$\Phi_f = \int_V (\rho_f - \rho_i) g z dV, \tag{5.19}$$

where $\rho_f(z)$ and $\rho_i(z)$ are the final and initial stratifications. The efficiency of the system, $E = \Phi_f/\Phi_p$ was approximately 10% in all experiments considered. We note that much of the energy, Φ_p, was dissipated through the action of the viscous drag on individual settling particles.

5.5 Concentration evolution

Once layers are established in a closed container, they modify the evolution of the particle concentration. Consider a container comprised of steady layers. We assume that each layer has a volume V_i and a base area A_i, and that the convective motions within each layer are sufficiently vigorous to maintain a uniform particle fraction ($U_{con} \gg U_s$). This assumption is justified by experimental data, see §5.3, showing that layers formed by the Boycott effect erode an initial density gradient and evolve to a step profile. The results of Martin & Nokes (1988) may thus be used to determine the time evolution of the particle concentration throughout the system. Their analysis assumes that particles are kept in suspension by the fluid motion, except in a thin boundary layer at the bottom (and top in our case) where viscous effects become important. Particles in the boundary layer region settle out at their Stokes settling speed U_s. The number of particles in a layer is therefore reduced proportionally to the settling speed and to the surface area of the base of that layer. The flux of particles into a layer is given by the flux of particles out of the overlaying layer. Thus

$$\frac{d\phi_i}{dt} = -\frac{U_s A_i}{V_i}\phi_i + \frac{U_s A_{i+1}}{V_i}\phi_{i+1} + \frac{Q_i}{V_i} \tag{5.20}$$

where ϕ_i is the concentration in each layer. We include a source term, Q_i, that may account for new particles that form within a layer, as could be the case for crystals in a magma chamber. This term is also constant within each layer because of convective motions. This system of equations may easily be solved numerically and has analytical solutions for simple source terms.

At all times, the upper layer evolves independently, acting as a source of particles for underlying layers. We consider that the top layer evolves as in the absence of ambient stratification, as is supported by our observations in the weak stratification limit. The overall settling time of the system is thus obtained by combining the Boycott settling time of each layer. For a given geometry, the total settling time may thus be found using equation (5.10). For the trapezoidal geometry used in our experiments, the total settling time is

$$T = \sum_i t_i = \sum_i \frac{H_i}{U_s}\left(1 - \frac{H_i}{2X_i}\right) \tag{5.21}$$

where t_i, H_i, and X_i are respectively the settling time, thickness and base length of the ith layer. A limiting case of interest is that of large n, for which is it seen that the settling time of the system tends to that of an individual particles settling in the absence of the Boycott effect. In this limit, the layers become sufficiently small that

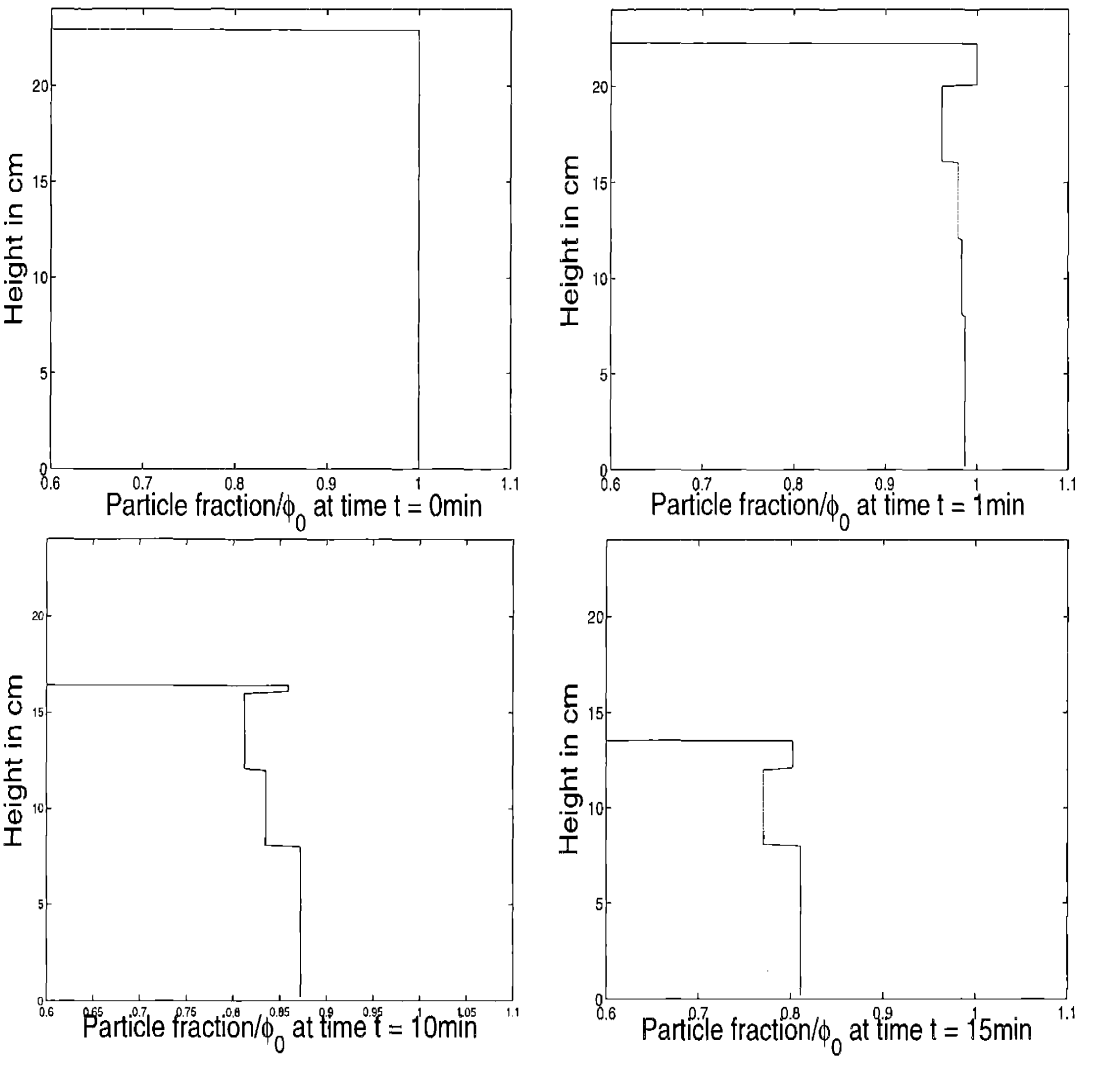

Figure 5-11: The dependence of the normalised particle concentration on height in a layered system at different times (t=0, 1, 10 and 15 min). The top 4 layers are 4cm high and the bottom layer is 8cm high. Each layer is assumed to be well–mixed through the stratified Boycott effect, except for the top most layer where the top interface propagates as it would in the absence of stratification.

the Boycott layer does not appreciably enhance settling within any given layer.

Introducing the notation $\lambda_{i,j} = U_s A_i / V_j$ and denoting by $\vec{\phi}$ the concentration vector ϕ_i for $i = 1...n$, the system of equation (5.20) may be written as

$$\frac{d\vec{\phi}}{dt} = A\vec{\phi} + \vec{q} \tag{5.22}$$

where

$$A = \begin{bmatrix} -\lambda_{1,1} & \lambda_{2,1} & \dots & 0 \\ \vdots & \ddots & \dots & 0 \\ 0 & \dots & \lambda_{n-1,n-1} & \lambda_{n,n-1} \\ 0 & \dots & 0 & -\lambda_{n,n} \end{bmatrix}$$

and the ith element of $\vec{q}$ is Q_i/V_i. The general solution is

$$\vec{\phi} = e^{At}\left(\int_0^t e^{-As}\vec{q}(s)ds + \vec{K}\right) \tag{5.23}$$

where $\vec{K}$ is an integration constant vector determined from the initial conditions. In general, $\vec{q}(t)$ governs the long term behaviour of the solution and the term $e^{At}\vec{K}$ expresses the transient evolution from the initial state.

The simplest case to consider is when $\vec{q}$ is constant in time, corresponding to steady nucleation. An equilibrium concentration $\vec{\phi}_{eq}$ is then achieved. The equilibrium value is found by solving $\vec{\phi}_{eq} = -A^{-1}\vec{q}$, which yields an equilibrium concentration in the ith layer of the form

$$\phi_{eq,i} = \frac{1}{A_i U_s}(Q_i + Q_{i+1} + ... + Q_{n-1} + Q_n). \tag{5.24}$$

An important special case in the context of magma chambers is when crystals form only at the top of the container. The equilibrium concentration in a layer is then $\phi_{eq,i} = Q_n/U_s A_i$. The bottom area of each layer therefore determines the final concentration in suspension. If crystals form uniformly throughout the chamber, then all source terms are equal, and the concentration increases linearly with distance from the top.

The transient term depends largely on the eigenvalues of the matrix A. If the $\lambda_{i,i}$ are all different, the general solution is

$$\begin{bmatrix} \phi_1 \\ \vdots \\ \phi_{n-1} \\ \phi_n \end{bmatrix} = \begin{bmatrix} 1 & \frac{\lambda_{2,1}}{\lambda_{2,2}-\lambda_{1,1}} & \dots & \frac{\lambda_{1,2}...\lambda_{n-1,n}}{(\lambda_{2,2}-\lambda_{1,1})...(\lambda_{n,n}-\lambda_{1,1})} \\ \vdots & \ddots & \ddots & \vdots \\ 0 & \dots & 1 & \frac{\lambda_{n-1,n}}{\lambda_{n,n}-\lambda_{n-1,n-1}} \\ 0 & \dots & 0 & 1 \end{bmatrix} \begin{bmatrix} c_1 e^{-U_s\lambda_{1,1}t} \\ \vdots \\ c_{n-1}e^{-U_s\lambda_{n-1,n-1}t} \\ c_n e^{-U_s\lambda_{n,n}t} \end{bmatrix} \tag{5.25}$$

The time scale of adjustment is thus determined by the $\lambda_{i,i}$. If there are repeated eigenvalues, the form of the solution is slightly altered but the dominant term remains

of the form $e^{-U_s \lambda_{i,i} t}$. From the solution (5.25), we see that the concentration in each layer is influenced only by the overlaying layers, as one expects. The layer in which the concentration of particles decays the slowest will eventually dominate the transient dynamics of all the underlying layers. Therefore, the layer with the greatest value of V_i/A_i will be crucial to the long-term behaviour of the system. In the case where layers are of the same aspect ratio, (i.e.inclined rectangular cracks), the concentration decays exponentially in time, although lower layers will lose particles slightly slower since their time evolution must follow the evolution of overlaying layers.

A simulation of the evolution of the particle concentration for our trapezoidal geometry with six layers, one of which is a primary layer, is shown in figure 5-11. The concentration is initially uniform throughout, and subsequently decreases with height. In our trapezoidal geometry, A_i/V_i and A_{i+1}/V_i both increase with height, as does their difference. Thus, according to equation (5.20),

$$\frac{dc_{i+1}}{dt} < \frac{dc_i}{dt} < 0. \tag{5.26}$$

The concentration thus decreases faster in the upper than lower layers. The only exception to this trend is the top layer, whose settling is prescribed by the Boycott effect. We note that the presence of six layers increases the total settling time by approximately 50%, in good agreement with our experimental observations.

5.6 Numerical simulations

We here describe a numerical model of the formation of layers resulting from the Boycott effect in a stratified ambient. We present a simplified model which allows us to model the system as a system of three partial differential equation involving only one spatial variable. This allows us to monitor efficiently the time evolution of the system and to study the layer size as a function of both particle concentration and ambient stratification over a broad range of parameters.

The governing equations describing particles settling in a fluid containing a solute are

$$\frac{\partial \vec{u}}{\partial t} + \vec{u} \cdot \nabla \vec{u} = \frac{-\nabla P}{\rho} + \frac{\Delta \rho}{\rho} \phi \vec{g} + \beta S \vec{g} + \nu \nabla^2 \vec{u} \tag{5.27}$$

$$\frac{\partial S}{\partial t} + \vec{u} \cdot \nabla S = \kappa \nabla^2 S \tag{5.28}$$

$$\frac{\partial \phi}{\partial t} + \vec{u} \cdot \nabla \phi + U_s \cdot \nabla (1 - k\phi)\phi = \kappa_\phi \nabla^2 \phi \tag{5.29}$$

where $\vec{u}$ is the velocity field, S the solute concentration ϕ the particle concentration, β the expansion coefficient of the solute and κ_ϕ the particle diffusion constant. To simplify computations, we neglect non–linear terms in the momentum equation since the Reynolds number of the Boycott layer flow is small ($O(1)$). A Galerkin method was used to reduce the equations to only the vertical spatial variable, allowing us to monitor the time evolution of the flow in a reasonably small computation time.

5.6.1 Numerical Model

Before solving (5.27-5.29) numerically, we make two simplifying assumptions. We first impose that the particle concentration be constant in time. The analysis of Acrivos & Herbolzheimer (1979) shows that for a uniform initial concentration ϕ_0, the concentration of particles in the bulk remains constant in time. We therefore assume that particles are only present in the bulk and that their concentration remains ϕ_0 over the duration of the simulation. We expect this approximation to hold away from the top of the suspension and near equilibrium in the presence of a constant source of particles. We also make use of experimental observations described in §5.3 and assume that the thickness of the layer of clear fluid is constant, to a first approximation. This is justified by our experimental observations which show no systematic thickening with distance from the corner. We thus consider $\phi = 0$ inside the Boycott layer ($x - z < \delta$) and $\phi = \phi_0$ otherwise, where we consider an inclination angle of $\theta = 45°$, see figure 5-1.

Following Hosoi & Dupont (1996) who studied the formation of layers resulting from the settling of a particle concentration gradient in a horizontally stratified fluid, we employ the Galerkin method to reduce the system to one spatial dimension. We first assume a form of the velocity and salinity field with known horizontal dependencies. We note from experimental observations that vertical upflow is greatest at the interface between the suspension and clear fluid and that there is a weak downflow close to the Boycott layer. The magnitude of the vertical velocity must decay with distance from the wall, which suggests a velocity of the form:

$$u(x,z,t) = f(z,t)e^{-k\tan\Phi(x-z)}\left(\sin(k(x-z)+\Phi) - \sin\Phi\right) \tag{5.30}$$

where k is specified from experimental parameters. This form of the velocity can be seen to have 0 vertical flux and to vanish at the wall. Using the continuity equation and no–slip boundary conditions we can compute the corresponding horizontal velocity field.

$$v(x,z,t) = -\int_0^x \partial_z u(x',z,t)dx' \tag{5.31}$$

We choose the salinity field, S, as the sum of a background component $Sa(z,t)$ and a perturbation $b(z,t)$. The perturbation decays exponentially as did the velocity and we require that the x–derivative vanish at the boundary, which guarantees no horizontal S flux. Although this does not insure that there is no diffusive flux at the boundary, the time scale of diffusion being much slower than the advection time scale $Pe = U_s h/\kappa \gg 1$, this shortcoming is expected not to have much influence on the results. Conservation of solute also requires that the perturbation term integrates to 0 so that it does not affect the total amount of solute in the system, which leaves us with

$$S(x,z,t) = Sa(z,t) + b(z,t)e^{-k\tan\Phi(x-z)}(\sin(k(x-z)+\psi) - \sin(\psi) + \frac{\cos(\psi)}{\tan\Phi}) \tag{5.32}$$

where $\tan(\psi) = (1+2\tan^2\Phi)/\tan\Phi$.

Using the Galerkin method, we chose the test functions to be of the same form as the velocity and S fields (Hosoi & Dupont 1996). To derive equations in terms of $f(z,t)$, $Sa(z,t)$ and $b(z,t)$, we multiply the corresponding equations by test functions (take a dot product for equation 5.27) and integrate over the domain. We consider a domain restricted by $x = z$ and $x = W + z$ in the horizontal direction, and $z = 0$ and $z = L$ in the vertical direction. Integration against test functions may be done using the Mathematica software. The resulting equations are in terms of z and t and involve only $f(z,t)$, $Sa(z,t)$ and $b(z,t)$, from which one may readily recover the velocity and S fields.

The parameters to specify are Φ, δ, k and L. The relevant length scale is the size of the layer of clear fluid so we use the length scale $1/k$ to non–dimensionalize the equations. The maximum velocity occurs at a distance δ from the wall, which yields

$$\cos(2\Phi + k\delta) = -\sin^2\Phi. \tag{5.33}$$

The decay rate $-k\tan\Phi$ may be approximated following the results of Acrivos & Herbolzheimer (1979), to be $1/\delta$ and δ is estimated using equation (5.3). We may thus find the wavelength k and the phase angle Φ. Using the parameters corresponding to glass particles settling in salt–stratified water mentioned in §5.3 we find

$$0.2 - 1.6\ b - 1.6\ f + 0.9\ \partial_{zz}f - 0.3\ \partial_{zzzz}f = 0 \tag{5.34}$$

$$6.3\ \partial_t Sa + 0.15\ \partial_z\,(bf) = \kappa'(6.3\ \partial_{zz}Sa + 1.1\ \partial_z b) \tag{5.35}$$

$$0.3\ \partial_t b + 0.01\ (f\partial_z b + \partial_z\,(bf)) + 0.15\ f\partial_z Sa = \kappa'(0.3\ \partial_{zz}b + 0.3\ \partial_z b - 0.3\ b) \tag{5.36}$$

where κ' is non-dimensional.

Our algorithm was implemented using finite elements and is explicit in time with second order accuracy in space, except for non linear terms where upwinding is used. Second order accuracy in time is also achieved by considering

$$f^{n+1} = 2\bar{f}^{1/2+1/2} - \bar{f}^{n+1} \tag{5.37}$$

where $\bar{f}^{n+1}$ is the result of a time increment of Δt and $\bar{f}^{1/2+1/2}$ is the result of two time increments of $\Delta t/2$. Adaptive time stepping allowed us to insure that the error of any particular step is small. The presence of shocks forced us to introduce artificial diffusion (Hosoi & Dupont 1996). To insure that shocks do not generate spurious oscillations in the velocity and salinity fields, the diffusion constant is modified following Hosoi & Dupont (1996) and is taken to be $\kappa = \kappa_{Sa} + |f|\Delta z\ \Delta\bar{Sa}\ \Theta_{Sa}$, where κ_{Sa} is the physical diffusion constant, $\Delta\bar{Sa}$ is the average variation of Sa in a neighborhood of two mesh points and Θ_{Sa} is a constant chosen to be as small as possible while still preventing overshoot at the shocks. It was seen that the added term was comparable to the physical diffusion constant, or smaller. A similar effective diffusivity was used to trace the evolution of the solute concentration b.

The horizontal averaging associated with the Galerkin method effectively reduces the magnitude of the Boycott effect compared to the magnitude of the diffusion of the solute. Therefore, in order to study the dependency of the layer size on differ-

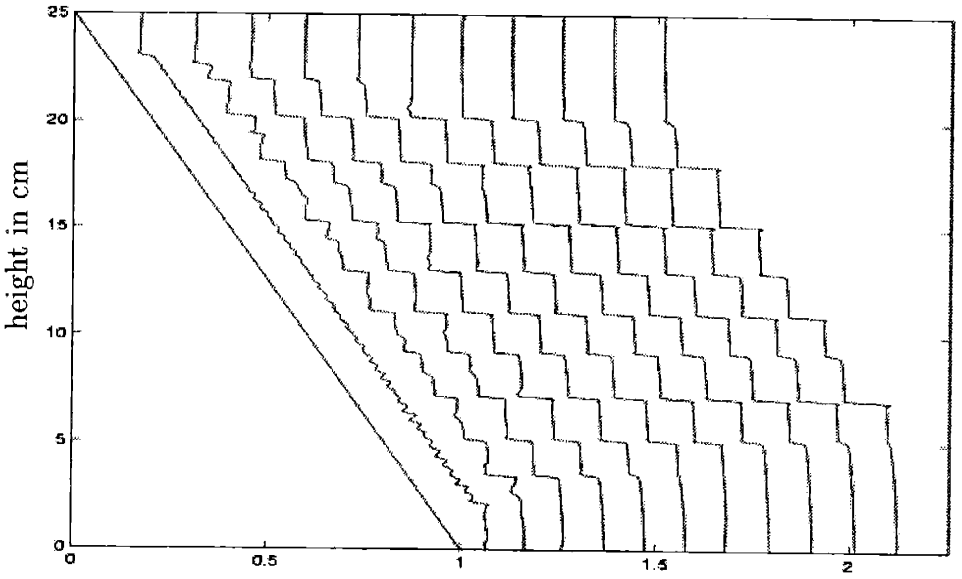

Figure 5-12: The time evolution of the dependence of the background salinity profile S on height in the presence of the stratified Boycott effect. Here the initial concentration gradient is of 150kg/m^4, the particle mass fraction is 5kg/m^3, $a = 5\mu$m and $\rho_p =$ 2g/cc. Starting from a linear salinity gradient, a step–like profile develops, indicating the formation of layers. Plots are shifted to the right by 0.12 for each $30s$.

ent parameters, we reduced the thickness to only a couple of periods of the model functions $\sin(k(x-z)+\psi)$. Experiments were performed to see if the width of the container,W, influenced the observed layer size. For values of W ranging from one to seven periods of the test functions, the layer size did not change in a systematic fashion. Therefore, our results for small W should apply for larger values. This is also justified by the fact that by making the tank narrower, we neglect only diffusive terms and perturbations due to the Boycott layer which decay exponentially.

5.6.2 Numerical Results

To allow comparison with the experiments of §5.3, simulations were first performed using the following parameters: $a = 5\mu$m, $L =$ 25cm, $\nu = 10^{-2}$cm$^2/s$, $g = 9.81$m/s^2, $\rho =$ 1g/cm^3, and $\kappa = 10^{-9}$m^2/s. The added density due to particles was varied between 1 and 15kg/m^3. The computations were started with an initial state for which the density profile was a linear gradient, the density gradient varying between 5 and 300kg/m^4. The initial velocity of the fluid was taken to be zero. Different initial conditions were tested but the results were seen to depend weakly on initial velocity conditions.

For most of the range mentioned above, layers were seen to form in succession from the top and bottom boundaries. Starting from a linear S profile, the concentration is seen to become quickly irregular. Layers of constant solute concentration then

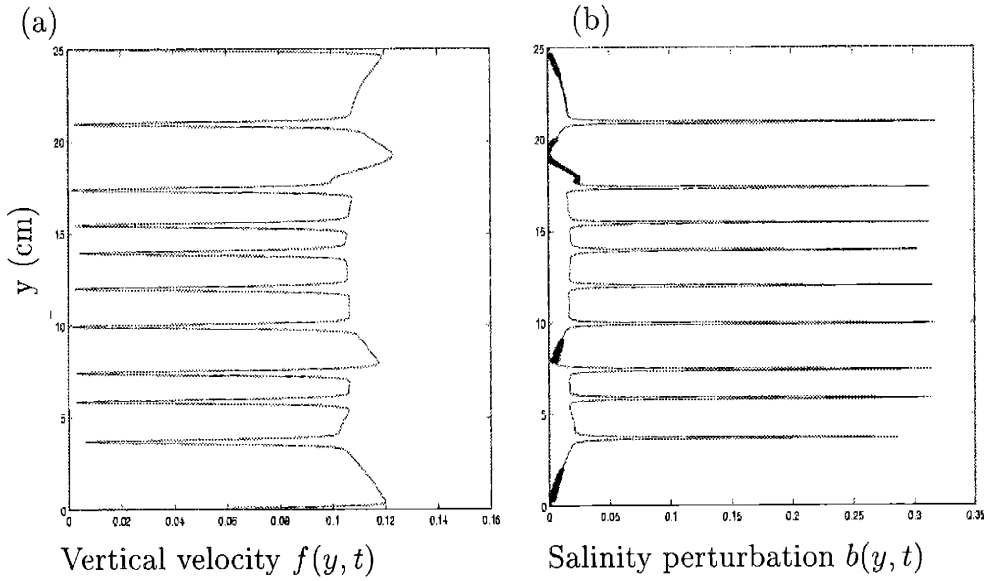

Figure 5-13: Numerical simulations of the stratified Boycott effect. Figure (a) illustrates the dependence of the magnitude of the vertical velocity, $f(y,t)$, on the distance from the bottom of the container, y. Figure (b) shows the dependence of perturbations to the background solute concentration, $b(y,t)$ on height y. Here the initial concentration gradient is 150kg/m,[4] and the initial particle mass fraction is $5kg/m^3$. Each spike corresponds to an intrusion and a typical layer size is of the order of 2cm.

appear near the top and bottom of the container. This indicates regions that have become well–mixed through the action of the Boycott effect. New layers then form in succession from both ends, see figure 5-12. The two sets of layers eventually merge and reach an equilibrium. The first and last layer continue to grow but on a timescale much smaller than that of the establishment of the intermediate bulk layers. The extremal layers were seen to grow as $t^{1/2}$, compared to t for the formation of the central layers; the growth of the upper and lower layers was therefore due the salt diffusion through the effect of the no–flux requirement at the upper and lower walls. The central layers are of uniform size and always smaller than the extremal ones.

The initial velocity of the upflow along the wall is nearly constant. However, as layers of constant S form, the vertical velocity drops sharply at the interfaces, signaling an intrusion, as may be seen in figure 5-13a. The horizontal velocity away from the wall also increases at the interfaces. Within each layer however, the vertical velocity in the Boycott layer is nearly constant and is the same in all layers. Similarly, the perturbations to the solute concentration b are seen to be small except at density jumps where they exhibit a very sharp peak as can be seen in figure 5-13b. The resulting flow pattern is thus a sequence of convection cells where the fluid moves upwards quickly along the wall, then intrudes inwards abruptly and goes slowly downwards away from the wall, in a manner consistent with experiments. The time scale

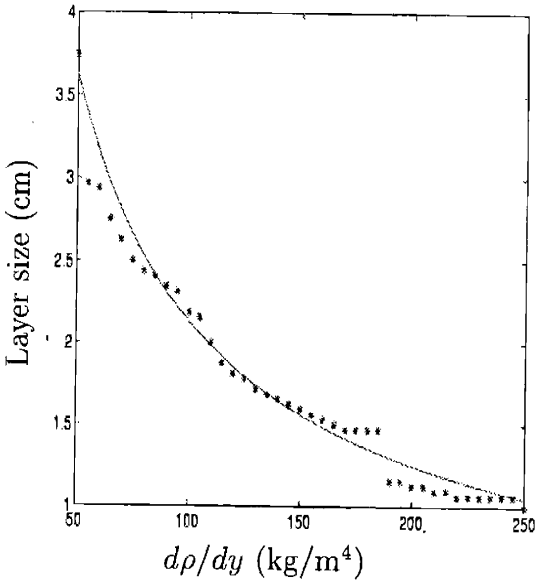

Figure 5-14: Numerical simulations of the stratified Boycott effect showing the dependence of layer size on the ambient density gradient for a particle fraction of 5kg/m^3, with $a = 5\mu$m, $\rho_p = 2$g/cc and water as the ambient fluid. The stars are numerical data, the solid line is the theoretical relation (5.38).

of formation of the layers was of the order of minutes, comparable to the experiments of §5.3 where the first layer appeared after about one minute. The size of the layers was of the order of centimeters, again in good agreement with our experiments.

Having established that our numerical simulations reproduce qualitatively the formation of layers through the Boycott effect, we now study the dependence of the layer size on the particle concentration and ambient density gradient in conditions similar to those of the experiments presented of §5.3. The parameters where thus set to: $a = 10\mu$m, $L = 25$cm, $\nu = 10^{-6}$m^2/s, $g = 9.81$m/s^2, $\rho = 1000$kg/m^3, $\kappa = 5 \cdot 10^{-9}$m^2/s. The added density due to particles was varied between 5 and 75kg/m^3. The computations were started with an initial state where the density profile is that of a linear gradient in S with a density gradient varying from 15kg/m^4 to 300kg/m^4.

We studied the layer size as a function of both particle concentration and density gradient. As expected from the theory and experiments, the layers became smaller with larger density gradients and increased with larger particle concentration. The scaling of the layer size

$$h_n = C \frac{\phi_0}{\rho \frac{d\rho}{dz}} \tag{5.38}$$

was qualitatively recovered. Specifically, as may be seen on figure 5-14, the layer size decreases with the density gradient. Here the particle mass fraction was 5kg/m^3 and a typical layer size is 2cm, in agreement with experimental results. We display here results for the size of the first layer and a similar behaviour is seen for the average

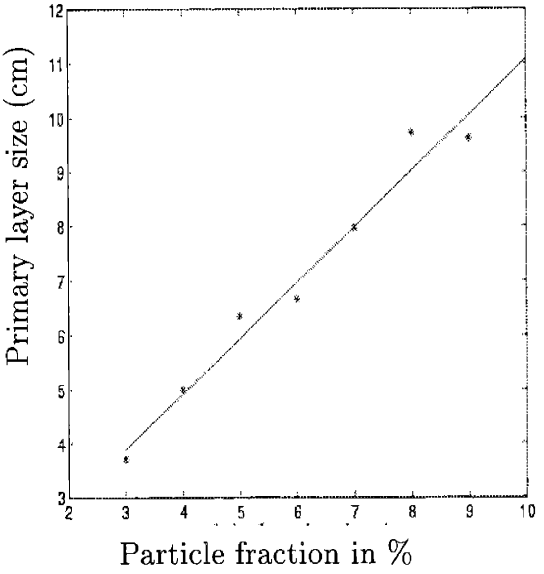

Figure 5-15: The dependence of the primary layer size on particle concentration in the presence of a $150kg/m^4$ density gradient. The stars are numerical data, the solid line is the theoretical relation (5.38).

layer size. The dependence of the layer size on particle concentration also yields good agreement with the theory, the layer size increasing almost linearly with increasing ϕ_0, (figure 5-15). The data here is somewhat irregular because of the discreteness of the number of layers, which leads to apparent discontinuities in the layer size. However, the trend clearly supports the theory and the results are in qualitative agreement with experiments.

The approximation of constant particle concentration made in our model does not allow us to make precise quantitative predictions for the layer size. However, the general agreement between numerics, experiments and scaling indicates that this simple model contains all the physics relevant to the formation of layers by the Boycott effect in a stratified ambient. More detailed simulations are required to describe adequately the formation of secondary layers and will be the subject of future work.

5.7 Application to magma chambers

5.7.1 Introduction to magma chambers

Magma chambers are large reservoirs of molten material contained in solid rock within the earth's mantle. Their geometries vary from roughly spherical to planar, with characteristic dimensions ranging from 100m to 10km (Smith 1979). Convective motions and crystal settling have long been thought to play a role in the dynamics of magma chambers (Darwin 1844). The chamber is typically filled rapidly with hot magma from the Earth's mantle and subsequently isolated; however, reinjections of magma

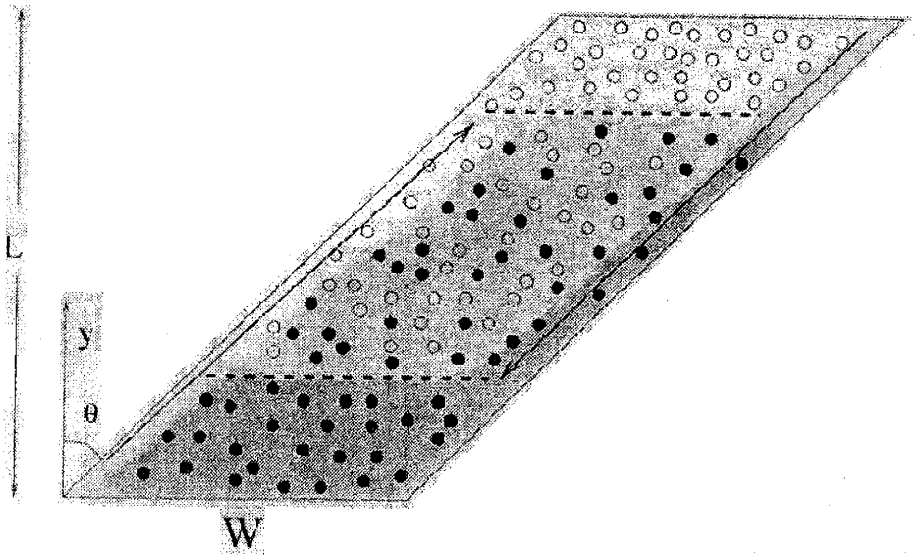

Figure 5-16: Heavy particles (dark circles) settling beneath an inclined wall give rise to an upward flowing, particle–free Boycott layer, seen as the pale layer. Conversely, bubbles (light circles) rising above an inclined wall generate a downward flowing, bubble–free Boycott layer, seen as the dark layer.

from a source conduit may also arise (Huppert *et al.*, 1982). The system is generally cooled from above so that thermally–driven convection may be present. Through magma differentiation, compositional gradients may develop and render the chamber unstable to compositional convection (Spera *et al.*, 1986). The temperature difference across the chamber is diminished by the convective mixing, and viscosity increases as the chamber cools until thermally–driven convection becomes negligible (Jaupart *et al.* 1995). Through magma differentiation, compositional gradients may develop and render the chamber unstable to compositional convection (Spera *et al.* 1986). Crystals, either present when the chamber was initially filled or formed as the chamber cools, and small bubbles of gas or low viscosity liquids (volatiles) (Greenough *et al* 1999) may subsequently come to dominate the dynamics of the magma chamber (Jellinek *et al.* 2001). As the chamber cools, the concentration of crystals increases until a crystal matrix forms and the interior of the magma chamber effectively becomes a porous medium (Schoofs *et al.* 1998). Eventually all the magma solidifies and interior motion is suppressed.

At the base of solidified magma chambers, compositionally distinct layers are often observed. These layers have been reported in Greenland (Hodson 1998), Québec (Loncarevic *et al.* 1990) and South Africa (Jaupart *et al.* 1995), and their origins are the subject of this letter. The individual layers are typically less than one meter deep and the strata may span up to 100m. In the majority of cases, the composition of the layers varies monotonically with height and the mean density within each layer decreases with height. Vesicular rock layers, those exhibiting high concentrations of volatiles, have been seen in Taiwan (Greenough *et al.* 1999) and Washington state

(McMillan *et al.* 1989). Vesicular layers form near the top of the chamber and usually only a few such layers are observed, with depths of order 20cm. A variety of mechanisms have been proposed to explain the formation of layers in solidified magma chambers, but have been difficult to confirm owing to the complexity of the system, the number and indeterminacy of the governing parameters and difficulties in obtaining reliable data.

One explanation for the existence of layers at the bottom of a magma chamber is the repeated injection of melt (Huppert *et al.* 1982), (Jaupart *et al.* 1995): new magma is introduced periodically at the base, each injection leading to the formation of a new layer. An alternative mechanism relies on episodic crystal settling from a convecting chamber cooled from above (Sparks *et al.* 1993); when the concentration of crystals becomes sufficiently large, convection is unable to keep them in suspension, leading to a deposition event. The repetition of this process yields a layered deposit. Another proposed layering mechanism relies on the time-periodic nucleation of two chemical species of crystals; (Hort *et al.* 1993, McMillan *et al.* 1989). Irvine (1987) and subsequently Hodson (1998) proposed that layers are the result of deposition from particle–driven gravity currents; if a large quantity of crystalline matter generated within the chamber is suddenly released from the top of the chamber, it will sink and spread as a gravity current along the base of the chamber. Particles then sediment out as the current spreads, leaving a deposit that thins with distance from the source. While the dynamics of particle–laden gravity currents are well understood (Bonnecaze *et al.* 1993), the origin of the required large mass of particles is unclear.

A number of explanations for the existence of layers in solidified magma chambers rely on the presence of convecting layers within the molten chamber (Hodson 1998); however, the origin of such layers remains uncertain. Double–diffusive convection has been suggested as a possible origin (Jaupart *et al.* 1995); however, in magma chambers the temperature and compositional gradients are not independent, and numerical simulations suggest that no such steady layers may form (Spera *et al.* 1986). Time dependent layers may form by the heating from below of a compositional gradient (Turner 1968, Huppert *et al.* 1979); a similar mechanism may operate in porous media (Schoofs *et al.* 1998), and so may be relevant in the limit of high crystal concentration. Alternative mechanisms for layer formation in magma chambers rely on sidewall cooling (or heating) of a density gradient (Jaupart *et al.* 1995, Huppert *et al.* 1980). Heating of a tilted interface in the presence of a chemical gradient may also lead to layer formation (Chen 1971).

The ability of particles to play the role of a diffusing component in a double–diffusive system has been well established. Green (1987) examined the convective instability arising in a stably stratified system marked by hot particle–laden fluid overlying cold fluid and explained the resulting plumes by analogy with salt fingering (Turner 1985). In the presence of a horizontal density gradient, settling particles may also generate convecting layers: Mendenhall & Mason (1923) observed layers when a polydisperse suspension, vertically stratified through differential settling, was heated from the side. In this section, we investigate the possibility that layering through the Boycott effect in a stratified ambient, as discussed earlier in this chapter, may be responsible for the observed layers in magma chambers.

Parameters	Value	References
Height	100m to 10km	McMillan *et al.* (1989), Smith (1979)
η	10^1 to 10^{10} Poise	Shaw (1972), McMillan *et al.* (1989)
ρ	2.5 to 3.0 g/cm^3	McMillan *et al.* (1989), Huppert *et al.* (1993)
ϕ crystals	0% to 10%vol.	Huppert *et al.* (1993), Smith (1979)
ϕ bubbles	0% to 10%vol.	Sahagian *et al.* (1994), McMillan *et al.* (1989)
Crystal size	0.1mm to 3cm	Huppert *et al.* (1993), Jellinek *et al.* (2001)
Bubble size	0.1mm to 2cm	Sahagian *et al.* (1994), McMillan *et al.* (1989)
$\frac{\Delta\rho}{\rho}$	0% to 5%	Hodson (1998), Spera *et al.* (1986)
κ	10^{-11} to 10^{-13}m^2/s	Jellinek *et al.* (2001)

Table 5.1: Estimates for the range of relevant physical parameters in magma chambers

5.7.2 The stratified Boycott effect in magma chambers

Layer formation through the stratified Boycott effect requires the combination of three factors: sloping walls, positively or negatively buoyant suspended material and a stratified ambient. The geometry of magma chambers is such that the presence of sloping walls is inevitable. Crystals are present in magma chambers (Sparks *et al.* 1993) and those that do not attach themselves to the boundaries will settle in the bulk. Similarly, volatiles nucleating throughout the chamber will be suspended in the magma (Jaupart *et al.* 1995). As the magma chamber cools sufficiently that thermal convection is suppressed, thermal or compositional gradients may result in a stable stratification (Hodson 1998). Thus all the components necessary for the formation of convecting layers through the stratified Boycott effect are generally present in magma chambers. We proceed by describing the relevant parameters in more detail.

The size of crystals and bubbles in magma chambers varies widely, but is usually assumed to be of the order of 1mm (Sahagian *et al.* 1994). The density difference between crystals and the ambient magma is approximately 0.5g/cm^3, while that of bubbles is approximately 2.5g/cm^3 (Huppert *et al.* 1993). Bubble volume fractions are usually less than 10% (Sahagian *et al.* 1994) while crystal concentrations may be arbitrarily large. The Boycott effect is only significant for concentrations greater than 0.1%: if too few particles are present, the upflow in the Boycott layer is comparable to the particle settling speed. Temperature and compositional variations, in addition to the presence of particles, significantly affect the magma viscosity. A typical estimate for the viscosity of the molten magma, η, is 5×10^5 Poise (Shaw 1972), but estimates vary by a factor of 10^4. Throughout the body of the chamber, compositional gradients may form through magma differentiation, and it is commonly thought that the total density changes by approximately 5% from top to bottom, SiO_2 being the principal stratifying agent (Spera *et al.* 1986, Hodson 1998). The parameters relevant to the dynamics of magma chambers are summarized in Table 5.1.

We proceed by quantifying the time and length scales that would characterise layers formed in a magma chamber by the stratified Boycott effect. Considering a compositional diffusion coefficient of $10^{-12}m^2/s$ (Jellinek *et al.* 2001), we see from

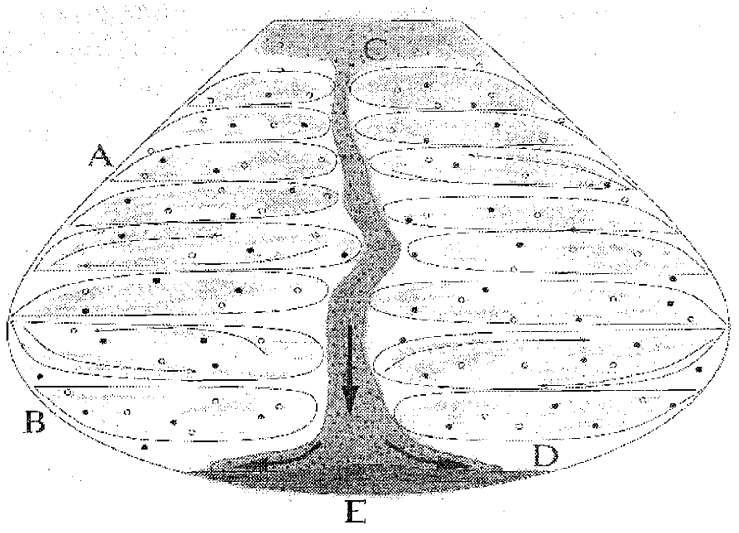

Figure 5-17: The stratified Boycott effect may form convecting layers in magma chambers. As the top layer cools, crystals may form and sink to the bottom, resulting in a particle-laden gravity current that spreads and deposits a layer of crystals at the base of the chamber. Repetition of this process may yield a layered deposit corresponding to the strata observed in solidified magma chambers.

equation (5.17) that $t_d/t_s \sim 10^5$; consequently, the Boycott effect is expected to operate within magma chambers. For a chamber height of 100m, if the density varies by 5% about a mean density of 2500kg/m^3, the resulting density gradient is $d\rho/dy = (0.05 \cdot 2500\text{kgm}^{-3})/100\text{m} = 1.25\text{kg/m}^4$. The particle weight fraction for magma containing 1% of crystals is approximately $0.01 \cdot 500\text{kg/m}^3 = 5\text{kg/m}^3$. Using equation (5.9), this yields a typical convecting layer size of about 4m. Given the broad range of particle concentrations and density gradients, however, this layer size could conceivably vary from 1m to 1km. Equation (5.3) yields a timescale of layer development $t = H/v$ of the order of one month; however, the wide range of particle sizes and viscosities allows for this timescale to vary from days to years. Finally, we note that crystallisation in the bulk will continually drive the Boycott effect and thus maintain the convecting layers.

5.7.3 Discussion

Magma chambers marked by the stratified Boycott effect may leave layered deposits such as those found in field observations via two distinct mechanisms. The chamber can solidify as a whole, the layered rock structure thus being a record of the succession of frozen convecting cells either driven by crystals (A in figure 5.7.2) or bubbles (B). Alternatively the presence of convecting layers could generate layered deposits at the base of the chamber. Since each layer acts as a well–mixed convecting cell, one expects it to maintain a relatively uniform temperature within. The crystallisation of an appreciable quantity of magma may occur when the temperature in the upper,

and therefore coolest, layer falls below a critical value, (C); the resulting crystals would then sink and spread as a gravity current, depositing a layer of crystals (D). The thickness of this deposit is expected to be smaller than that of the convecting layers in the bulk of the chamber (and determined by the volume fraction of particles that settle out), consistent with observations of layers having a thickness of order 20cm (Hodson 1998). The repetition of this process, through the crystallisation of successive layers, then leads to a layered accumulation at the bottom of the chamber (E). According to this physical picture, the layers observed within the solidified chambers are a signature of the cooling of successive layers within the chamber.

Our discussion of the Boycott effect has focused on the physical picture appropriate for monodisperse suspensions, but crystals and bubbles in a magma chamber are likely to be of various sizes. The influence of polydispersity on the Boycott effect was examined by Schaflinger (1985) and the dynamics of the flow are qualitatively unchanged; the layer formation mechanism is therefore not likely to be influenced by polydispersity. However, the simultaneous presence of volatiles and crystals in a magma chamber could lead to the formation of two Boycott layers, as shown in figure 5-16. Both of these Boycott layers may generate convective motions in a stratified ambient, which would then interact in the body of the chamber. The Boycott layer with the largest volume flux is then expected to dominate and prescribe the vertical extent of the horizontal layers.

Chapter 6

Hindered settling in a stratified ambient

6.1 Introduction

The locally averaged settling speed, u_s, of small Reynolds number spherical particles, $Re_p = u_s a/\nu \ll 1$, is typically written as

$$u_s = f(\phi)U_s = f(\phi)\frac{2a^2 g(\rho_p - \rho_f)}{9\nu\rho_f}, \tag{6.1}$$

where U_s is the Stokes settling speed of a single particle in an unbounded ambient, ϕ the particle volume fraction, a the particle radius, ν the kinematic viscosity, g the gravitational acceleration and ρ_p and ρ_f the particle and fluid densities respectively (Batchelor 1967). The presence of neighbouring particles generates a fluid reflux which acts to reduce the settling speed of an individual particle, i.e. $f(\phi) \leq 1$ and $f'(\phi) < 0$ (Richardson & Zaki 1954). The influence of hindered settling on the evolution of a suspension was investigated by (Kynch 1952). The derivative of the particle flux

$$V(\phi) = \frac{d}{d\phi}(\phi f(\phi)) \tag{6.2}$$

was found to be a determinant factor in the qualitative behaviour of the system. Starting from an initial particle concentration jump, one of two things may happen: if $dV(\phi)/dz < 0$, the two regions of different concentration move away from each other and are joined by an expansion fan, an intermediate region where ϕ varies continuously. However, if $dV(\phi)/dz > 0$, the concentration jump remains sharp and propagates as a shock. Concentration jumps may also form from continuous initial particle distributions if $dV(\phi)/dz$ becomes infinite.

The settling speed of particles may change significantly over the course of the sedimenting process. Almost all the components of equation (6.1) (namely a, ρ_f, ν, g) may vary as particles settle. The presence of a density gradient will modify the buoyancy of the particles as they settle, as could be the case for microorganisms settling in the ocean (Pedley & Kessler 1992). Crystals settling in magma chambers

may see their settling speed change owing to vertical viscosity gradients (Hodson 1998) or variations in their own size as melting or crystallisation occurs (Cashman 1993). Centrifugation of particles provides an example where the body force on the particles changes during the settling process (Essington, Mattingod & Ervin 1985). In this chapter, we elucidate the combined influence of inhomogeneities in the suspending fluid and hindered settling effects on the time evolution of the particle concentration of a suspension.

We focus on settling speed variations due to a stable density gradient. As particles settle, the density difference between particles and the ambient diminishes, causing a reduction in settling speed. As a measure of the magnitude of the settling speed variation, we consider the relative velocity variation $\gamma = (u_h - u_0)/u_0$, where u_h and u_0 are respectively the settling speed at the top and bottom of the suspension. When settling speed variations arise only from density gradients, γ reduces to

$$\gamma = \frac{\rho_0 - \rho_h}{\rho_p - \rho_0}, \tag{6.3}$$

with ρ_h and ρ_0 the density at the top and bottom of the suspension, respectively. Particles having a density close to that of the ambient fluid are thus subject to larger relative velocity variations.

The influence of a density gradient on the settling speed of a single particle was studied by Oster & Yamamoto (1963), who demonstrated that the settling speed adjusts to the surrounding conditions on a time scale $t_{adj} \sim a^2/\nu$. The ratio of the adjustment time to the time required for a particle to settle a distance equal to its radius, $t_s = a/U_s$, is thus equal to the particle Reynolds number, $Re_p = U_s a/\nu$. We here focus our attention on particles with $Re_p \ll 1$, which allows us to assume that the settling speed adjusts instantaneously and thus depends only on local parameters.

The combination of density gradients and particle concentration gradients may give rise to large scale fluid motions. Instabilities may develop if a region of high particle concentration overlies a particle–depleted region. Details of the instability of a region of high sand concentration settling above a clear fluid region in a vertical Hele-Shaw cell were recently investigated by Völtz, Pesch & Rehberg (2001) and many similarities with a classic Rayleigh-Taylor instability were observed. A similar instability may result from particles settling through a density jump. If a particle–laden fluid overlies a heavier, particle–free fluid, the initial density profile may be stable. However, as particles settle across the density interface, they form a region of high concentration above a particle–free region. The resulting three–layer system may then become unstable and the form of the resulting instabilities have been examined by Hoyal, Bursik & Atkinson (1999) and Parsons, Bush & Syvitski (2001). We consider similar systems where instabilities may result from particle concentration variations caused by the presence of an ambient stratification.

In this chapter, we first review the results of Kynch (1952) in §6.2 before extending them to the case of an inhomogeneous ambient in §6.3. The stability of the resulting motion is discussed in §6.4 and §6.5 is concerned with the experimental verification of these results for a suspension of latex particles settling in a density gradient.

6.2 Hindered settling

We begin by considering the effects of particle–particle interactions on the time evolution of the particle concentration in a homogeneous ambient. Because the settling speed decreases with increasing particle concentration, a front of particles settling above a particle–free region will be quickly eroded as particles ahead of the front settle faster than those behind it. Conversely, the interface between particle–free and particle–laden regions above a suspension will remain sharp as particles above the interface fall faster than those in the bulk of the suspension. We proceed to quantify the influence of hindered settling following the approach of Kynch (1952).

We consider the equation of conservation of particles

$$\partial_t \phi - \partial_z (u_s \phi) = 0. \tag{6.4}$$

Here t denotes time and z height, taken to be increasing upwards. The relative importance of particle settling and particle diffusion is prescribed by the Péclet number $Pe = u_s h/\kappa_\phi$, with κ_ϕ the diffusion coefficient of particles and h the height of the container. We consider the large Péclet number limit in which particle diffusion may be neglected. We consider that the settling speed and concentration are uniform in any horizontal plane so that we may restrict ourselves to one spatial dimension. The development of instabilities that violate this condition will be considered in §6.4. We suppose the settling speed to be of the form (6.1), assuming that only local parameters have an impact on the settling speed. We consider monodisperse suspensions: a and ρ_p, are the same for all particles. For the moment we restrict our attention to homogeneous ambients, so that u_s depends exclusively on ϕ.

We may then rewrite (6.4) as

$$\partial_t \phi - U_s V(\phi) \partial_z \phi = 0. \tag{6.5}$$

Using the method of characteristics (e.g. Debnath 1997), it may be seen that the concentration of particles remains constant along straight lines described by

$$\frac{dz}{dt} = -U_s V(\phi). \tag{6.6}$$

Note that for small values of ϕ, approximately below 15%, $f(\phi)$ is nearly one and varies slowly so that $V(\phi)$ is positive and decreasing (Richardson & Zaki 1954). Given the initial particle concentration, one may thus follow along characteristics and deduce the concentration at later times.

Two notable complications may occur. The first one results from divergent characteristics. If a discontinuity in ϕ exists at height M and is such that the concentration above, ϕ_2, yields characteristics with slope larger than the concentration below, ϕ_1,

$$-U_s V(\phi_2) \geq -U_s V(\phi_1) \tag{6.7}$$

then there is a region of the zt–plane through which no characteristics pass, see figure

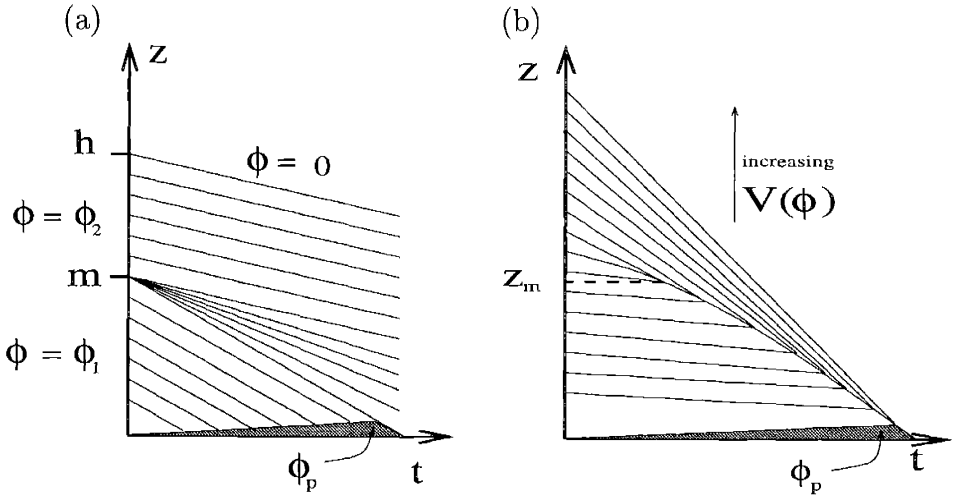

Figure 6-1: The evolution of particle concentration in a homogeneous ambient. a) Formation of an expansion fan from an initial discontinuity in particle concentration. Here $V(\phi_2) < V(\phi_1)$, where $V(\phi)$ is define in (6.2), so that characteristics travel faster in the underlying region $z < m$. b) Formation of a shock from a continuous initial distribution. Here $V(\phi)$ increases with z. The bottom region shows the accumulation of particles at their packing concentration, ϕ_p.

6-1a. The discontinuity at M should then be replaced by a linear interpolation such that $\phi(M+\epsilon) = \phi_2$ and $\phi(M-\epsilon) = \phi_1$. The problem is then well–posed and a unique solution is found following characteristics. Taking the limit $\epsilon \to 0$ recovers the case of a discontinuity as illustrated in figure 6-1b. The concentration at any point (z,t) in the expansion fan, $\phi_f(z,t)$, thus satisfies

$$z - M = -U_s V(\phi_f) t. \tag{6.8}$$

If characteristics are converging, particle concentration discontinuities will form. When two characteristics meet, the concentration of particles cannot be found through the use of equation (6.5) alone. Because the concentration becomes discontinuous, a discrete form of equation (6.4) is needed to track the progression of the shock. Labeling the region above the shock with index a and the region below with index b, conservation of particles then requires

$$\phi_a(U_s f(\phi_a) + U_j) = \phi_b(U_s f(\phi_b) + U_j) \tag{6.9}$$

where U_j is the propagation speed of the jump in particle concentration. The shock thus moves through the suspension with speed

$$U_j = -U_s \frac{\phi_b f(\phi_b) - \phi_a f(\phi_a)}{\phi_b - \phi_a} \tag{6.10}$$

provided $V(\phi_a) > V(\phi_b)$; otherwise, no shocks form. In particular, if there are no par-

ticles in the above region, $\phi_a = 0$, the jump is simply seen to propagate with velocity $U_j = -U_s f(\phi_b)$. If the initial concentration is continuous but such that characteristics meet, the time-evolution of the concentration is found following characteristics until they reach a shock, as shown in figure 6-1b. It may be seen that the first characteristics to meet originate from points infinitesimally close, which we denote z_0 and $z_0 + \epsilon$, with $\epsilon \to 0$. Denoting the initial particle distribution by $\phi_0(z)$, the time at which characteristics intersect, t, satisfies

$$z_0 - U_s V(\phi_0(z_0))t = z_0 + \epsilon - U_s V(\phi_0(z_0 + \epsilon)) \tag{6.11}$$

Taking the limit $\epsilon \to 0$ and solving for t yields

$$t = \frac{1}{U_s} \frac{1}{\frac{dV(\phi_0)}{dz}|_{z_0}} \tag{6.12}$$

The first occurrence of a shock is thus found by minimising the above expression. Denoting the maximum of $dV(\phi_0)/dz$ by z_m, the point at which characteristics first cross has coordinates

$$t_j = \frac{1}{U_s} \frac{1}{\frac{dV(\phi_0)}{dz}|_{z_m}} \qquad \text{and} \qquad z_j = z_m - \frac{V(\phi_0(z_m))}{\frac{dV(\phi_0)}{dz}|_{z_m}} \tag{6.13}$$

At later times, the shock progresses with speed U_j (equation (6.10)).

As particles reach the bottom of the container, their concentration reaches a maximum that will be approximately equal to the solid packing concentration ($\phi_p \approx 65\%$) (Torquato & Truskett 2000). The bottom of the container is thus a source of characteristics of slope $-U_s V(\phi_p)$. Note that these lines are expected to have a positive slope to account for the accumulation of particles at the bottom. Similarly, characteristics of slope $-U_s V(0)$ originate from the top of the suspension if no new particles are introduced. In a homogeneous ambient, these upper and lower boundary conditions are sufficient to track the evolution of ϕ.

6.3 Stratified ambient

We now allow the density of the fluid ρ_f to be a function of z, so that the settling speed U_s also depends on height. We consider low particle concentrations ($\phi \ll 1$) so that the fluid reflux is weak ($U_{ref} \sim u_s \phi$). The upward motion of the ambient stratification resulting from the accumulation of particles at the bottom of the container may thus be neglected. We thus have that $U_s(z)$ is time independent and we may thus rewrite equation (6.4) as

$$\partial_t \phi - U_s \, V(\phi) \partial_z \phi = \phi f(\phi) \partial_z U_s \tag{6.14}$$

Using the method of characteristics, we obtain the following system of equations

$$dt = -\frac{1}{U_s} \frac{dz}{V(\phi)} = \frac{d\phi}{\phi f(\phi) \partial_z U_s} \tag{6.15}$$

This system cannot be solved in general but special cases may be investigated in detail.

6.3.1 Neglecting Particle–Particle Interactions

We first consider the case of very low particle concentration so that hindered settling is of negligible importance, but allow the settling speed to vary with height. Taking $f(\phi) = 1$, the system (6.15) reduces to

$$dt = -\frac{dz}{U_s} = \frac{d\phi}{\phi \partial_z U_s}, \tag{6.16}$$

which has a general solution of the form

$$\phi(z,t) = \frac{1}{U_s} F\left(t + \int_0^z \frac{dz'}{U_s}\right) \tag{6.17}$$

where $F(\eta)$ is an unspecified function to be determined from initial conditions.

If we consider the case of a linear density gradient, the settling speed is of the form $U_s(z) = (u_0 + \Gamma z)$, where the velocity gradient is $\Gamma = (u_h - u_0)/h$. The top interface propagates downward from the initial position $z_i(0) = h$ with speed U_s, from which we find $z_i(t) = (u_h e^{-\Gamma t} - u_0)/\Gamma$. If the initial concentration is uniform, $\phi(z,0) = \phi_i$, the complete solution is

$$\begin{aligned} \phi(z,t) &= \phi_i e^{\Gamma t} && \text{if } z < z_i(t) \\ &= 0 && \text{otherwise} \end{aligned} \tag{6.18}$$

The concentration is thus seen to increase with time uniformly within the suspension. Note that the concentration remains uniform in space because of the assumed linear density gradient and would vary with height for other forms of $U_s(z)$. The concentration of particles increases exponentially in time. When expressed in terms of the height of the suspension, z_i, the concentration obeys

$$\phi(z_i) = \phi_i \frac{u_0 + \Gamma h}{u_0 + \Gamma z_i} \tag{6.19}$$

6.3.2 Including hindered settling

We now include the effects of hindered settling and assume the settling speed to be of the form $u_s(z,\phi) = f(\phi)(u_0 + \Gamma z)$. The system (6.14) then takes the form

$$dt = -\frac{dz}{(u_0 + \Gamma z)V(\phi)} = \frac{1}{\Gamma}\frac{d\phi}{f(\phi)\phi} \tag{6.20}$$

Solving for the first and third terms we find

$$K_1 = P(\phi) - \Gamma t \tag{6.21}$$

and for the second and third terms

$$K_2 = \phi f(\phi) U_s \tag{6.22}$$

where we define $P(\phi) = \int_{1/2}^{\phi} dc/(cf(c))$. Since K_1 is in effect dependent on K_2, the general solution is

$$\Gamma t = P(\phi) + F(U_s \phi f(\phi)) \tag{6.23}$$

This solution may only be expressed implicitly, but simple initial conditions yield explicit expressions.

We first consider a step-function as an initial condition: $\phi = \phi_1$ if $0 < z < m$, $\phi = \phi_2$ if $m < z < h$ and $\phi = 0$ otherwise, as shown in figure 6-1a. Note that the characteristics are still described by $dz/dt = -(u_0 + \Gamma z)V(\phi)$. For general ϕ_1, ϕ_2 the solution is

$$\begin{aligned} \phi(z,t) &= P^{-1}(\Gamma t + P(\phi_1)) \qquad \text{if } 0 < [\frac{\phi f(\phi)}{\phi_1 f(\phi_1)}(u_0 + \Gamma z) - u_0]\frac{1}{\Gamma} < m \\ &= P^{-1}(\Gamma t + P(\phi_2)) \qquad \text{if } m < [\frac{\phi f(\phi)}{\phi_2 f(\phi_2)}(u_0 + \Gamma z) - u_0]\frac{1}{\Gamma} < h \end{aligned} \tag{6.24}$$

We consider the function $V(\phi)$ to be decreasing with ϕ, a dependence that has been verified experimentally for low particle concentrations ($\phi < 15\%$) by Richardson & Zaki (1954). If $\phi_1 < \phi_2$, the regions of concentration $P^{-1}(\Gamma t + P(\phi_1))$ and $P^{-1}(\Gamma t + P(\phi_2))$ drift apart and are joined by an expansion fan. For any point (z,t) in that region, the concentration is given by $P^{-1}(\Gamma t + P(\phi_m))$, where ϕ_m satisfies

$$m = \frac{1}{\Gamma}\left[\frac{P^{-1}(\Gamma t + P(\phi_m)) f(P^{-1}(\Gamma t + P(\phi_m)))}{\phi_m f(\phi_m)}(u_0 + \Gamma z) - u_0\right]. \tag{6.25}$$

Because $dV(\phi)/d\phi < 0$, we must have that $\phi_1 < \phi_m < \phi_2$; the concentration of the suspension may thus be determined everywhere. Using the Richardson-Zaki formula, $f(\phi) = (1-\phi)^{5.1}$, the concentration evolution may be computed numerically. Figure 6-2 illustrates the evolution of a suspension settling in a stable linearly stratified ambient; initial particle concentrations are $\phi_1 = 0.01$ and $\phi_2 = 0.03$ respectively above and below $z = 20$cm. The position of the top interface z_i may be found by integrating

$$\frac{dz_i}{dt} = f(\phi)(u_0 + \Gamma z_i) \tag{6.26}$$

with the initial condition $z_i(0) = h$.

If $\phi_1 > \phi_2$, the two regions described by equation (6.24) will overlap, leading to the formation of a shock across which the concentration changes abruptly. The presence of a discontinuity again forces the use of a discrete statement of particle conservation. If we denote the downward speed of the shock as U_j, and the concentration above and below the shock respectively as ϕ_a and ϕ_b, we find that the jump propagates with

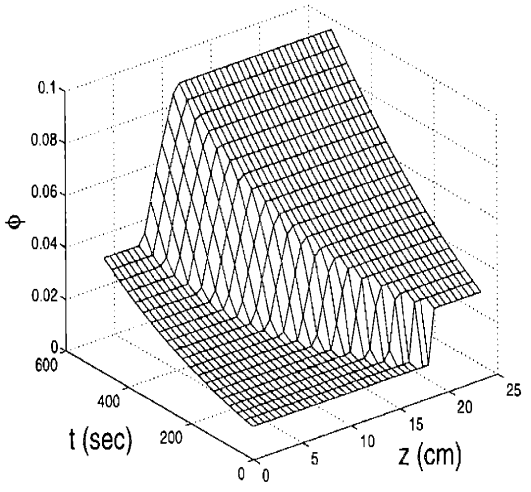

Figure 6-2: Theoretical predictions of the progression of an initial concentration jump of particles of radius 50μm and density 1.19g/cc settling in a stable linear density gradient with density 1g/cc at the top and 1.18g/cc at the bottom. Initial particle concentrations are $\phi_1 = 0.01$ below $z = 20$cm and $\phi_2 = 0.03$ above $z = 20$cm. Characteristics are divergent, leading to the formation of an expansion fan.

speed

$$\frac{dz_j}{dt} = U_j(z,t) = U_s(z)\frac{\phi_b f(\phi_b) - \phi_a f(\phi_a)}{\phi_b - \phi_a} \tag{6.27}$$

The position of the shock, z_j, may thus be obtained by integrating this equation in time. The position of the top interface is given, as previously, by equation (6.26). Using the Richardson-Zaki formula (1.14) allows for the numerical computation of the time evolution of the particle concentration. Figure 6-3 shows the evolution of a particle jump settling in a linear stratification, with initial concentrations $\phi_1 = 0.03$ and $\phi_2 = 0.01$, respectively, below and above $z = 12$cm. Note that in the case $dV(\phi)/d\phi > 0$, corresponding to $\phi > 15\%$, the solution given in (6.24) may be applied by interchanging the values of ϕ_1 and ϕ_2.

In general, the function $V(\phi)$ need not be monotonous. Around a local minimum of $V(\phi)$ corresponding to an inflection point in the flux function $\phi f(\phi)$, both an expansion fan and a shock will form. Consider a case where $\phi_1 < \phi_2$ and $V(\phi_1) > V(\phi_2)$ but V has a local minimum between ϕ_1 and ϕ_2, a simple expansion fan is not a solution since characteristics would travel slower in the expansion fan than in the upper region. The concentration then increases from $P^{-1}(\Gamma t + P(\phi_1))$ continuously up to an intermediate value, ϕ_s, at which point it jumps to $P^{-1}(\Gamma t + P(\phi_2))$. The concentration ϕ_s is such that the shock travels exactly at the same speed as the characteristics associated with ϕ_s

$$\frac{\phi_s f(\phi_s) - P^{-1}(\Gamma t + P(\phi_2)) f(P^{-1}(\Gamma t + P(\phi_2)))}{\phi_s - P^{-1}(\Gamma t + P(\phi_2))} = V(\phi_s). \tag{6.28}$$

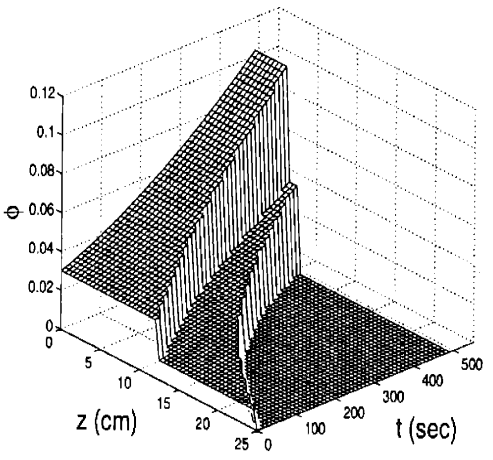

Figure 6-3: Theoretical prediction for the progression of a concentration jump of particles of radius 50μm and density 1.19g/cc settling in a stable linear density gradient with density 1g/cc at the top and 1.18g/cc at the bottom. Initial concentrations are $\phi_1 = 0.03$ below $z = 12cm$ and $\phi_2 = 0.01$ above $z = 20$cm. Characteristics are convergent, thus the concentration jump remains sharp. The rate of descent of the upper interface and concentration jump are notably different.

as may be seen in figure 6-4. As particles settle, the ambient fluid density becomes larger and the concentrations increase. Eventually, $P^{-1}(\Gamma t + P(\phi_1))$ exceeds the concentration corresponding to a minimum of $V(\phi)$, and only a shock remains. A similar scenario may arise in the vicinity of a maximum of $V(\phi)$, with the values of ϕ_1 and ϕ_2 inverted.

If the settling speed depends on height in a non–linear fashion, we may still compute numerically the time evolution of the particle concentration, and the positions of the top interface and concentration jumps. Starting from a uniform initial particle concentration and using the Richardson-Zaki formula (1.14), ϕ may be computed as a function of time by solving numerically equations (6.15). Following along characteristics given by $dz/dt = -U_s[\phi(1-\phi)^{5.1}]'$, the quantity $K_2 = U_s\phi(1-\phi)^{5.1}$ remains constant, which allows us to find ϕ everywhere. In the presence of a stable ambient stratification, the concentration of particles increases with time, thus enhancing the influence of hindered settling. The speed of the top interface obeys equation (6.26), and so

$$\frac{dz_i}{dt} = -U_s(z_i)[1-\phi(z_i,t)]^{5.1}, \tag{6.29}$$

which may be integrated, using $z_i(0) = h$, to yield its position as a function of time. The evolution of an initial concentration jump may also be computed numerically. We consider the case where the concentration above the shock, ϕ_a, is less than that below the shock, ϕ_b, so that the settling process remains stable. If in addition the concentration of particles is everywhere smaller than 15%, the concentration jump remains sharp and the velocity of the shock is given by equation (6.10). Making use

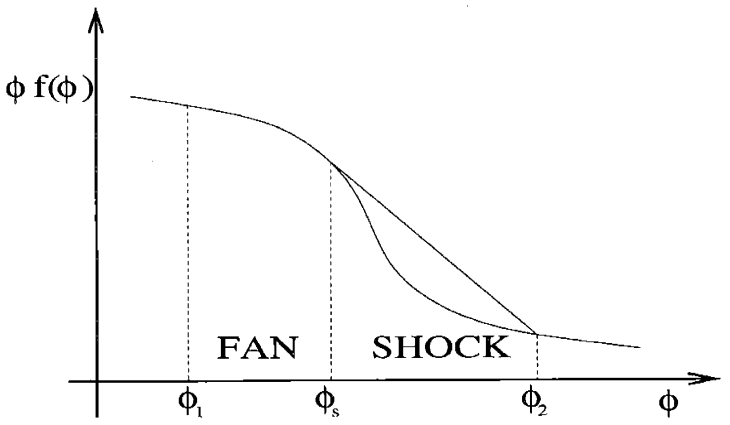

Figure 6-4: In the vicinity of a local minimum of the characteristics slope $V(\phi) = [\phi f(\phi)]'$, corresponding to an inflection point of the flux $\phi f(\phi)$, both an expansion fan and a shock may form. The transition occurs at a point ϕ_s where characteristics propagates at the same speed as the shock between ϕ_s and ϕ_2. If particles settle in a stably stratified ambient, the concentrations increase with time and eventually the concentration in the bottom region $P^{-1}(\Gamma t + P(\phi_1))$ exceeds the minimum of $V(\phi)$ and only a shock remains.

of the Richardson-Zaki formula and computing the concentrations of the bottom and top regions as in the case of a uniform initial ambient, we may track the position of the concentration jump as a function of time.

6.4 Convective instabilities

We consider a physical system where an initial particle concentration $\phi_i(z)$ settles in a fluid whose density increases with depth $d\rho_f/dz < 0$. If the particles are denser than the ambient fluid, $\rho_p > \rho_f$, a region of high particle concentration overlying a particle–depleted region has a statically unstable density gradient, and so may give rise to large–scale convective overturning. We derive in this section criteria describing when an unstable density gradient is formed by particles settling in a stably stratified ambient; both discrete and continuous stratifications are considered.

A simple criterion may be obtained for the formation of an unstable density profile from sedimentation across a stable density jump. Consider a fluid of density ρ_t containing an initial particle concentration ϕ_t overlying a fluid of density ρ_b and particle concentration ϕ_i (see figure 6-5). Conservation of particle flux across the interface requires that the concentration of particles having settled through the density jump, ϕ_b, be given by

$$\phi_b f(\phi_b) = \frac{\phi_t f(\phi_t)(\rho_p - \rho_t)}{(\rho_p - \rho_b)}. \tag{6.30}$$

If $\phi_b > \phi_i$, the resulting density profile is statically unstable. In particular, if the concentration above and below the density jump are initially equal, $\phi_t = \phi_b$, the

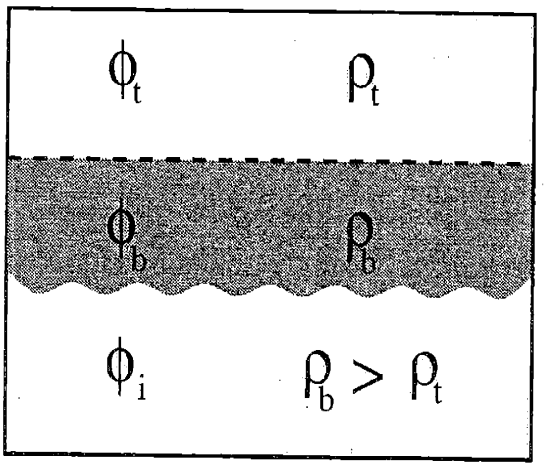

Figure 6-5: If particles settle through an ambient density jump, $\phi_t < \phi_b$, instabilities may develop if the concentration below the jump, is greater than the initial concentration in the bottom region $\phi_b > \phi_i$.

bottom region will become statically unstable owing to the development of a high concentration particle layer in its upper extremities.

We now turn our attention to systems where particles settle in a continuous, stable stratification. For example, consider a uniform concentration of particles settling in a stable density gradient overlying a region of constant density (but with no density jump). The concentration of particles increases in the stably stratified region but remains constant in the region of constant density. As particles settle, a region of high particle concentration forms at the top of the layer of constant density and the resulting density profile is unstable. Hindered settling facilitates the formation of such instabilities by further increasing the concentration of particles in the stratified layer. We wish to characterise initial conditions under which a stable initial particle concentration may generate an unstable density profile. In the following argument, we neglect hindered settling in order to obtain a simpler criterion which is valid to order ϕ, but neglects terms of order ϕ^2. A similar derivation including hindered settling effects may be done by the same reasoning but would require the use of cumbersome notation.

We begin by recalling that, in the absence of hindered settling, the quantity $K_2 = U_s\phi$ is constant along characteristics of slope $dz/dt = -U_s(z)$. We define a function $a(z) = \int_0^z (U_s(z'))^{-1}dz'$ such that characteristics passing through a point (z,t) originate from the point $(z_0, 0)$, with

$$z_0 = a^{-1}(a(z) + t). \tag{6.31}$$

The concentration of particles at any point (z,t) below the top interface is then

$$\phi(z,t) = \frac{U_s(z_0)\phi_i(z_0)}{U_s(z)} = \frac{U_s(a^{-1}(a(z)+t))\phi_i(a^{-1}(a(z)+t))}{U_s(z)} \tag{6.32}$$

where ϕ_i is the initial particle concentration.

Because the settling speed changes only owing to variations in the ambient fluid density, $\rho_f(z)$, we have

$$\frac{U_s(z_0)}{U_s(z)} = \frac{\rho_p - \rho_f(z_0)}{\rho_p - \rho_f(z)}. \tag{6.33}$$

The total density of the suspension then becomes, using (6.32) and (6.33),

$$\rho(z,t) = \rho_f(z) + \phi_i(z_0)(\rho_p - \rho_f(z_0)). \tag{6.34}$$

Using the definition of $a(z)$ and equation (6.31) we find the derivative of the total density to be

$$\left.\frac{d\rho}{dz}\right|_z = \left.\frac{d\rho_f}{dz}\right|_z + \frac{\rho_p - \rho_f(z_0)}{\rho_p - \rho_f(z)} \left((\rho_p - \rho_f(z_0)) \left.\frac{d\phi_i}{dz}\right|_{z_0} - \phi_i(z_0) \left.\frac{d\rho_f}{dz}\right|_{z_0} \right) \tag{6.35}$$

A simple result may be found if we further assume that the initial concentration of particles is uniform. We then find that an unstable density profile, $d\rho/dz > 0$, is formed if

$$\left.\frac{d\rho_f}{dz}\right|_z > \phi_i(z_0) \left(\frac{\rho_p - \rho_f(z_0)}{\rho_p - \rho_f(z)} \right) \left.\frac{d\rho_f}{dz}\right|_{z_0} \tag{6.36}$$

where it should be noted that the derivative of ρ_f with respect to z is everywhere negative (or zero). For a given z, $z_0(t)$ ranges over all values such that $z_0 > z$. In particular, if the density gradient vanishes ($d\rho_f/dz = 0$) beneath a stratified region, particle settling will always result in a statically unstable density profile. This criterion also indicates that if the fluid density gradient increases with depth ($d^2\rho_f/dz^2 > 0$) then no statically unstable profile may develop due to particle settling. We note that larger particle concentrations will more readily generate unstable density profiles, which is to be expected since particles act as the destabilising agent. Also, this criterion will always be satisfied if the fluid density tends to a constant for large depths, $d\rho_f/dz \to 0$ for $z \to -\infty$.

The formation of a statically unstable density profile does not necessarily lead to large–scale convective overturning. The analogy with the Rayleigh-Bénard instability serves to show that viscous effects may be sufficiently strong to suppress dynamical instabilities, as was observed when very low particle concentrations settling across a density jump remained stable (Parsons *et al.* 2001). The size of the unstable region, $d(t)$, typically grows as particle settle and we may then define a time–dependent Rayleigh number

$$Ra = \frac{g\Delta\rho d^3}{\rho\kappa_\phi\nu} \tag{6.37}$$

where $\Delta\rho$ is the density difference across the unstable region and κ_ϕ the diffusivity of particles. If the unstable region becomes sufficiently large, the Rayleigh number exceeds a critical value above which convective motions are observed. The onset of instability may thus be considerably delayed before the unstable region reaches its critical size. Another stabilising factor is the downward propagation of the unstable

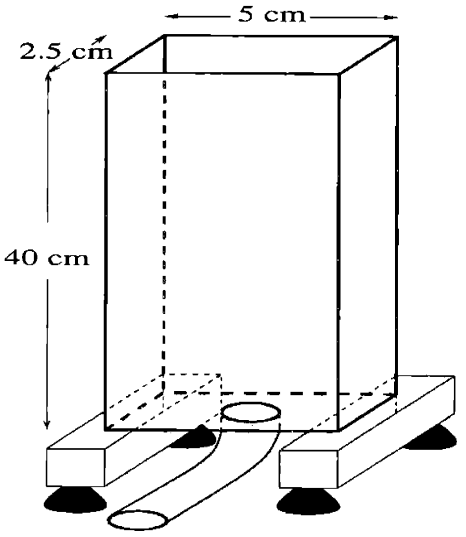

Figure 6-6: A schematic illustration of the apparatus used in our experimental study. The tank is filled from below via the Oster double–bucket technique to obtain a stably stratified ambient with either a suspension of uniform concentration or a particle concentration jump.

region, as was discussed in chapter 4; the value of the critical Rayleigh number increases almost linearly with the particle settling speed. Larger particles thus require a larger particle concentration difference across the unstable region before becoming unstable.

6.5 Experiments

A series of experiments were conducted in order to investigate the evolution of a suspension settling in a stably stratified ambient. Particular attention was given to tracking the position of the top interface and examining the stability of the resulting motion. The experimental apparatus, shown schematically in figure 6-6, consists of a Plexiglas tank 40cm high, 5cm wide and 2.5cm thick. Vibration control mounts isolated the container from mechanical disturbances and were used to level the system and so ensured that no Boycott effect was present (Boycott 1920). Bangs Labs polymer beads of density 1.19g/cc and radius $49\pm8\mu$m were used and the smallest particles present, with radius 41μm, determined the progression of the top interface. Salt water was used as a suspending fluid and linear density gradients were generated via the Oster double–bucket technique (Oster 1965). Non–linear density gradients were generated by varying the flow rates between the two buckets. The container was filled from below with progressively heavier fluid. The filling process took approximately one minute, in which time particles settled less than 2cm. Precise measurements of the density profile were performed using a PME salinity probe calibrated using an Anton Parr DMA 35 densitometer. The salinity variations also

prompted viscosity variations of the salt water solution of up to 50% (Handbook of Chemistry and Physics 1986). From the density and viscosity profile so deduced, we could evaluate the settling speed as a function of height using equation (6.1). The settling speed typically varied by a factor of $\gamma = 2$ over the depth of the tank.

Two distinct initial particle distributions were considered. To produce an initially uniform distribution of particles, an equal volume fraction of particles were added to each of the two source buckets used for filling. To produce a system marked by an initial particle concentration jump, a given volume fraction of particles was initially present in each source bucket; at the appropriate time, particles were added simultaneously to both buckets so that the concentration increased abruptly and remained constant thereafter.

The time evolution of concentration jumps and the top interface were measured from video recordings. The camera was located 4m away from the container in order to eliminate parallax effects. The position of the top interface was defined as the position where the reflected light intensity increased abruptly from a value corresponding to particle–free fluid to that of the suspension. Similarly, the position of a jump in particle concentration was defined as the position where the light intensity changed abruptly. Qualitative observations of the particle concentration were deduced by measuring the intensity of the reflected light using Digimage software (Dalziel 1993) Images of the development of instabilities were captured using Digimage and contrasts were enhanced using Matlab.

6.5.1 Time evolution of the top interface

Figure 6-7 shows the progression of the top interface in the presence of relatively (a) weak and (b) strong stratifications. The stars indicate experimental measurements while the solid line was computed via equation (6.29). Computations deduced through the neglect of hindered settling are also plotted as the dashed line for the sake of comparison. In both experiments, the initial particle concentration is 1.5%. In the case $\gamma = 0.4$ (figure 6-7a), the ambient stratification is predicted to cause the particle concentration to increase to 2.2% by the time the suspension is completely settled out. Although no quantitative measurements could be made of the particle concentration, variations in the reflected light intensity indicated that ϕ increased appreciably as the particles settled. For small values of γ, the total settling time may be predicted to within an error of approximately 5% by neglecting hindered settling. Moreover, because the settling speed of the particles only varies by a factor of 0.4, the progression of the top interface is nearly linear.

In the strong stratification case $\gamma = 3.1$ (figure 6-7b) the presence of the ambient stratification greatly affects the sedimentation process. The concentration is predicted to increase from 1.5% to approximately 5.9% by the time the interface reaches the bottom of the container. In order to predict accurately the progression of the interface, the effects of both hindered settling and of the ambient stratification must be taken into account, as may be seen from the relatively large error (20%) obtained by neglecting hindered settling. The theoretical prediction (6.29) is seen to yield good agreement with experimental measurements for both small and large γ.

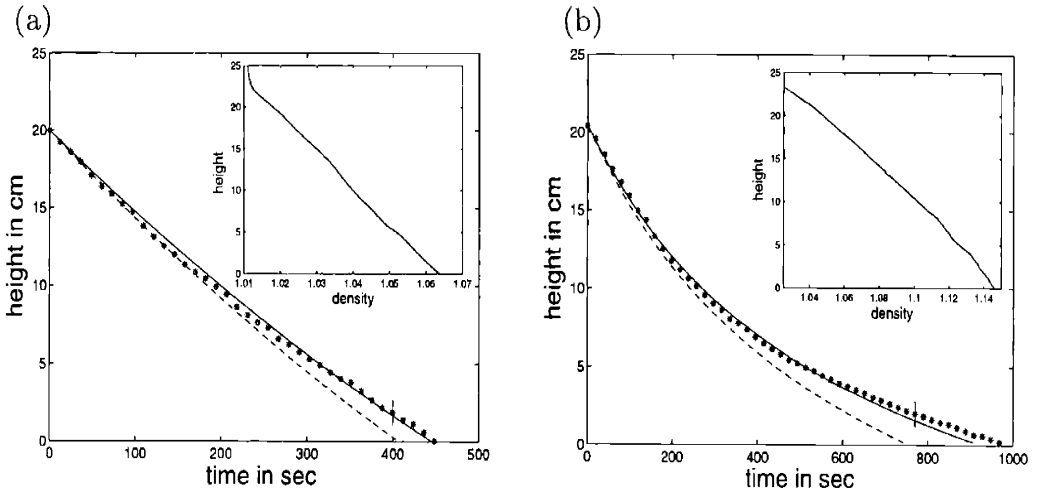

Figure 6-7: Position of the top interface of a suspension with $\phi_i = 1.5\%$ settling in a stratified ambient for (a) weak density gradient, $\gamma = 0.4$ and (b) strong density gradient, $\gamma = 3.1$. The dashed curves correspond to the theoretical predictions (6.19) deduced by neglecting hindered settling and the solid curves are obtained by combining equations (6.15) and (6.26). The stars indicate experimental measurements of the progression of the top interface. A typical error bar is shown. The corresponding density profile is shown on the top right.

6.5.2 Concentration Jump

The progression of a concentration jump in shown in figure 6-8 for particles settling in relatively (a) weak and (b) strong density gradients. In both experiments, initial particle concentrations above and below the interface are, respectively, $\phi_a = 0.5\%$ and $\phi_b = 2.0\%$. The stars indicate experimental measurements and the solid lines the theoretical predictions. Computations made neglecting hindered settling are also plotted as the dashed line for the sake of comparison. The dotted line indicates the observed progression of the top interface. It may be seen in both experiments that the top interface propagates faster than the concentration jump, as one expects on the basis of equation (6.27).

For $\gamma = 1.0$ (figure 6-8a), the ambient stratification is predicted to cause the particle concentrations to increase to $\phi_a = 0.9\%$ and $\phi_b = 4.0\%$ by the time the concentration jump reaches the bottom of the container. As was the case for the top interface, systems with small values of γ are marked by a nearly linear progression of the concentration jump. Qualitative observations of the particle concentration again showed that ϕ increased significantly as settling proceeded. For $\gamma = 2.3$ (figure 6-8b), the progression of the concentration jump is clearly non linear and the final particle concentrations are predicted to be larger, $\phi_a = 1.4\%$ and $\phi_b = 5.9\%$, respectively. Neglecting hindered settling greatly underpredicts the position of the concentration jump as indicated by the dashed curve in figure 6-8b. Experimental results are again well described by the theory of §6.3.

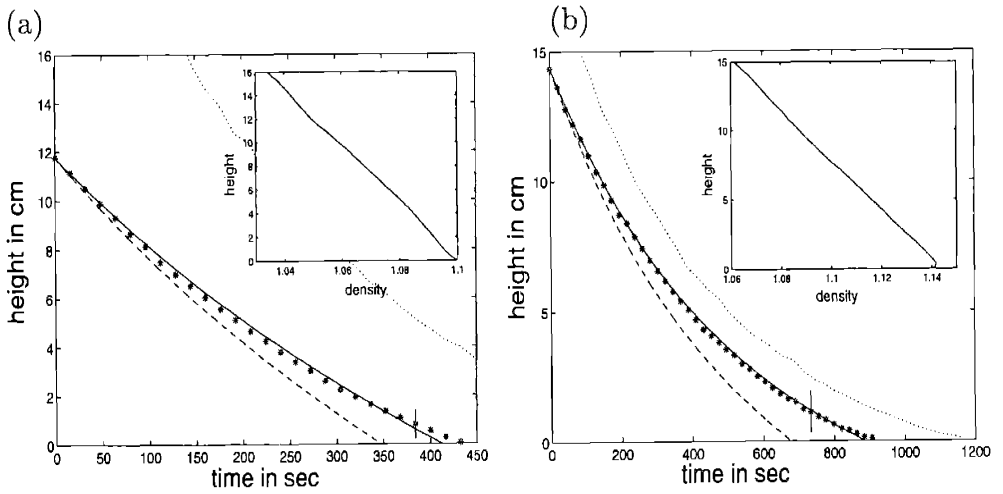

Figure 6-8: Progression of a particle concentration jump with $phi_a = 0.5\%$ and $\phi_b = 2.0\%$ settling in a stably stratified ambient for (a) weak density gradient $\gamma = 1.0$ and (b) strong density gradient $\gamma = 2.3$. The dashed curves corresponding to theoretical predictions deduced by neglecting hindered settling ((6.26 with $f(\phi) = 1$) and the solid curves are obtained by combining equations (6.15) and (6.24). The stars are experimental measurements of the progression of the concentration jump and the dotted line indicates the recorded progression of the top interface. A typical error bar is shown. The corresponding density profile is shown on the top right.

6.5.3 Instability

Our experimental arrangement was such that the criterion (6.36) could only be qualitatively verified. In particular, the precise point where instability first develops is difficult to observe because of the presence of suspended particles both above and below the region of instability. The presence of instabilities was observed through the formation of large scale structures such as plumes and convection rolls that could be observed through variations in the reflected light intensity.

Particles settling in a linear density gradient or in a concave density profile, $d^2\rho_f/dz^2 > 0$, were seen to remain stable: particles settled as individuals without generating any large scale convective motions. However, an initially uniform concentration of particles settling through a density jump was seen to give rise to particle plumes in the bottom region, in accord with previous observations (Hoyal *et al.* 1999, Parsons *et al.* 2001). Uniform initial particle concentrations settling in a stably stratified ambient where the density tends to a constant toward the bottom of the tank also developed instabilities. The observed plumes typically had a characteristic scale of 4mm and velocity of 1cm/s, values consistent with plumes formed through corresponding Rayleigh-Taylor instabilities. Two counter–rotating convective rolls with typical speed 1cm/s could also be observed, showing a vigourous upflow near the center of the container and downflow along the walls. Figure 6-9 summarises the stability characteristics of a number of generic density profiles.

Images were captured of the instability resulting from an initially uniform concentration of particles settling in a stable linear density gradient matching continuously onto an underlying region of constant density. The resulting convective motions are apparent in figures 6-10 and 6-11 (Matlab and Digimage were used to enhance contrasts). The initial and final density profiles are shown in figure 6-10d. The pictures shown in figure 6-10 were taken almost 10 minutes after the filling of the tank, by which time the particle concentration had increased significantly in the stratified region, computations showing that the concentration in the top region should be in excess of 3%.

It may be seen in figure 6-10(a,b,c) that the region of high particle concentration does not progress downward. In the absence of instability, the high ϕ region would have traveled approximately 1.5cm between the times images (a) and (C) were captured. Instead, in the 5 minutes following the apparition of the first particle plumes, the region of high concentration remained stationary and sheds particle plumes into the underlying region. Convection rolls were also observed, transporting particles on a timescale much faster than that of particle settling and ensuring that the lower region was well-mixed. The initial density profile (figure 6-10d) shows a linear ambient density gradient in the region where particles settled as individuals (above $\sim$ 29cm), but a nearly constant density in the region where instabilities developed (below $\sim$ 29cm). This profile indicates that convective instability developed in the region where the density gradient vanished, in agreement with criterion (6.36). Also, the final density profile shows that limited mixing occurred at the top of the region of constant density, but no significant entrainment of fluid from the stably stratified region could be observed. Once instability was initiated, particles were transported

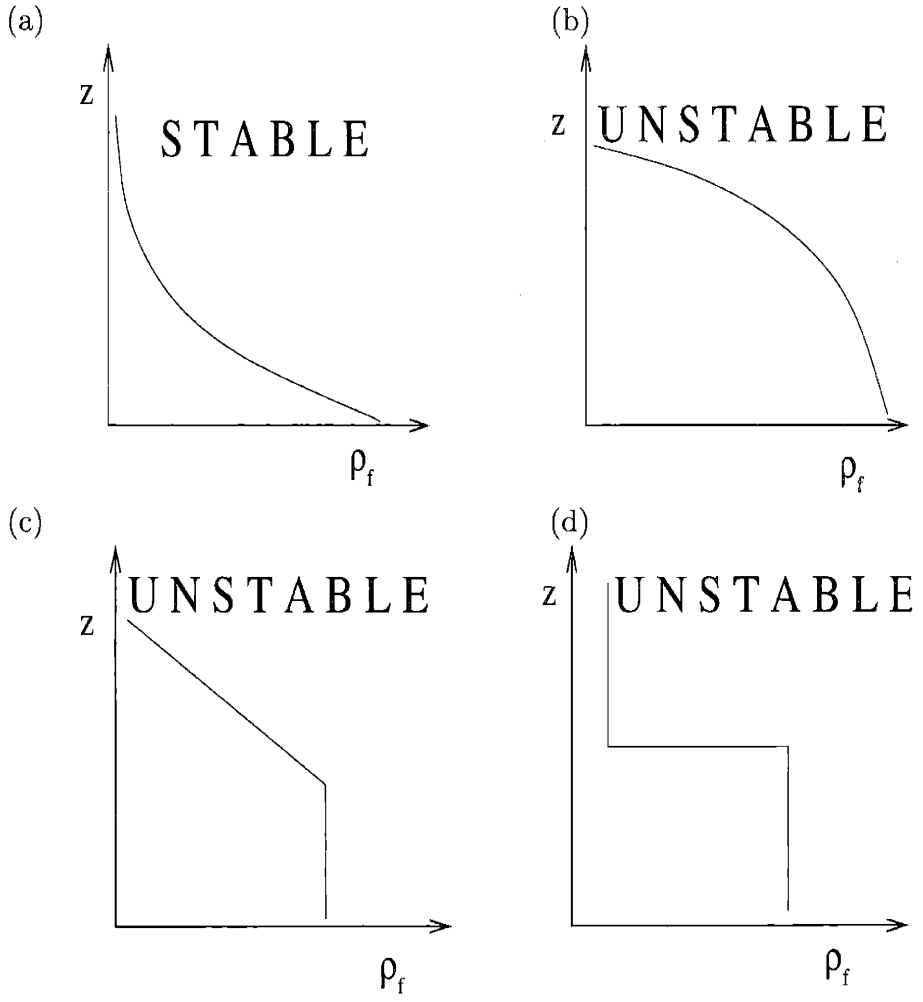

Figure 6-9: A schematic illustration indicating the stability of a uniform particle concentration settling in stably stratified ambients. (a) If the fluid density gradient is constant or decreases with height according to (6.36), the resulting total density profile will remain statically stable. (b, c) A uniform initial particle concentration settling in a density profile such that the fluid density gradient vanishes with depth becomes statically unstable and (d) density jumps also result in the formation of instabilities.

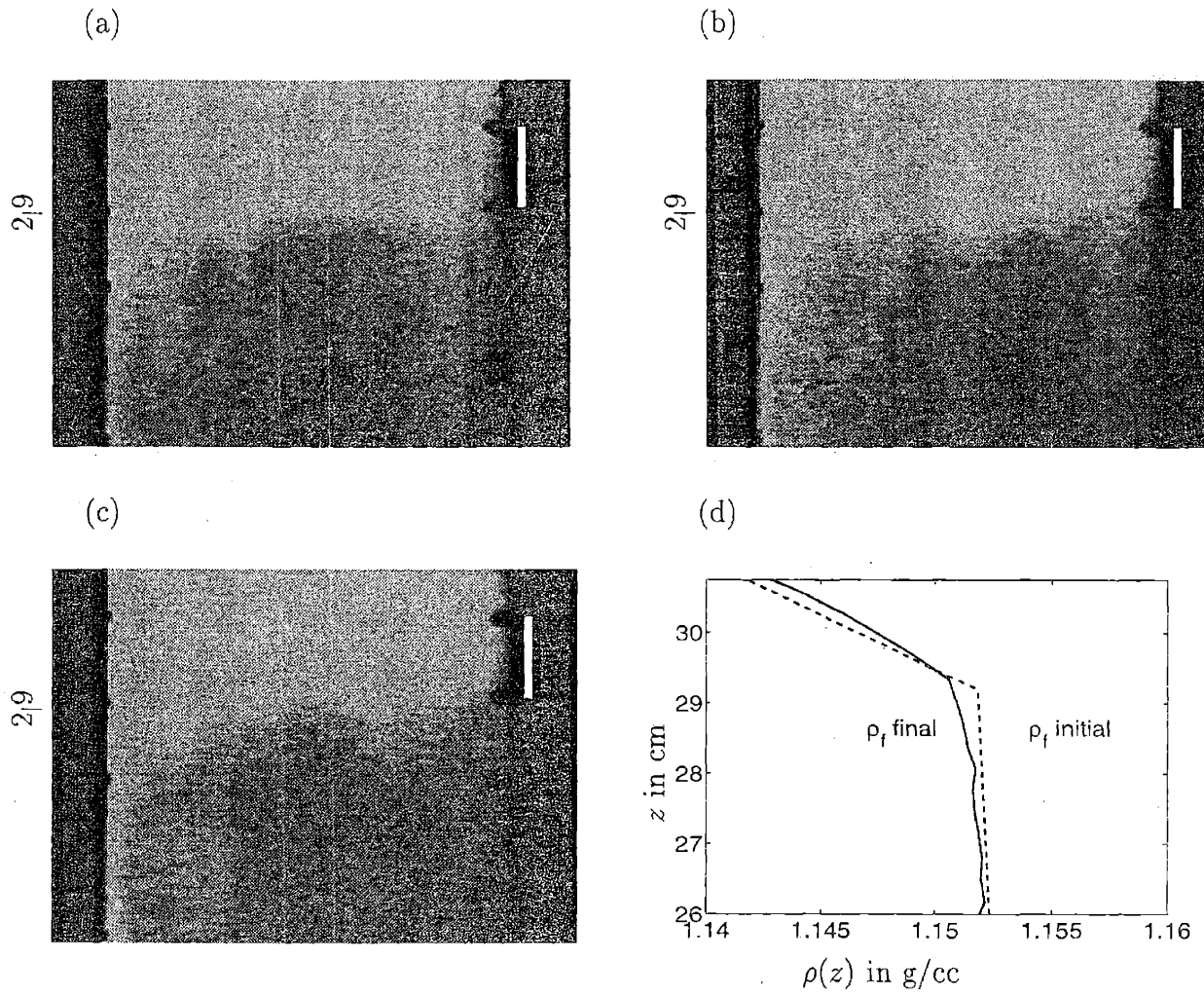

Figure 6-10: The convective motion prompted by an initially uniform concentration of particles settling in density gradient overlying a region of constant density. The corresponding initial and final density profiles are shown in (d). Scale bars in figures (a,b,c) are 1cm long. The formation of centimetric plumes driven by a higher concentration of particles overlying a region of lower particle concentration is observed. Pictures were taken at 30 sec intervals and the region of high concentration is seen to remain stationary while shedding particle plumes. Note that the contrasts were accentuated using Matlab; particles are also present in the lower region.

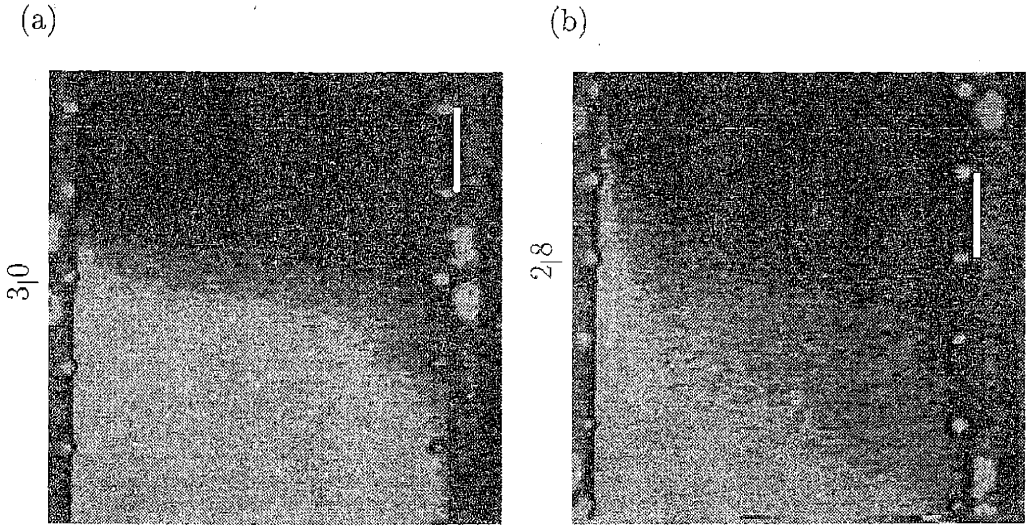

Figure 6-11: Images of the top interface as it settles through (a) a stably stratified ambient ($z = 30$cm) and later through (b) a region of constant density ($z = 28$cm). The initial and final density profiles are shown in figure 6-10d. The density remains approximately constant for $z < 29$cm an decreases linearly for $z > 29$cm. In (a), the top interface is horizontal and relatively sharp when particles settle in a density gradient and do not generate large scale fluid motion. In (b), the top interface reaches a region of constant density in which particles generate convective rolls causing the top interface to become diffuse and tilted. The scale bars are 1cm long.

primarily through convective rolls, with speeds of the order of 1cm/s that exceeded the settling speed of particles by an order of magnitude. The region of uniform density was thus well–mixed and the particle concentration was uniform below a certain level (approximately $z = 28$cm).

Figure 6-11 illustrates the progression of the top interface (a) above the unstable region and (b) through the unstable region. While the top interface was in a stably stratified region it remained horizontal and relatively sharp (figure 6-11a). The velocity of the top interface was not appreciably affected by the presence of instabilities in the lower region. However, as the top interface reached the homogeneous region, its downward velocity increased and exceeded the settling speed of individual particles. The interface also became increasingly diffuse and appeared significantly tilted (figure 6-11b) as convective rolls appreciably distorted the horizontal interface.

6.6 Conclusion

By generalising the results of Kynch (1952) to the case of an ambient with vertical settling speed variations, we have obtained means to predict the time evolution of the concentration of particles settling in a stratified ambient. The basic scenarios of shock and expansion fan are similar to those arising in a homogeneous environment as considered by Kynch (1952). However, the stratified case is richer due to the time dependence of the particle concentration; specifically, the presence of a settling speed gradient causes the particle concentration to increase in time, thus enhancing the influence of hindered settling. In the case of a linear settling speed gradient, an analytical expression describing the particle concentration was found (equation 6.24). The validity of the theoretical predictions describing the progression of the top interface (equation 6.26) and that of concentration jumps (equation 6.27) was verified experimentally by measuring the time evolution of a suspension of latex particles settling in salt stratified water. Good quantitative agreement was found, and the relative importance of hindered settling and ambient stratification could be readily distinguished.

Our experimental system was such that random particle concentration fluctuations were negligible compared to particle concentration variations due to the ambient stratification. Random fluctuations occurs on the scale of the container and typically are of order (Brenner 1999)

$$\Delta\phi_{flu} \sim \frac{(\rho_p - \rho_f)\phi^{1/2}a^{3/2}}{\rho\, h^{3/2}} \tag{6.38}$$

The particle concentration variations due to the presence of an ambient density gradient scale as $\Delta\phi_{str} \sim \phi h(d\rho/dz)$ and in our experiments were dominant relative to $\Delta\phi_{flu}$

$$\frac{\Delta\phi_{flu}}{\Delta\phi_{str}} \sim \frac{a^{3/2}}{h^{3/2}} \frac{(\rho_p - \rho_f)}{\phi^{1/2}h(d\rho/dz)} \sim 10^{-4} \tag{6.39}$$

Random particle concentration fluctuations were also small relative to the mean parti-

cle concentration, $\Delta\phi_{flu}/\phi \sim 10^{-3}$ and convective motions were not discernible when particles settled in a stable linear density gradient or in a uniform ambient, confirming that random fluctuations in ϕ were negligible in our system.

In the presence of a density gradient, sedimentation may lead to the formation of convective instabilities through the development of gravitationally unstable density profiles. Such instabilities modify qualitatively the physical picture described in sections §6.2 and §6.3 and dominate the time evolution of the system. We developed a criterion for the stability of a suspension settling in a stably stratified ambient (equation 6.36) of which experiments provided good qualitative agreement. A similar criterion may be obtained for cases where the settling speed variations are due to viscosity rather than density gradients. Viscosity gradients are easily handled by replacing equation (6.33) with a corresponding expression in terms of the viscosity variation

$$\frac{U_s(z_0)}{U_s(z)} = \frac{\nu(z)}{\nu(z_0)}. \tag{6.40}$$

Variations in settling speed resulting from variations in particle size may be taken into account using a similar approach.

Systems where an unstable ambient density profile is stabilised by varying particle concentrations are known to become unstable as settling particles release light fluid underlying heavier fluid (Huppert *et al.* 1991). In our experiments, the ambient stratification was always statically stable so that such instabilities were not observed. The initial particle concentration profile was also statically stable, being either uniform or increasing with depth, in contrast with the experiments of Hoyal *et al.* (1999) and Parsons *et al.* (2001) where the lower region was initially particle–free. Therefore, particle concentration variations generated by settling through an ambient stratification were the only cause of the convective motions observed.

When an initially uniform particle concentration settled in a density gradient overlying a region of constant density, convective rolls similar to those forming in a Rayleigh-Taylor instability were observed. The top interface was also seen to become diffuse and tilted as it reached the region of instability, owing to the presence of the convective rolls. Instabilities observed in our experiments are qualitatively different from double–diffusive sedimentation (DDS). Double–diffusive instabilities typically form millimeter-scale, sparsely distributed particle–fingers rather than the relatively large convective rolls observed in our experiments. Also, particle–fingers are initiated directly whereas in our experiments approximately 10 minutes were required before the apparition of the first convective rolls. This delay suggests that a region of high particle concentration must be established in a region of little or no fluid density gradient before convective motions are initiated. Experimental observations thus support the simple physical picture presented in §6.5.3 and confirm that particle–driven instabilities may be a dominant feature of sedimentation in a stratified ambient.

Convective motions are expected to dominate the transport of particles if the velocity of the convective rolls is large relative to the settling speed of particles

$$\frac{U_{con}}{U_s} = \frac{\Delta\rho l^2}{(\rho_p - \rho_f)a^2} \gg 1 \tag{6.41}$$

where $\Delta\rho$ is a typical ambient density variation across the unstable region and l is the height of the unstable region. The instability mechanism presented in §6.5.3 is thus likely to be important as particle–laden rivers enter the oceans. As particles settle out of the fresh river water into the denser underlying ocean, their concentration increases which may cause the formation of particle plumes to dominate the particle transport. Also, suspensions settling through the thermocline in the ocean are likely to satisfy (6.36) once they have reached a region of almost uniform density and the subsequent transport of particles is expected to occur mostly through convective rolls.

Chapter 7

Conclusions

Five different problems involving particle settling in an inhomogeneous suspending fluid have been considered. We first investigated systems in which particles are present only in a confined region: a localised release of particles sinking vertically and deposits resulting from the horizontal spreading of particle–laden gravity currents. We then turned our attention to suspensions where particles are present throughout the fluid and studied instabilities resulting from particle concentration gradients settling in an ambient stratification. We also considered layering and mixing resulting from sedimentation beneath an inclined wall. Finally, interactions between hindered settling and ambient stratification were investigated. These problems find applications in a variety of geophysical flows where crystals, sediment, or dust settle in magma chambers, oceans or the atmosphere respectively. Applications are also found in a variety of industrial settings; for example, in the release of waste in the oceans and atmosphere.

In chapter 2, we studied the behaviour of turbulent particle clouds. Using results describing the motion of fluid thermals in homogeneous and stratified ambients, we described the initial stages of the motion of particle clouds. This description is valid until particles rain out from the bottom of the cloud and the radial expansion of the cloud stops. Our experimental approach allowed us to characterise the motion of the cloud and the fallout height in both homogeneous and stratified ambients. In the latter case, the fluid left behind after fallout is buoyant and rises to its level of neutral buoyancy where it intrudes as a gravity current. We derived a criterion describing the various types of deposits resulting from particle clouds, distinguishing between localised, dispersed and ring–shaped deposits. Deposition patterns of contaminated waste in the oceans are an important environmental concern and may be predicted from our results.

Our numerical model gives a good description of the evolution of particle clouds at little computational cost. Comparison between numerical simulations and experimental results allowed us to determine that much of the discrepancies between particle clouds and fluid thermal results from the dependence of the entrainment coefficient on the particle Reynolds number. An experimental study focusing on this aspect of the problem should therefore be the subject of future work.

Particle–laden gravity currents were modeled in chapter 3. Particle clouds reach-

ing the bottom of the container while still in their swarm phase provide a direct application of such gravity currents. As particles settle out of suspension, the driving force of the current is reduced until the fluid comes to a stop and all particles are deposited at the bottom. We developed theoretical models describing the runout length of particle–laden gravity currents and presented numerical simulations of deposits left by such currents. Particular attention was given to flows containing two different types of particles in order to give insight into polydisperse currents. We focused our attention on the deposits of such currents, a problem of interest in oil exploration. We distinguish between deposits resulting from turbulent currents, where the particle concentration is kept uniform by vigourous eddy motions, and laminar currents, where particles simply settle vertically relative to the fluid.

Using box–models, we developed new theoretical predictions for the length of deposits of laminar gravity currents. Our numerical simulations also allowed us to characterise the shape and distribution of particles in deposits left by turbulent and laminar gravity currents with either fixed volume or volume flux. A potentially important aspect of the flow which was not included in our model is the reentrainment of particle from the lower boundary of the container. When the current is sufficiently turbulent, reentrainment may be an important feature of geophysical flows (Garcia & Parker 1991). Future work will focus on the inclusion of this effect in numerical simulations.

In chapter 4, we studied numerically the linear stability of double–diffusive systems where one of the diffusing components has a non–zero settling speed. In particular, we determined the critical particle size below which particles behave essentially as a solute and above which their settling speed qualitatively alters the stability of the system. For glass particles settling in temperature–stratified water, this critical size was found to be of order 1μm. Using equations describing double–diffusive systems, and adding a term describing the advection of particle concentration, we have investigated numerically the conditions under which instabilities may develop. In the presence of particles only, the non–zero settling speed was seen to stabilise systems that would otherwise be subject to Rayleigh–Bénard instabilities. For sufficiently large Péclet numbers ($Pe > 450$), the mode of instability becomes oscillatory, a qualitatively different behaviour from instabilities arising from non–settling components such as heat or salt, where the instability is direct. When both static (heat) and settling (particles) components are present, the non–zero settling speed again acts to stabilise systems where the particle concentration is unstable and to inhibit the formation of particle–fingers. Large Péclet numbers tend to destabilise systems where the ambient density gradient is destabilising (corresponding to the overstable regime of thermohaline systems) and, as Pe increases, the stability of the system tends to be determined by the ambient density gradient only.

No precise experimental measurements of particle–driven double–diffusive instabilities have yet been reported. The conditions under which a particle concentration gradient settling in a homogeneous ambient first becomes unstable shall be investigated experimentally in the future. Particle–fingers have been observed as particles settle across a density jump (Green 1987, Hoyal *et al.* 1999) but no critical Rayleigh number measurements have been provided. Although the presence of a continuously

varying particle concentration renders the onset of instability difficult to observe, both particle–fingers and overstable instabilities may be generated in the laboratory and studied in detail. The conditions under which a particle concentration gradient settling in a homogeneous ambient first becomes unstable shall also be investigated in the future.

In chapter 5, we turned our attention to the flow generated by a suspension of particles settling beneath an inclined wall (the Boycott effect) in a stratified ambient. The layer of clear fluid forming underneath the wall is buoyant and generates a rapid upflow bringing upward heavy bottom fluid. The Boycott effect thus acts as a mixing mechanism for stably stratified fluid, albeit with low energy efficiency, and the ambient density gradient is eroded much faster than it would be through diffusive effects alone. If the density of the ambient fluid decreases sufficiently with height, fluid in the Boycott layer reaches its level of neutral buoyancy, where it intrudes into the bulk of the suspension and generates horizontal layers. These layers are analogous to those formed by the lateral heating of a density gradient and those formed in double–diffusive systems in the presence of a sloping boundary. Our experimental study allowed us to study the size of layers formed by the stratified Boycott as a function of the ambient density gradient and particle concentration. Two types of layers were observed, as is the case in double–diffusive systems with a sloping boundary. Numerical simulations were performed and captured the formation mechanism of the first type of layers, resulting from fluid from the bottom of the container reaching its level of neutral buoyancy. However, our model assumed a constant Boycott layer thickness, which restricted its applicability to relatively short times. A more detailed numerical investigation of this problem should be the subject of future work.

Application of the stratified Boycott effect to magma chambers, where crystals settle in stratified magma beneath a sloping roof, was also presented. Comparison of the magnitude of the flow resulting from the Boycott effect with those resulting from direct settling and diffusion shows that the dynamics of magma chambers may be dominated by the Boycott effect, provided no thermally–driven convection occurs throughout the chamber. Although the uncertainty of the geophysical parameters involved precludes a precise description of layer formation in magma chambers, it is plausible that the layered deposits found at the bottom of solidified magma chambers are a signature of the presence of layers formed through the action of the stratified Boycott effect.

Finally, we studied in chapter 6 a classical sedimentation phenomenon, hindered settling, in combination with settling speed variations. We focused on stably stratified systems where the particle settling speed varied significantly over the course of the setting process (of order 50%). As particles settle, the settling speed reduction causes the particle volume fraction to increase, which in turns enhances the effects of hindered settling. Previous work describing hindered settling effects in a homogeneous ambient was extended to cases where the settling speed varies significantly during the sedimentation process. The time evolution of the particle concentration was thus computed, allowing us to predict the progression of the particle–free — suspension interface and of particle concentration jumps. Through an experimental study, our theoretical results were confirmed and the relative importance of hindered settling

and ambient stratification could be readily distinguished. It was also observed that particles settling in a density gradient overlying a region of constant density could give rise to convection rolls and particle plumes, reminiscent of those generated in Rayleigh–Bénard convection. Instability occurs when a region of high particle concentration forms above a region of relatively low particle concentration, which corresponds to a statically unstable density profile. A criterion for the formation of such instabilities in a stably stratified ambient was presented and was qualitatively verified experimentally.

Precise measurements of the exact conditions under which instability occurs could not be made in our experimental set–up as the presence of particles throughout the system impeded direct observations of the onset of instability. Quantitative verification of our stability criterion thus requires more precise flow visualisation techniques and shall be the subject of future work. Detailed numerical simulations of this type of instability allowing for a better comparison with classical Rayleigh-Bénard convection would also be of interest and should be the subject of future investigation.

Experiments, numerical simulations and analytical methods have been employed to paint as complete a picture as possible of the most important features of a number of flows involving sedimentation in stably stratified ambients. The combination of these three approaches provides a detailed and realistic description of the dynamics of suspensions in a variety of contexts. It is with this philosophy in mind that future work will be conducted.

Bibliography

[1] A. Acrivos and E. Herbolzheimer. Enhanced sedimentation in settling tanks with inclined walls. *J. Fluid Mech.*, 92:435–457, 1979.

[2] D. Houk anf T. Green. Descent rates of suspension fingers. *Deep Sea Res.*, 20:757–761, 1973.

[3] PG. Baines and AE. Gill. On thermohaline convection with linear gradients. *J. Fluid Mech.*, 37:289–306, 1969.

[4] GK. Batchelor. *An introduction to fluid dynamics.* Cambridge Mathematical Library, 1967.

[5] GK. Batchelor. Sedimentation in a dilute dispersion of spheres. *J. Fluid Mech.*, 52:245, 1972.

[6] TB. Benjamin. Gravity currents and related phenomena. *J. Fluid Mech.*, 31:209–248, 1968.

[7] F. Blanchette, JWM. Bush, and T. Peacock. The stratified Boycott effect in magma chambers. *Geoph. Res. Lett.*, under consideration, 2003.

[8] RT. Bonnecaze, HE. Huppert, and JR. Lister. Particle-driven gravity currents. *J. Fluid Mech.*, 250:339–369, 1993.

[9] RT. Bonnecaze, HE. Huppert, and JR. Lister. Patterns of sedimentation from polydispersed turbidity currents. *Proc. Roy. Soc. Lon. A*, 452:2247–2261, 1996.

[10] AE. Boycott. Sedimentation of blood corpuscles. *Nature*, 104:532, 1920.

[11] MP. Brenner. Screening mechanisms in sedimentation. *Phys. Fluids*, 11:754–772, 1999.

[12] J. Bühler and DA. Papantoniou. Barge dumping of rubble in deep water. *Env. Hydr.*, pages 193–198, 1999.

[13] JWM. Bush, BA. Thurber, and F. Blanchette. Particle clouds in homogeneous and stratified environments. *J. Fluid Mech.*, to appear.

[14] RE. Caflisch and JHC. Luke. Variance in the sedimentation speed of a suspension. *Phys. Fluids*, 28:759, 1985.

[15] KV. Cashman. Relationship between plagioclase crystallization and cooling rate in basaltic melts. *Contrib. Mineral. Petrol.*, 113:126–142, 1993.

[16] S. Chandrasekhar. *Hydrodynamic and Hydromagnetic Stability.* Clarendon Press, 1961.

[17] CF. Chen. Stability of thermal convection in a salinity gradient due tolateral heating. *Int. J. Heat Mass Trans.*, 14:57–65, 1971.

[18] CF. Chen. Particle flux through sediment fingers. *Deep Sea Res.*, 44:1645–1654, 1997.

[19] S. Dalziel. http://www.damtp.cam.ac.uk/user/fdl/people/sd/digimage /index.htm.

[20] CR. Darwin. *Second Part of the Geology of the Voyage of the Beagle.* London, 1844.

[21] RH. Davis and A. Acrivos. Sedimentation of noncolloidal particles at low reynolds numbers. *Ann. Rev. fluid Mech.*, 17:91–118, 1985.

[22] RH. Davis and MA. Hassen. Spreading of the interface at the top of a slightly polydisperse sedimenting suspension. *J. Fluid Mech.*, 196:107–134, 1988.

[23] E. Delnoij, FA. Lammers, JAM. Kuipers, and WPM vanSwaaij. Dynamic simulation of dispersed gas-liquid two-phase flow using a discrete bubble model. *Chem. Eng. Sci.*, 52:1429–1458, 1997.

[24] DE. Drake. Suspended sediment and thermal stratification in santa barbara channel. *Deep Sea Res.*, 18:763–769, 1971.

[25] A. Einstein. A new determination of molecular dimensions. *Annals of Physics*, 19:289–306, 1911.

[26] A. Eistein. *Investigations on the theory of the Brownian motion.* Dover publications, 1956.

[27] MP. Escudier and T. Maxworthy. On the motion of turbulent thermals. *J. Fluid Mech.*, 61:541–552, 1973.

[28] ME. Essington, SV. Mattigod, and JO. Ervin. Particle sedimentation–rates in the linear density gradient. *Soil Sc. Soc. Am. J.*, 49(3):767–771, 1985.

[29] HJS. Fernando. The formation of a layerd structure when a stable salinity gradient is heated from below. *J. Fluid Mech.*, 182:525–542, 1987.

[30] HJS. Fernando, MS. Lee, J. Anderson, M. Princevac, E. Pardyjak, and S. Grossman-Clarke. Air circulation and contaminant dispersion in cities. *Env. Fluid Mech.*, 1:1–58, 2001.

[31] BA. Finlayson. *The method of Weighted residuals and variational principles*, pages 151–203. Academic, 1972.

[32] HB. Fischer. Dilution of an undersea sewage by salt fingers. *Deep Sea Res.*, 5:909–915, 1971.

[33] SK. Friedlander. *Smoke, dust, and haze : fundamentals of aerosol dynamics.* Oxford University Press, 2000.

[34] M. Garcia. Depositional turbidity currents laden with poorly sorted sediment. *J. Hydr. Eng.*, 120:1240–1263, Nov 1994.

[35] M. Garcia and G. Parker. Entrainment of bed sediment into suspension. *J. Hydr. Eng.*, 117(4), 1991.

[36] C. Gladstone, JC. Phillips, and RSJ. Sparks. Experiments on bidisperse, constant volume gravity currents: Propagation and sediment deposition. *Sedimentology*, 45:833–843, 1998.

[37] T. Green. The importance of double–diffusion to the settling of suspended material. *Sedimentology*, 34(2):319–331, 1987.

[38] JD. Greenough, CY. Lee, and BJ. Fryer. Evidence for volatile-influenced differentiation in a layeredalkali basalt flow, penghu islands, taiwan. *Bull. Volcanol.*, 60:412–424, 1999.

[39] MA. Hallworth, AJ. Hogg, and HE. Huppert. Effects of external flow on compositional and particle gravity currents. *J. Fluid Mech.*, 359:109–142, 1998.

[40] JM. Ham and GM. Homsy. Hindered settling and hydrodynamic dispersion in quiescent sedimenting suspensions. *J. Multiphase flow*, 14:533–546, 1988.

[41] JE. Hart. On sideways diffusive instability. *J. Fluid Mech.*, 49:279–288, 1971.

[42] C. Härtel, E. Meiburg, and F. Necker. Analysis and direct numerical simulation of the flow at a gravity current head. part 1. flow topology and front speed for slip and no–slip boundaries. *J. Fluid Mech.*, 418:189–212, 2000.

[43] WD. Hill, RR. Rothfus, and K. Li. Boundary enhanced sedimentation due to settling convection. *Int. J. Multiphase Flow*, 3:561–583, 1977.

[44] EJ. Hinch. An averaged–equation approach to particle interactions in a fluid suspension. *J. Fluid Mech.*, 83:695, 1977.

[45] ME. Hodson. The origin of igneous layering in the nunarssuit syenite, south greenland. *Min. Magazine.*, 62(1):9–27, 1998.

[46] AJ. Hogg, M. Ungarish, and HE. Huppert. Particle-driven gravity currents: asymptotics and box-model solutions. *Eur. J. Mech. B-Fluids*, 19:139–165, 2000.

[47] AJ. Hogg, M. Ungarish, and HE. Huppert. Effects of particle sedimentation and rotation on axisymmetric gravity curretns. *Phys. of Fluids*, 13(12):3687–3698, December 2001.

[48] M. Hort, BD. Marsh, and T Spohn. Igneous layering through oscillatory nucleation and crystal settling in well-mixed magmas. *Contrib. Mineral. Petrol.*, 114:425–440, 1993.

[49] AE. Hosoi and TF. Dupont. Layer formation in monodispersive suspensions and colloids. *J. Fluid Mech.*, 328:297–311, 1996.

[50] DP. Hoult. Oil spreading on the sea. *Ann. Rev. Fluid Mech.*, 1972.

[51] DCJD. Hoyal, MI. Bursik, and JF. Atkinson. Settling–driven convection: A mechanism of sedimentation from stratified fluids. *J. Geophys. Res.*, 104:7953–7966, 1999.

[52] HE. Huppert, RC. Kerr, JR. Lister, and JS. Turner. Convection and particle entrainment driven by differential sedimentation. *J. Fluid Mech.*, 226:349–369, 1991.

[53] HE. Huppert and PF. Linden. On heating a stable salinity gradient from below. *J. Fluid Mech.*, 95:431–464, 1979.

[54] HE. Huppert and JE. Simpson. The slumping of gravity currents. *J. Fluid Mech.*, 99:785–799, 1980.

[55] HE. Huppert and RSJ. Sparks. Double–diffusive convection due to crystalization of magmas. *Ann. Rev. Earth Planet Sci.*, 12:11–37, 1984.

[56] HE. Huppert and JS. Turner. Melting icebergs. *nature*, 271:46–48, 1978.

[57] HE. Huppert and JS. Turner. Ice blocks melting into a salinity gradient. *J. Fluid Mech.*, 100:167–384, 1980.

[58] HE. Huppert, JS. Turner, and RSJ. Sparks. Replenished magma chambers: effects of compositional zonation and input rates. *Earth and Planet. Sci. Lett.*, 57:345–357, 1982.

[59] TN. Irvine. Layering and related structures in the duke island and skaergaard intrusions: similarities, differences and origins. In I. Parsons, editor, *Origins of Igneous Layering*, NATO ASI Series C196, pages 185–245. D. Reidel Publ. Co, 1987.

[60] C. Jaupart and S. Tait. Dynamics of differentiation in magma reservoirs. *J. Geophys. Res.*, 100:17,615–17,636, 1995.

[61] AM. Jellinek and RC. Kerr. Magma dynamics, crystallization, and chemical differentiation of the 1959 kilauea iki lava lake, hawaii, revisited. *J. Volcan. Geothem. Res.*, 110:235–263, 2001.

[62] Kinosita K. Sedimentation in tilted vessels. *J. Colloid Interface Sci.*, 4:525–536, 1949.

[63] T. Von Kármán. The engineer grapples with nonlinear problems. *Bull. Am. Math. Soc.*, 46:615, 1940.

[64] OS. Kerr. Heating a salinity gradient from a vertical sidewall: linear theory. *J. Fluid Mech.*, 207:323–352, 1989.

[65] RC. Kerr and JR. Lister. Further results for convection driven by the differential sedimentation of particles. *J. Fluid Mech.*, 243:227–245, 1992.

[66] B. Kneller. Beyond the turbidite paradigm: physical models for deposition of turbidites and their implications for reservoir prediction. In Hartley & Prosser, Characterisation of Deep Marine Clastic Systems Geological Society of London Special Publication, 1995. 94, 29–46.

[67] B. Kneller and C. Buckee. The structure and fluid mechanics of turbidity current: a review of some recent studies and their geological implications. *Sedimentology*, 47:62–94, 2000.

[68] DL. Koch. Hydrodynamic diffusion in a suspension of sedimenting point particles with periodic boundary conditions. *Phys. Fluids*, 6:2894–2900, 1994.

[69] PK. Kundu. *Fluid Mechanics.* Academic Press, 1990.

[70] E. Kuusela and T. Ala-Nissila. Velocity correlations and diffusion during sedimentation. *Phys. Rev. E*, 63(061505), 2001.

[71] GJ. Kynch. A theory of sedimentation. *Trans. Faraday. Soc.*, 48:166–176, 1952.

[72] WF. Leung and RF. Probstein. Lamella tube settlers. model and operation. *Ind. Eng. Chem. Process Des. Dev.*, 22:58–67, 1983.

[73] P. Linden and F. Weber. The formation of layers in a double–diffusive system with a sloping boundary. *J. Fluid Mech.*, 81:757–773, 1977.

[74] PF. Linden and JE. Simpson. Microbursts: a hazard for aircraft. *Nature*, 317:601–602, 1985.

[75] BD. Loncarevic, T. Feiniger, and D. Lefebvre. The sept-iles layered mafic intrusion: Geophysical expression. *Can. J. Earth Sci.*, 27:501–512, 1990.

[76] D. Luketina and D. Wilkinson. Particle clouds in density stratified environments. *Proc. 4th Symp. of Stratified Flows, Grenoble, France*, 1994.

[77] S. MacIntyre, AL. Alldredge, and CC. Gotschalk. Accumulation of marine snow at density discontinuities in the water column. *Limnol. Oceaongr.*, 40:449–468, 1995.

[78] D. Martin and IH. Campbell. Laboratory modeling of convection in magma chambers: Crystallization against sloping floors. *J. Geophys. Res.*, 93(3):7974–7988, 1988.

[79] D. Martin and R. Nokes. Crystal settling in a vigorously convecting magma chamber. *Nature*, 332:534–536, Apr. 1988.

[80] J. Martin, N. Rakotomalala, and D. Salin. Hydrodynamic dispersion broadening of sedimentation front. *Phys. Fluids. Lett.*, 6:3215, 1994.

[81] J. Martin, N. Rakotomalala, and D. Salin. Hydrodynamic dispersion fo noncolloidal suspensions: Measurements from einstein's argument. *Phys. Rev. Lett.*, 74:1347–1350, 1995.

[82] AD. Mason. *Mathematical models of traffic flow and related problems.* PhD thesis, Trinity College, July 1988.

[83] T. Maxworthy. Turbulent vortex rings. *J. Fluid Mech.*, 64:227–239, 1974.

[84] T. Maxworthy. The dynamics of sedimenting surface gravity currents. *J. Fluid Mech.*, 392:27–44, 1999.

[85] K. McMillan, PE. Long, and RW. Cross. Vesiculation in columbia river basalts. *Spec. Pap. Geol. Soc. Am.*, 239:157–167, 1989.

[86] DA. McQuarrie. *Statistical Mechanics.* University science book, 2000.

[87] CE. Mendenhall and M. Mason. The stratified subsidence of fine particles. *Proc. Natl. Acad. Sci.*, 9:199–202, 1923.

[88] SG. Monismith. Wind–forced motions in stratified lakes and their effect on mixed–layer shear. *Limn. and oce.*, 1985.

[89] TB. Moodie, JP. Pascal, and JC. Bowman. Modeling sediment deposition patterns arising from suddenly released fixed-volume turbulent suspensions. *Studies in App. Math.*, 105:333–359, 2000.

[90] BR. Morton, GI. Taylor, and JS. Turner. Turbulent gravitational convection from maintained and instanteneous sources. *Proc. Roy. Soc. Lon.*, 234:1–23, 1956.

[91] PJ. Mucha, SY. Tee, DA Weitz, BI Shraiman, and MP. Brenner. A unifying model for velocity fluctuations in sedimentation. *J. Fluid Mech.*, to appear.

[92] H. Nakamura and K. Kuroda. La cause de l'acceleration de la vitesse de sedimentation des suspensions dans les recipients inclinés. *Keijo J. Med.*, 8:256–296, 1937.

[93] K. Nakatsuji, M. Tamai, and A. Murota. Dynamic behaviour of sand clouds in water. In *Int. Conf. on Physical Modelling of Trnasport and dispersion.* MIT, 1990.

[94] F. Necker, C. Härtel, L. Kleiser, and E. Meiburg. High–reslution simulations of aprticle–driven gravity currents. *Int. Journ. of Multiphase Flow*, 28:279–300, 2002.

[95] H. Nicolai, B. Herzhaft, EJ. Hinch, L. Oger, and E.Guazzelli. Particle velocity fluctuations and hydrodynamic self–diffusion of sedimenting non–Brownian spheres. *Phys. Fluids*, 7:12–23, 1995.

[96] Y. Noh and HJS. Fernando. The transition in sediment pattern of a particle cloud. *Phys. Fluids A*, 5:3049–3055, 1993.

[97] G. Oster. Density gradients. *Sci. Am.*, 213:70, 1965.

[98] G. Oster and M. Yamamoto. Density gradient techniques. *Chem. Rev.*, 63:257–268, 1963.

[99] RC. Paliwal and CF. Chen. Double-diffusive instability in an inclined fluid layer, part 2: Stability analysis. *J. Fluid Mech.*, 98:769–785, 1979.

[100] DA. Papantoniou, J. Bühler, and T. Dracos. On the internal structure of thermals and momentum puffs. In *Int. Conf. on Physical Modelling of Trnasport and dispersion.* MIT, 1990.

[101] G. Parker, M. Garcia, Y. Fukushima, and W. Yu. Experiments on turbidity currents over an erodible bed. *J. Hydr. Res.*, 25:191–244, 1987.

[102] JD. Parsons, JWM. Bush, and JPM Syvitski. Hyperpycnal plume formation from riverine outflows with small sediment concentrations. *Sedimentology*, 48:465–478, 2001.

[103] T. Peacock, F. Blanchette, and JWM. Bush. The stratified Boycott effect. *J. Fluid Mech.*, under consideration.

[104] TJ. Pedley and JO. Kessler. Hydrodynamic phenomena in suspensions of swimming microorganisms. *Ann. Rev. Fluid Mech.*, 24:313–358, 1992.

[105] OM. Phillips. On flow induced by diffusion in a stably stratified fluid. *Deep-Sea Res.*, 17:435–443, 1970.

[106] P. Ponder. On sedimentationand rouleaux formation. *Q. J. Exp. Physiol.*, 15:235–252, 1925.

[107] H. Rahimipour and D. Wilkinson. Dynamic behaviour of particle clouds. In Univesity of Tasmania, editor, *11th Australasian Fluid Mechanics conference*, 1992.

[108] L. Rayleigh. On convection currents in a horizontal layer of fluid, when the higher temperature is on the under side. *Phil. Mag.*, 32:529–546, 1916.

[109] JF. Richardson and WN. Zaki. Sedimentation and fluidisation: Part I. *Trans. Inst. Chem. Eng.*, 32:35–53, 1954.

[110] GJ. Ruggaber. *The dynamics of particle–clouds related to open–water sediment disposals.* PhD thesis, Dept of Civil and Env. Eng., MIT, 2000.

[111] DL. Sahagian and JE. Maus. Basalt vesicularity as a measure of atmospheric pressure and paleoelevation. *Nature*, 372:449–451, 1994.

[112] U. Schaflinger. Influence of nonuniform particl-size on settling beneath downwards facing inclined walls. *Int. J. Multiphase flow*, 11:783–796, 1985.

[113] RW. Schmitt. Growth–rate of super–critical salt fingers. *Deep Sea Res.*, 26:23–40, 1979.

[114] RW. Schmitt. Double diffusion in oceanography. *Ann. rev. fluid mech.*, 26:255–285, 1994.

[115] S. Schoofs, RA. Trompert, and U. Hansen. The formation and evolution of layered structures in porous media. *J. Geophys. Res.*, 103:20,843–20,858, 1998.

[116] RS. Scorer. Experiments on convection of isolated masses of buoyant fluid. *J. Fluid Mech.*, 2:583–594, 1957.

[117] HR. Shaw. Viscosities of magmatic silicate liquids: an empirical method of prediction. *Am. J. Sci.*, 272:870–893, 1972.

[118] GK. Sigworth. Rheological properties of metal alloys in the semi-solid state. *Can. Metal. quarterly*, 35:101–122, 1996.

[119] J.E. Simpson. *Gravity currents : in the environment and the laboratory.* Cambridge University Press, 1987.

[120] GW. Slack. Sedimentation of a large numbe of particles as a cluster in air. *Nature*, 200:1306, 1963.

[121] RL. Smith. Ash-flow magmatism. *Spec. Pap. Geol. Soc. Am.*, 180:5–27, 1979.

[122] VS. Solomatov, P. Olsen, and DJ. Stevenson. Entrainment from a bed of particles by thermal convection. *Earth Planet. Sci. Lett.*, 120:387–393, 1993.

[123] RS. Sparks, HE. Huppert, T. Koyaguchi, and MA. Hallworth. Origin of modal and rhythmic igneous layering by sedimentation in a convecting magma chamber. *Nature*, 361:246–249, January 1993.

[124] RSJ. Sparks, SN. Carey, and H. Sigurdsson. Sedimentation from gravity currents generated by turbulent plumes. *Sedimentology*, 38:839–856, 1991.

[125] FJ. Spera, DA. Yuen, S Clark, and HJ. Hong. Double–diffusive convection in magma chambers, single or multiple layers? *Geophys. Res. Lett.*, 13(1):153–156, 1986.

[126] H. Stommel, AB. Arons, and D. Blanchard. An oceanographical curiosity: the perpertual salt fountain. *Deep Sea Res.*, 3:152–153, 1956.

[127] Y. Suzukawa and U. Narusawa. Structure of growing double–diffusive convection cells. *Trans. ASME C: J. Heat Transfer*, 104:248–254, 1982.

[128] J. Tanny and AB. Tsinober. The dynamics and structure of double–diffusive layers in sidewall heating experiments. *J. Fluid Mech.*, 196:151–160, 1988.

[129] S. Thangam, A. Zebib, and CF. Chen. Transition fronmm shear to sideways diffusive instability in s vertical slot. *J. Fluid Mech.*, 112:151–160, 1981.

[130] SA. Thorpe. The effect of horizontal gradients on thermohaline convection. *J. Fluid Mech.*, 38:375–400, 1969.

[131] S. Torquato, TM. Truskett, and P. G. Debenedetti. Is random close packing of spheres well defined? *Phys. Rev. Lett.*, 84:2064–2067, 2000.

[132] JS. Turner. The behaviour of a stable salinity gradient heated from below. *J. Fluid Mech.*, 33:183–200, 1968.

[133] JS. Turner. *Buoyancy effects in fluids.* Cambridge University Press, 1973.

[134] JS. Turner. Multicomponent convection. *Ann. Rev. Fluid Mech.*, 17:11–44, 1985.

[135] JS. Turner and CF. Chen. Two–dimensional effects in double diffusive convection. *J. Fluid Mech.*, 63:577–592, 1974.

[136] M. Ungarish. *Hydrodynamics of Suspensions.* Springer Verlag, 1993.

[137] G. Veronis. On finite amplitude instability in thermohaline convection. *J. Marine Res.*, 23:1, 1965.

[138] G. Veronis. Effect of a stabilizing gradient of solute on thermal convection. *J. Fluid Mech.*, 34:315, 1968.

[139] C. Völtz, W. Pesch, and I. Rehberg. Rayleigh–taylor instability in a sedimenting suspension. *Phys. Rev. Lett. E*, 65(011404), 2001.

[140] RC. Weast, editor. *Handbook of Chemistry and Physics.* CRC. Press, 1986.

[141] AW. Woods, RE. Holasek, and S. Self. Wind–driven dispersal of volcanic ash plumes and its control on the thermal structure of the plume–top. *Bull. Volcanology*, 1995.

[142] B. Woodward. The motion in and around isolated thermals. *Quart. J. Roy. Met. Soc.*, 85:144–151, 1959.

[143] LD. Wright. Sediment transport and deposition at river mouths: a synthesis. *Geol. S. of Ame. Bull.*, 88:857–868, 1977.

[144] A. Wuest and E. Carmack. A priori estimates of mixing and circulation in the hard–to–reach water body of lake vostok. *Ocean Model.*, 2:29–43, 2000.